PUBLICATIONS OF
THE UNIVERSITY OF EASTERN FINLAND

*Dissertations in Forestry and Natural Sciences*


**LASSE RÄSÄNEN**

# FUNCTIONAL MR IMAGING AND BIOMECHANICAL MODELING OF THE KNEE

*Significance of Collagen and Fixed Charge Density on Articular Cartilage Mechanics*

**LASSE RÄSÄNEN**

# *Functional MR Imaging and Biomechanical Modeling of The Knee*

## *Significance of Collagen and Fixed Charge Density on Articular Cartilage Mechanics*

Publications of the University of Eastern Finland
Dissertations in Forestry and Natural Sciences
No 226

Academic Dissertation
To be presented by permission of the Faculty of Science and Forestry for public examination in auditorium SN201 in Snellmania Building of the University of Eastern Finland, Kuopio, on June 11th, 2016,
at 12:00 o'clock.

Department of Applied Physics

Grano Oy
Jyväskylä, 2016
Editors: Prof. Jukka Tuomela, Prof. Pertti Pasanen
Prof. Pekka Toivanen, Prof. Matti Vornanen

Distribution:
University of Eastern Finland Library / Sales of publications
P.O. Box 107, FI-80101 Joensuu, Finland
tel. +358-50-3058396
http://www.uef.fi/kirjasto

ISBN: 978-952-61-2146-8 (printed)
ISSNL: 1798-5668
ISSN: 1798-5668
ISBN: 978-952-61-2147-5 (pdf)
ISSNL: 1798-5668
ISSN: 1798-5676

Author's address:
University of Eastern Finland
Dept. of Applied Physics
P.O.Box 1627
70211 Kuopio
Finland
email: lasse.rasanen@uef.fi / lasse.p.rasanen@gmail.com

Supervisors:
Associate Professor Rami K. Korhonen, Ph.D.
University of Eastern Finland
Dept. of Applied Physics
Kuopio, Finland
email: rami.korhonen@uef.fi

Dean Jukka S. Jurvelin, Ph.D.
University of Eastern Finland
Dept. of Applied Physics
Kuopio, Finland
email: jukka.jurvelin@uef.fi

Reviewers:
Professor Garry Gold, MD
Stanford School of Medicine
Department of Radiology
1201 Welch Road
Stanford, CA 94304-5488, USA
email: gold@stanford.edu

Associate Professor Rajshree Mootanah, Ph.D., MBA
Anglia Ruskin University
Director, Medical Engineering Research Group
Bishop Hall Lane, Chelmsford, CM1 1SQ
Chelmsford, Essex, United Kingdom
email: rajshree.mootanah@anglia.ac.uk

Opponent:
Associate Professor Corey P. Neu, Ph.D.
University of Colorado Boulder
College of Engineering and Applied Science
Mechanical Engineering
Engineering Admin Wing, 1111 Engineering Drive
Boulder, CO 80309 USA
email: cpneu@colorado.edu

**ABSTRACT**

The main components of articular cartilage, *i.e.* the highly organized collagen fibril network, proteoglycans (fixed charge density, FCD) and fluid, determine the response of the knee joint to loading such as walking or standing. Cartilage composition has been found to be a subject- specific feature, varying extensively with tissue depth and location as well as the condition of the joint. The disruption of the cartilage network, *e.g.*, due to osteoarthritis (OA), impairs the function of the joint and can eventually lead to a progressive loss of cartilage tissue and function of the knee. Current magnetic resonance imaging (MRI) modalities allow the evaluation of cartilage structure and composition in a non-invasive manner. For example, $T_2$ methods are capable of visualizing the water bound up by the collagen network, thus revealing variations in the orientations of collagen fibrils, while methods such as sodium MRI can be used to estimate the fixed charge density of cartilage. However, the current clinical methods cannot predict the influence of the tissue composition on knee joint mechanics. In addition, the early stages of OA are usually not diagnosed until significant cartilage loss has occurred.

By combining clinically available information about the cartilage composition and condition with biomechanical modeling of the knee joint, one can investigate the subject-specific joint function and the influence of the local and spatial variations in the cartilage composition on joint mechanics in a non-invasive manner. Nonetheless, the subject-specific cartilage structure, obtained from clinical MRI, has not been implemented into biomechanical knee joint models before.

The aim of this thesis was to investigate the influence of the spatial variation of cartilage composition on knee joint stresses and strains using finite element analysis. In these studies, the collagen architectures were obtained in 2-D and 3-D of the tibial cartilages from asymptomatic male subjects, using $T_2$ mapped clinical MR data sets. The models, based on MR -imaging, were simulated us-

ing impact loading and during the stance phase of gait. Furthermore, the FCD distribution of tibial cartilage of a healthy volunteer was calculated from sodium MRI and its effect on the knee joint response to standing (static, creep load) and during gait was investigated. The models with subject-specific collagen architectures and FCD distributions were compared to models with alternative compositions and to those with generic, non-specific, tissue compositions.

The results indicated that the spatial variation of collagen architecture (from $T_2$ maps of MRI) and FCD of cartilage (from sodium MRI) modulate the mechanical response of human knee joint cartilage in a depth-, location- and time-dependent manner both in 2-D (impact) and 3-D (gait and standing). Furthermore, the inaccuracies in the determination of the composition and its implementation into the model can lead to erroneous model predictions in the evaluation of the joint mechanics. The subject-specific FCD, and the swelling of the tissue caused by it, influenced the internal tissue strain in the cartilage and therefore affected the knee joint function, both during static and dynamic loading, as well as following cartilage tissue degeneration (*e.g.* due to OA).

In conclusion, the determination of the cartilage composition from clinical and pre-clinical MRI is feasible and may be used to evaluate the subject-specific joint mechanics using biomechanical modeling. Specifically, the local and spatial variations in collagen fibril orientations and in FCD modulate the cartilage response in a spatial and time-dependent manner during everyday activities, such as standing and walking. In addition, if one ignores this variation in the cartilage constituents, this may well lead to an inaccurate estimate of the joint function. These results suggest that, in order to investigate the joint mechanics in a subject-specific manner using biomechanical modeling, the corresponding collagen architecture as well as the FCD distribution *e.g.*, as determined from MRI, should be taken into account. Ultimately, the presented methods could be applied as a diagnostic tool to investigate the joint mechanics and possible failure sites in cartilage in a subject-specific

manner.

*National Library of Medicine Classification: QT 34.5, QU 55.3, WE 300, WE 870, WN 185*

*Medical Subject Headings: Knee; Knee Joint; Biomechanical Phenomena; Stress, Mechanical; Magnetic Resonance Imaging; Finite Element Analysis; Cartilage, Articular; Collagen; Proteoglycans; Posture; Gait; Cartilage Diseases/diagnosis*

*Yleinen suomalainen asiasanasto: polvet; nivelrusto; biomekaniikka; rasitus; mallintaminen; magneettitutkimus; elementtimenetelmä; kollageenit*

# *Acknowledgements*

This study was carried out during the years 2012-2016 in the Department of Applied Physics of the University of Eastern Finland and was financially supported by European Research Council under the European Union's Seventh Framework Programme (FP/2007-2013)/ERC Grant Agreement no. 281180, the strategic funding of University of Eastern Finland and Kuopio University Hospital (EVO grants), National Doctoral Programme of Musculoskeletal Disorders and Biomaterials (TBDP) and Saastamoinen Foundation. CSC-IT Center for Science, Finland, is acknowledged for computing resources and modeling software.

I'd like to start by thanking my supervisors, Associate Professor Rami Korhonen and Dean Jukka Jurvelin, for providing me with the opportunity and challenge that this thesis has been. Specifically, I'd like to thank Rami for creating an inspirational working environment and recruiting such a talented group of people. It's quite remarkable how all that combines to produce an atmosphere that genuinely encourages people to think and push themselves, while having simultaneously a relaxed and laid back feel to it. Thank you for that. I'd like to thank Jukka for the guidance and sharing with us your wide perspective and all the knowledge that you have gathered throughout the years.

I also wish to thank the reviewers of this thesis, Professor Garry Gold and Associate Professor Rajshree Mootanah, for giving their professional and constructive criticism and views on the thesis. I'd also like to thank Ewen MacDonald, Ph.D., for the linguistic review.

I'd also like to express my deepest gratitude to all the co-authors for their valuable work and sharing of the knowledge throughout the thesis. In particular, I'd like to thank Professor Miika Nieminen and Eveliina Lammentausta, Ph.D. for introducing me to MRI and igniting my interest toward this topic.

This goes to all my colleagues in the Biophysics of Bone and

Cartilage (BBC) research group and to all the people I've had the chance to interact with; it's been a privilege to work with such a great group of people during these years. In particular, I'd like to thank my "roommates", Mikko Venäläinen, M.Sc., Simo Ojanen, M.Sc., and Mimmi Liukkonen, M.Sc., in addition to Petri Tanska, M.Sc., for the more or less relevant discussions (in particular, Mikko and Simo, for providing the tunes for the day and for being someone to chase after on the floorball and futsal fields). Mika Mononen, Ph.D., is especially acknowledged for all the support and for giving "the magic touch" to all matters related to knee joint modeling. Most importantly, I'd like to thank Juuso Honkanen, Ph.D (soon), and Petri Tanska, Ph.D (soon), for all the great times and for travelling alongside me all the way from year one up to this date (and onward). Cheers mates!

I'm tremendously grateful to my family; to my mother Eira, my father Tapani and my brother Matti, for all the encouragement and support you have given throughout the years. I cannot thank you enough for everything. I'd also like to thank my longtime friend, Markku, for all the discussions and sessions of "saving the world" (still in progress). I cherish them all.

Last, but certainly not least, by beloved Lotta. I cannot express how grateful I am for the continuous support and encouragement as well as the patience and understanding you've expressed through the long days, evenings and nights along the years. You have made this all possible, sensible and worthwhile.

This thesis, and the journey to its completion, would not have been possible without all of you.

Lasse Räsänen
Kuopio, May 2016

## ABBREVIATIONS

| | |
|---|---|
| 2-D | Two-dimensional |
| 3-D | Three-dimensional |
| AC | Articular cartilage |
| C3D8P | Continuum element type with 8 nodes and porosity |
| CPE4P11 | Porous plane strain element |
| CT | Computed tomography |
| CW | Continuous wave |
| DD | Digital densitometry |
| DESS | Double or dual echo steady state (sequence) |
| dGEMRIC | Delayed gadolinium enhanced magnetic resonance imaging of cartilage |
| ECM | Extracellular matrix |
| FCD | Fixed charge density |
| FE | Finite element |
| FEM | Finite element modeling |
| FRPE | Fibril-reinforced poroelastic |
| FRPVE | Fibril-reinforced poroviscoelastic |
| FRPVES | Fibril-reinforced poroviscoelastic with swelling |
| GAG | Glycosaminoglycan |
| gagCEST | GAG-specific chemical exchange dependent saturation transfer |
| GRE | Gradient echo |
| ICP | Iterative closest point (method) |
| LCL | Lateral collateral ligament |
| MCL | Medial collateral ligament |
| MESE | Multi-echo spin echo |
| MR | Magnetic resonance |
| MRI | Magnetic resonance imaging |
| MT | Magnetization transfer |
| NMR | Nuclear magnetic resonance |
| OA | Osteoarthritis |
| OAI | The Osteoarthritis Initiative |
| PCL | Posterior cruciate ligament |

| | |
|---|---|
| PD | Proton density |
| PG | Proteoglycan |
| PLM | Polarized light microscopy |
| PVE | Partial volume effect |
| RF | Radio frequency |
| SE | Spin echo |
| SR | Saturation recovery |
| SNR | Signal-to-noise ratio |
| POR | Pore pressure |
| T | Tesla (unit of magnetic flux density) |
| vTE | Variable Echo Time |

## SYMBOLS

| | |
|---|---|
| $^1H$ | Nucleus of hydrogen, *i.e.* proton |
| $^{23}Na$ | Sodium (ion) |
| $A$ | Amplitude (of relaxation time components) |
| $B_0$ | External or static magnetic field, *i.e.* the main magnetic field induced by the MRI equipment |
| $B_1$ | Magnetic field induced by radio frequency (RF) pulse, *i.e.* the magnetic field inside a subject |
| $B_{1,SL}$ | Magnetic field induced by a spin lock (SL) pulse |
| $B_z$ | Internal magnetic field component in z-direction, *i.e.* the magnetic field inside a subject |
| $BW$ | Imaging bandwidth |
| $C$ | Tissue stiffness matrix |
| $c$ | Concentration |
| $c^-$ | Mobile anion constant |
| $d_z$ | Tissue depth |
| $d$ | Tissue thickness |
| $E_f^0$ | Initial fibril network modulus |
| $E_f^\varepsilon$ | Strain-dependent fibril network modulus |
| $E_m$ | Elastic modulus |
| $e$ | Void ratio |
| $e_0$ | Initial void ratio |
| $F$ | Deformation tensor |
| $G_m$ | Shear modulus |
| $\boldsymbol{I}$ | Unit tensor |
| $J$ | (Jacobian) determinant of the deformation tensor |
| $K_m$ | Bulk modulus |
| $k$ | Permeability |
| $k_0$ | Initial permeability |
| $M_{xy}$ | Magnetization in the transverse plane |
| $M_z$ | Magnetization in the longitudinal plane |
| $n_f$ | Fluid fraction |
| $p$ | Fluid pressure |

| | |
|---|---|
| $R$ | Molar gas constant |
| $S_0$ | Initial signal intensity |
| $S_{xy}$ | Observed (attenuated) signal intensity |
| $T$ | Absolute temperature |
| $T_1$ | Longitudinal or spin-lattice relaxation time |
| $T_{1\rho}$ | Longitudinal relaxation time in rotating frame |
| $T_2$ | Transverse or spin-spin relaxation time |
| $T_2^*$ | The apparent transverse relaxation time |
| $T_{2\rho}$ | Transverse relaxation time in rotating frame |
| $T_C$ | Chemical expansion stress |
| $T_E$ | Time-to-echo, *i.e.* echo time |
| $T_R$ | Time-to-repeat, *i.e.* repetition time |
| $t$ | Time |
| $totf$ | Total number of fibrils |
| $\gamma_{ext}^{\pm}$ | External activity coefficient |
| $\gamma_{int}^{\pm}$ | Internal activity coefficient |
| $\Delta\phi$ | Donnan equilibrium pressure gradient, *i.e.* swelling pressure gradient |
| $\varepsilon_f$ | Fibril strain |
| $\dot{\varepsilon_f}$ | Strain rate |
| $\varepsilon_{nf}$ | Non-fibrillar strain (elastic strain tensor) |
| $\zeta$ | Density ratio between the primary and secondary collagen fibrils |
| $\eta$ | Viscoelastic damping coefficient |
| $\theta$ | Flip angle |
| $\mu_f$ | Electrochemical potential of water |
| $\rho_z$ | Fibril volume fraction |
| $\sigma_f$ | Fibril network stress |
| $\dot{\sigma_f}$ | Stress rate |
| $\sigma_{nf}$ | Non-fibrillar stress |
| $\sigma_{tot}$ | Total stress |
| $\upsilon$ | Poisson's ratio |
| $\Phi_{ext}$ | External osmotic coefficient |
| $\Phi_{int}$ | Internal osmotic coefficient |
| $\omega_0$ | Larmor frequency |

## LIST OF PUBLICATIONS

This thesis consists of a review of the author's work and publications on subject-specific modeling of knee joint based on MRI:

**I** Räsänen L.P., Mononen, M.E., Nieminen M.T., Lammentausta E., Jurvelin J.S. and Korhonen R.K., "Implementation of subject-specific collagen architecture of cartilage into a 2D computational model of a knee joint - data from the Osteoarthritis Initiative (OAI)". *Journal of Orthopaedic Research*. **31 (1)**, 10-22 (2013).

**II** Räsänen L.P., Mononen, M.E., Nieminen M.T., Lammentausta E., Jurvelin J.S. and Korhonen R.K., "Three Dimensional Patient-Specific Collagen Architecture Modulates Cartilage Responses in the Knee Joint During Gait". *Computer Methods in Biomechanics and Biomedical Engineering*.
***DOI:*** *10.1080/10255842.2015.1124269* (2015).

**III** Räsänen L.P., Tanska P.K., Mononen, M.E., Lammentausta E., Zbyn S., Szomolanyi P., Venäläinen M.S., van Donkelaar C.C., Jurvelin J.S., Trattnig, S., Nieminen M.T., and Korhonen R.K., "Subject-specific Spatial Variation of Fixed Charge Density in Knee Joint Cartilage from Sodium MRI – Implication on Knee Joint Mechanics Under Static Loading". *Journal of Biomechanics. (Submitted)* (01/2016).

**IV** (Conference proceeding) Räsänen L.P., Tanska P.K., Zbyn S., Trattnig S., Nieminen M.T., and Korhonen R.K., "Effect of Cartilage Swelling and Fixed Charge Density on Knee Joint Mechanics During Gait". *Transactions of the Orthopaedic Research Society*. **62**, 243 (2016).

Throughout the thesis, these papers will be referred to by Roman numerals.

## AUTHOR'S CONTRIBUTION

The publications in this thesis are original research papers on biomechanical modeling of the subject-specific composition and joint mechanics in the human knee joint. The author has been the main contributor to the execution of the studies; participated in the planning and conducting the MR imaging, performed the MR data-analyses (apart from the $T_2$ mapping, which was conducted by E. Lammentausta, Ph.D.), as well as the implementation of the data to FE-model, the simulations and data-analyses. The author has been the main writer of each paper.

# *Contents*


**1 INTRODUCTION** **1**

**2 COMPOSITION AND FUNCTION OF KNEE JOINT TISSUES** **5**

2.1 Articular cartilage . . . . . 7

2.1.1 Tissue composition . . . . . 7

2.1.2 Biomechanics . . . . . 10

2.2 Other knee joint tissues . . . . . 12

2.3 Osteoarthritis and its evaluation . . . . . 14

**3 MAGNETIC RESONANCE IMAGING OF ARTICULAR CARTILAGE** **17**

3.1 Principles of clinical MRI . . . . . 17

3.2 Articular cartilage structure and composition from MRI 19

3.2.1 $T_2$ -methods . . . . . 20

3.2.2 Sodium MRI ($^{23}$Na-MRI) . . . . . 22

3.2.3 Other imaging modalities . . . . . 24

**4 FINITE ELEMENT MODELING OF THE SOFT KNEE JOINT TISSUES** **27**

4.1 Fibril-reinforced poroviscoelastic modeling of cartilage 28

4.1.1 Fibril-reinforced poroviscoelastic properties . 28

4.1.2 Fibril-reinforced poroviscoelastic materials with swelling . . . . . 31

4.2 Applications and benefits of the knee joint models . . 32

**5 AIMS** **37**

**6 MATERIALS AND METHODS** **39**

6.1 Cartilage structure and tissue deformation from MRI 39

6.1.1 Magnetic resonance imaging and segmentation 39

6.1.2 Collagen architecture from $T_2$ maps of MRI . 42

6.1.3 Fixed charge density from sodium MRI . . . . 43
6.1.4 Tibial cartilage deformation under 120 N load 46
6.2 Model parameters . . . . . 47
6.2.1 Model geometries and finite element meshes . 47
6.2.2 Material parameters . . . . . 48
6.3 Cartilage structure in the models . . . . . 50
6.3.1 Implementation of collagen fibril orientations and FCD into the joint models . . . . . 50
6.3.2 Subject-specific and alternative models . . . . 52
6.4 Boundary conditions and simulations . . . . . 57

**7 RESULTS** **61**
7.1 Effect of subject-specific collagen architecture . . . . . 61
7.2 Effect of subject-specific variation of FCD . . . . . 67

**8 DISCUSSION** **75**
8.1 Model validity . . . . . 75
8.2 Importance of subject-specific cartilage composition . 77
8.2.1 Collagen architecture . . . . . 77
8.2.2 Fixed charge density . . . . . 80
8.3 Limitations . . . . . 83

**9 SUMMARY AND CONCLUSIONS** **89**
9.1 Future aspects . . . . . 91

**REFERENCES** **93**

# 1 Introduction

Articular cartilage (AC) of the knee joint is a thin layer of fibrous connective tissue covering the articulating joint surfaces. Its main function is to transmit and distribute loads across the articulating bone surfaces in order to minimize stress concentrations in the joints, and to ensure smooth and virtually frictionless movement of the joint surfaces. The highly organized and anisotropic structure and composition of AC are well adapted to this purpose [1]. The distribution of forces in the joint and, hence, the function of the joint are dependent on the composition and integrity of the articular cartilage matrix [1–3].

The composition of articular cartilage can be divided into two separate phases, the fluid phase and the solid phase, which is mainly composed of collagen fibrils and proteoglycans (PGs) [4]. The depth-wise variation of the collagen fibril orientations in articular cartilage results in an organized laminar structure of the tissue [4–6]. The collagen fibril network primarily controls the tensile stiffness and dynamic compressive stiffness of cartilage, modifies the fluid flow and resists tissue swelling in the knee joint [2, 3, 7]. It has been demonstrated that it is the organization of the collagen fibrils in the network that mostly determines the cartilage response to dynamic loading [2,3]. PGs, on the other hand, are non-homogeneously distributed proteins immobilized within articular cartilage and their concentration varies with tissue depth [1, 8, 9]. PGs carry negatively charged glycosaminoglycan (GAG) side chains, resulting in a fixed charge density (FCD) of the tissue [1, 10]. FCD results in increased osmotic pressure and swelling in the tissue, and therefore the PG content of cartilage primarily determines the static compressive stiffness of the tissue [3, 11]. The early stages of osteoarthritis (OA) are characterized by a disruption of the collagen network, reduced PG content and an increased fluid fraction in the joint cartilage, causing pain and impaired functioning of the joint, eventually

leading to a complete loss of articular cartilage [12–14].

The current high-field magnetic resonance imaging (MRI) techniques enable evaluation of the cartilage condition, morphology, constituents and the structure of the tissue [15–17]. The depth-dependent anisotropy of cartilage leads to observable variations in the relaxation times and signal intensity of MRI in conjunction with cartilage depth [18, 19]. In particular, the $T_2$-relaxation time of MRI correlates, *e.g.*, with the orientation of the collagen fibrils, making it possible to evaluate the integrity and the morphology of the collagen network [20–22]. The negative charge of the PGs, on the other hand, attracts positive sodium ions, and thus, this enables the measurement of PG distribution and the FCD in articular cartilage *e.g.* using sodium imaging techniques of MRI ($^{23}$Na-MRI) [23–25]. However, the diagnostics of the condition of articular cartilage are still somewhat limited and the function of the knee joint tissues is yet to be elucidated with the current non-invasive methods available in the clinic.

Finite element (FE) modeling is a non-invasive computational method that allows a simulation of knee joint function during daily activities, such as walking or standing [26–29]. Even though the importance of the collagen network and FCD of cartilage tissue on joint function is well known, these constituents have not been taken into account in a subject-specific manner in previous studies. By implementing the cartilage geometry and structure (collagen architecture, fibril orientation and PG distribution) from MRI and a realistic loading into a biomechanical model, it is possible to evaluate stress, strain and pressure distributions in the knee joint in a non-invasive, subject-specific manner. By including the information of cartilage structure obtained from MRI, FE modeling can provide information on the functional properties of cartilage and thus enable the evaluation of the function of the tissue constituents to joint mechanics as well as evaluating possible failure points.

The aim of these studies was to investigate the importance of subject-specific variation of cartilage composition on knee joint mechanics during standing and walking. This was done by using clin-

ically feasible and accessible imaging modalities (namely MRI). In study **I**, the method to determine collagen architecture from MRI and the importance of the depth-wise variations in the collagen fibril orientations were investigated using a 2-D joint model under impact loading. In study **II**, the effect of the spatial, subject-specific, variation of collagen fibril orientations in the tibial cartilage was investigated in a 3-D joint model during gait. Finally, in study **III**, the subject-specific variations in the FCD in tibial cartilage was determined from $^{23}$Na-MRI and its importance on knee joint mechanics was investigated during standing. In addition, the importance of the swelling of the cartilage tissue due to FCD was evaluated during walking (Study **IV**, unpublished).

The present studies aim to merge computational modeling techniques with the clinically available information describing the composition and function of the knee joint. This has been done in order to develop functional, diagnostic imaging and modeling methods so that it will be possible to investigate the joint function in a subject-specific manner. The presented methods could be used as diagnostic tools to estimate putative failure sites in a knee joint and possibly to help assess the onset of OA in a subject-specific manner. Hence, in clinical use, the methods could aid in the diagnostics and possible treatment planning of knee joint pathologies.

# 2 Composition and function of knee joint tissues

The human knee joint is a complex synovial joint consisting of a variety of soft tissues articulating the femoral, tibial and patellar bones (Fig. 2.1a) [1]. The connective soft tissues include muscles and tendons, the anterior and posterior cruciate ligaments (ACL and PCL, respectively), the lateral and medial collateral ligaments (LCL and MCL, respectively), menisci and articular cartilages. The muscles transmit forces to the joint through the tendons, whereas ligaments restrict the motion of the joint [1, 30]. The space between the articulating bones is filled with synovial fluid, menisci and articular cartilage tissues that ensure a smooth movement of the knee joint and distribute the load across the articulating surfaces (Fig. 2.1a) [1, 31]. The structure and composition of these soft tissues contribute significantly to the mechanics of the knee joint [1, 30]. This study will focus on the role of the composition of articular cartilage, in particular that of the tibial cartilage, on the function and mechanics of the knee joint.

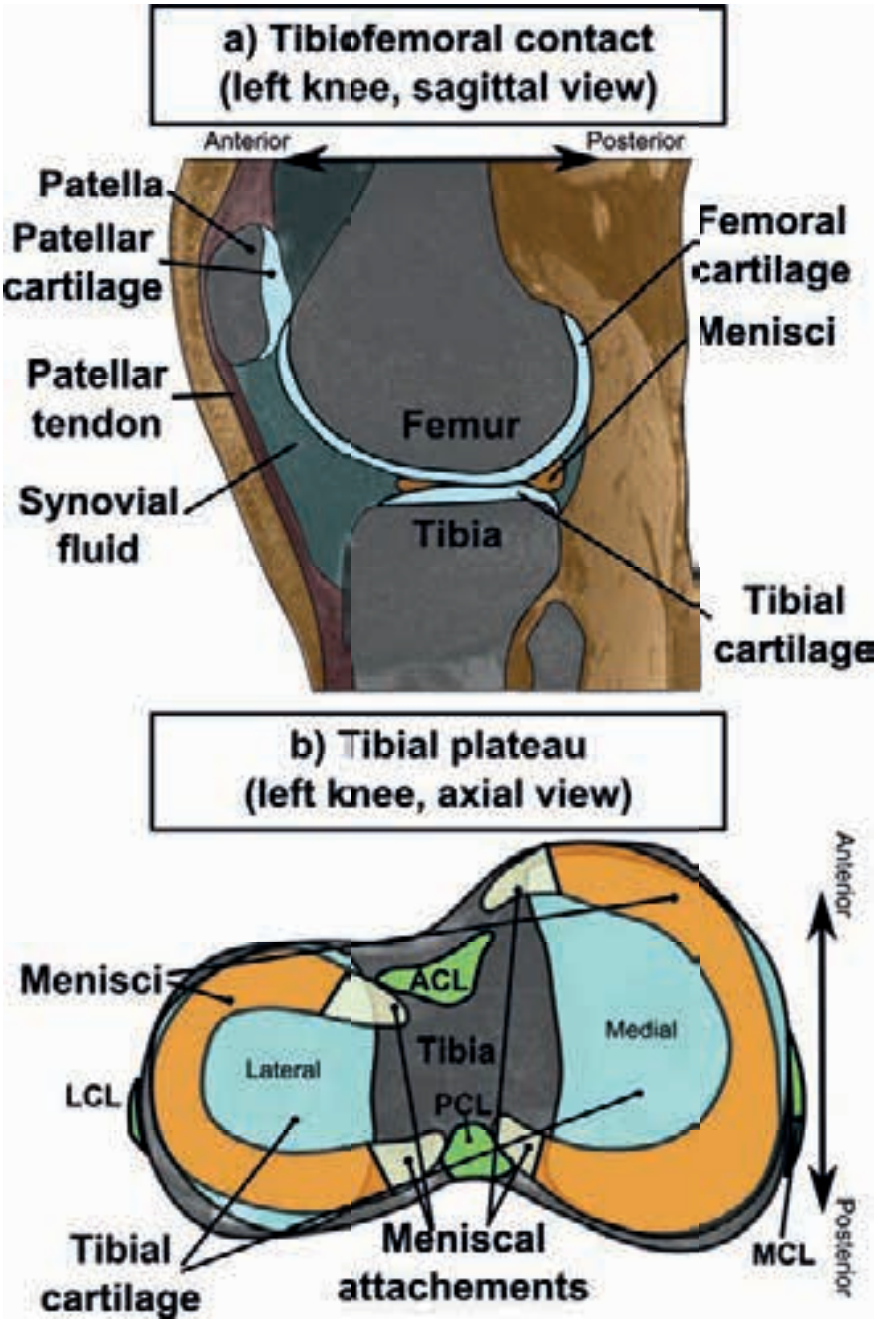


*Figure 2.1: Schematic representation of a) the left knee joint and b) an axial view of the surface of tibial plateau. ACL & PCL = anterior & posterior cruciate ligament, LCL & MCL = lateral & medial collateral ligament*

## 2.1 ARTICULAR CARTILAGE

Articular cartilage is an avascular layer of fibrous connective tissue covering the articulating surfaces of the femoral, tibial and patellar bones (Fig. 2.1) [32]. Articular cartilage primarily acts as a kind of cushion capable of transmitting and distributing articular forces over the articulating bone surfaces in order to minimize stress concentrations while simultaneously allowing smooth and virtually frictionless movement of the joint surfaces in conjunction with the synovial fluid [2, 33]. The mechanical properties of articular cartilage are dependent on the composition and structure of the tissue (Fig. 2.2) [1, 3].

### 2.1.1 Tissue composition

Articular cartilage can be described as a fibril-reinforced, viscoelastic tissue with a highly inhomogeneous composition (Fig. 2.2) [2, 33]. Articular cartilage is mainly composed of chondrocytes, *i.e.* articular cartilage cells, and the extracellular matrix (ECM) [34, 35]. The ECM can be further divided into two distinct phases; the solid phase and the fluid phase [1, 30, 34]. The fluid phase is mainly composed of interstitial fluid as well as solutes that fill the pores in the ECM [11, 36, 37]. The solid phase on the other hand is mainly composed of proteoglycans (PGs) and collagen fibrils (altogether 20-40% of the cartilage wet weight) [38]. The organization and concentration of the cartilage constituents vary with tissue depth (Fig. 2.2), and the composition of cartilage tissue is strongly adapted to the loading conditions to which the joint is subjected [1, 3, 5, 38].

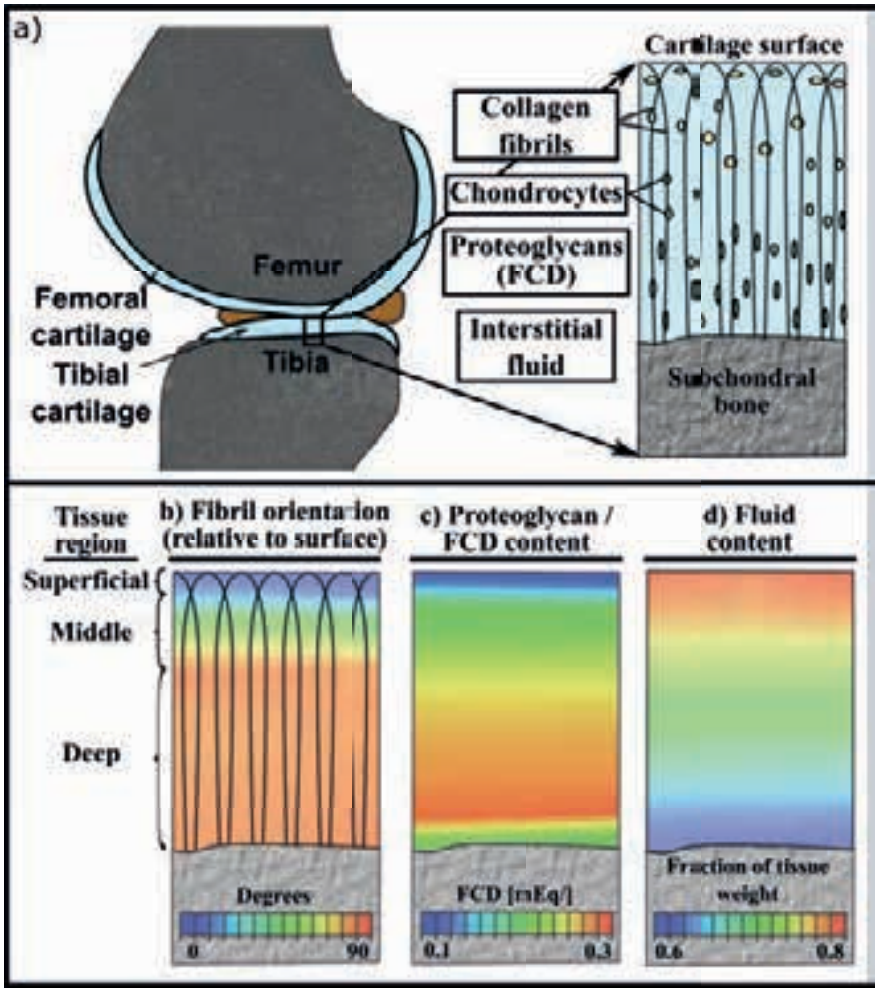


*Figure 2.2: Schematic representation of a) articular cartilage constituents and depth-wise variation in b) collagen fibril orientation, c) proteoglycan and FCD content and b) fluid content.*

### *Collagen fibril network*

Collagen fibrils are rod-shaped protein structures that form an organized, anisotropic network within the articular cartilage (Fig. 2.2 a,b) [1,37,39,40]. This fibrous network constitutes approximately 15-22% of cartilage wet weight and 60% of cartilage dry weight [33,34].

The collagen mesh is mainly composed of type II collagen fibrils (90-95% of the total collagen content), which are cross-linked by smaller, secondary, collagen fibrils (namely types IX and XI) [1,40]. The collagen fibril content and the orientation of the collagen fibrils vary with tissue depth and according to the likely orientation of stresses within the cartilage tissue [1,5,41]. A healthy articular cartilage can be divided depth-wise into three zones, *i.e.* superficial, middle and deep zones, based on the orientations of the primary collagen fibrils (Fig. 2.2b) [1,5,42–44].

The superficial zone of articular cartilage is characterized by a dense network of collagen fibrils that are organized in parallel to the articular surface [1,5,6,6,45]. In healthy, mature cartilage, the superficial zone accounts for approximately 3-20% of the total cartilage thickness, being thinnest in the main load bearing areas of the cartilages (*i.e.* tibiofemoral contact region) [1,6,21,41,46–49]. In the middle zone, the collagen fibrils bend tangentially from the parallel orientation present in the cartilage surface such that they will assume a perpendicular orientation in the deep zone [5,7,50–52]. The middle zone comprises approximately 15-60% while the thickness of the deep zone varies from 30% to 80% of the total cartilage thickness [1,21,46,48,49]. The collagen content increases from the cartilage surface towards the cartilage-bone interface [1,53].

### *Proteoglycans*

Proteoglycans make up approximately 4-7% of cartilage wet weight, and are thus the second major component of the solid phase of articular cartilage [1,8,9,37]. Proteoglycans are macromolecules with protein cores and covalently attached, negatively charged, glycosaminoglycan (GAG) side chains [1,34,38]. The proteoglycan content of cartilage increases from the cartilage surface towards the deep tissue, reaching its maximum at approximately 80% of the total tissue thickness (Fig. 2.2c) [1,8,9,53].

Proteoglycans are mainly bound or embedded inside the cartilage mesh by the collagen fibrils and therefore confer a fixed charge density (FCD) in the cartilage tissue [1,34]. The FCD of healthy

cartilage tissue (0.1 - 0.3 mEq/ml) parallels the content of proteoglycans, reaching its maximum in the deep tissue (Fig. 2.2c) [53,54]. The negative charge attracts cations, *e.g.* sodium, resulting in the attraction of water molecules into the tissue [1,34,38].

### *Chondrocytes*

Chondrocytes are cartilage cells that occupy approximately 1% of the volume of adult human articular cartilage (Fig. 2.2a) [34]. These cells mainly regulate the macromolecular content of cartilage tissue *e.g.* by synthesizing proteoglycans [34]. Chondrocytes also maintain and organize the fibrillar network and proteoglycans in the cartilage construct and respond to external and internal loads subjected to the cartilage tissue [34,55].

### *Fluid phase*

The interstitial fluid accounts for approximately 60-80% of the articular cartilage wet weight, and mobile ions [11, 37]. The fluid content is inversely proportional to the proteoglycan content, and fixed charge density, with approximately 80% at the cartilage surface and decreasing to 65% in the cartilage-bone interface (Fig. 2.2d) [1, 38, 56, 57]. The porous structure of the ECM allows fluid to flow through the cartilage surfaces which permits the exchange of nutrients with the synovial fluid [30,58,59]. Interstitial fluid also contains a high concentration of cations, *e.g.* sodium ($^{23}$Na) ions, that balance the negative fixed charge density of the tissue [38].

## 2.1.2 Biomechanics

The anisotropic variations in the constituents in articular cartilage result in spatial variations in the mechanical properties of cartilage tissue. The collagen fibril network, the proteoglycans and the interstitial fluid each exhibit their own characteristic mechanical properties and the cartilage response to mechanical loading is mainly determined by the interactions of these three major constituent [1].

Hence the mechanical properties of cartilage tissue vary with tissue depth and location [1].

### *Role of collagen fibril network*

The collagen fibrils are primarily responsible for the tensile, dynamic and shear properties of cartilage and they contribute to the fluid flow and pressurization of the cartilage tissue [1, 2, 7]. The organized structure of the collagen fibril network confers tensile stiffness and strength on the cartilage tissue and also restricts the swelling pressure subjected by the proteoglycans, providing the cartilage with its characteristic compressive stiffness [1]. Hence, the mechanical properties of cartilage are significantly dependent on both the architectural organization of the collagen fibrils and the density of the fibril mesh [60].

Collagen fibrils can resist deformations effectively in the direction of the fibrils [60]. Therefore, the dense layer of collagen fibrils in the superficial cartilage results in a high tensile modulus and strength in comparison to the deeper tissue [3, 4, 34, 61–65].

The inhomogeneous organization of the bending fibers in the middle cartilage depths allow large deformations and this results in a higher Poisson's ratio than in the superficial tissue [3]. It has also been suggested that the collagen fibrils in the middle regions bend in a parallel direction to the articular surface when under compression, reducing the vertical expansion of the tissue and increasing the tensile stiffness at those tissue depths [66]. The middle zone may therefore have a major role in resisting shear forces *e.g.* such as those occurring during joint movement [66].

The perpendicularly oriented fibrils in the deep tissue play a particularly significant role in conferring the transient stiffness on the articular cartilage [3, 4, 61, 63, 64]. The fibril orientation in the deep zone has been proposed to enhance the fluid flow and thus ensuring the transportation of nutrients from the deep zone to the superficial cartilage zones [67].

### *Role of proteoglycans*

The proteoglycans primarily determine the static compressive stiffness of cartilage tissue as the negative charge (FCD) leads to increased osmotic pressure and swelling of the tissue [1, 3, 11]. The swelling pressure exerted by the FCD also helps to maintain the ECM organization and allows the collagen network to withstand tensile loads by pre-stressing the collagen fibril network [1, 30]. Therefore, proteoglycans mainly determine the cartilage stiffness in a mechanical equilibrium [2].

### *Role of interstitial fluid*

The collagen fibril network, together with the FCD of proteoglycans, determine the permeability of cartilage matrix and therefore modulate the fluid flow within the cartilage tissue [37,59,68,69]. The fluid flow out of the tissue is minimal while the cartilage is under instantaneous or dynamic loading and the incompressible interstitial fluid resists the load [30, 68, 70, 71]. Hence, the instantaneous compressive stiffness of cartilage is mainly determined by the fluid and results in high dynamic stiffness and renders the cartilage to be a virtually incompressible tissue under impact loading [3,68,70,71]. During prolonged loading (*i.e.* creep loading), the fluid has enough time to flow within and out of the tissue and cartilage becomes slowly compressed [30]. Therefore, interstitial fluid is also responsible for the viscoelastic properties of cartilage [30,70].

## 2.2 OTHER KNEE JOINT TISSUES

### *Menisci*

Menisci are crescent-shaped fibrocartilage tissues located in the medial and lateral compartments of the knee joint capsule, between the femoral condyle and tibial plateau cartilages [31, 72, 73]. A cross-section of the menisci is wedge-like and their shape is adjusted to those of femoral and tibial contact surfaces. The lateral meniscus

covers a larger portion of the tibial cartilage plateau when compared to the medial meniscus [74]. The shape of the menisci is optimized to distribute the load to which the knee is being subjected by increasing the size of the contact area, thereby providing congruity for the articulation of the knee [75,76]. The meniscal horns are attached to the tibial bone in the intercondylar area.

The human meniscal tissue is primarily composed of water (60-72% of its wet weight), type I collagen (15-25%) and approximately 5% of non-collagenous substances, *e.g.*, proteoglycans [1,72,73]. The collagen fibrils in the menisci are oriented in an optimized fashion to withstand tensile forces and to transfer axial loading [77,78]. In detail, the collagen fibrils in the surface of the menisci are oriented radially along the meniscal wedge, while in the inner parts of the menisci, the fibril orientation is circumferential [75,77,79,80]. The FCD is notably smaller (approximately 0.03 mEq/ml) in meniscus, than in articular cartilage [1].

The mechanical properties of the menisci vary according to the collagen fibril orientations similarly to the situation in cartilage tissue. Thus, meniscal tissue is stiffest in the circumferential direction [81]. The tensile stiffness of the lateral meniscus is higher than that of the medial meniscus [73,81,82]. The tissues's tensile and compressive properties also vary with its location [81,83]. Generally the tensile stiffness of meniscus is higher than that of cartilage, while the equilibrium modulus is similar or lower [83].

### *Ligaments*

Ligaments are viscoelastic connective tissues that are mainly composed of collagen fibril bundles. They predominantly form bone-to-bone connections and thus they contribute to transferring tensile loads, thereby guiding the motion and stabilizing the joint [84]. The anterior and posterior cruciate ligaments (ACL and PCL, respectively) are intracapsular tissues running from the anterior and posterior intercondylar area of tibia to the posterior and anterior femur, respectively [85]. Their principal function is to stabilize the knee by restraining the flexion and posterior translations of tibia with re-

spect to femur [86, 87]. The lateral and medial collateral ligaments (LCL and MCL, respectively), on the other hand, are located in the lateral and medial side of the knee joint and their distal origins are found in the proximal tibia and fibula; they attach to the distal femur. LCL and MCL mainly work to stabilize the knee joint in the medial-lateral direction, restricting the varus-valgus motion [87].

## 2.3 OSTEOARTHRITIS AND ITS EVALUATION

Osteoarthritis (OA) is a severe joint disease characterized by the progressive degeneration of the articular cartilage structure that leads eventually to a total loss of cartilage [13, 14, 34]. OA causes alterations in the biomechanical function of the joint, reducing joint mobility and evoking pain [13, 14, 34]. The progression of OA is characterized by increasing collagen fibrillation and an elevated water content as well as a reduction in the proteoglycan content starting from the superficial cartilage in the early stages of the disease [12–14]. This disruption to the composition and structure of the cartilage matrix increases the permeability of the cartilage and decreases its stiffness [13, 14, 34, 45].

The condition of the knee joint, as well as the onset and progression of OA, can be investigated invasively or non-invasively with current clinical techniques. Arthroscopy is an invasive method in which the cartilage surface is imaged using an optical transducer inside the joint capsule. However, due to the invasiveness and the risk of infection associated with arthroscopy, non-invasive techniques are generally preferred. Radiography is a widely used imaging modality for the assessment of OA *e.g.*, via the evaluation of the narrowing of the joint space [88–90]. However, traditional radiological methods (*X-rays*) are unable to distinguish cartilage from synovial fluid due to their similar coefficients of attenuation, resulting in low sensitivity to determine cartilage loss [90–92]. On the other hand, magnetic resonance imaging (MRI) techniques are able to assess not only the health and thickness, but also the constituents of the cartilage, due to the major differences in contrast and relax-

ation parameters between the soft tissues (containing water) and bony structures (more details on this phenomenon will be provided in the next chapter) [93–95]. In spite of its benefits, MRI is generally a fairly time consuming and expensive methodology [93].

Although there are methods which can evaluate the onset and progression of OA, the diagnosis of OA is generally made too late to prevent the disease [96]. The symptoms of OA are commonly observed at a stage where the disease has already progressed to a point where a significant loss of cartilage and impairment of the mechanical function of the cartilage has already occurred [34,97,98]. In addition, although, the exact cause of OA is still unknown, overloading of the cartilage and cartilage trauma have been postulated to significantly increase the risk of OA [99,100].

The current, clinically used methods enable the assessments of OA symptoms and possible risk factors for progressing OA. However, they are not able to estimate the stresses and strains and their variations caused by the changes in the composition or in the geometry of the cartilage tissues during realistic, everyday loading scenarios. For that purpose, biomechanical, computational methods are needed.

# 3 Magnetic Resonance Imaging of Articular Cartilage

Magnetic resonance imaging (MRI) is a non-invasive imaging modality that provides excellent soft tissue resolution and, therefore, is well suited for imaging complex soft tissues such as the articular cartilage in the knee joint. In contrast to the other clinical imaging methods used for the assessment of cartilage condition and morphology, *e.g.*, computed tomography (CT), X-ray and arthroscopic techniques, MRI is a safe and non-invasive quantitative tool for the evaluation of the knee joint tissues without exposing the patient to harmful radiation. In addition, the wide availability of the MR imaging equipment and the vast number of MR imaging modalities, together with the excellent soft tissue resolution, have made MRI-based methods very popular for imaging the knee joint. MRI imaging has been widely used in the evaluation of cartilage lesions and pathological conditions [101–103], for structural and morphological imaging of articular cartilage [20–22, 48, 49, 104–107] and even for the estimation of the mechanical properties of cartilage tissue [19, 108–113].

This chapter presents some of the principles and techniques of MR imaging, related to the evaluation of articular cartilage composition. For more details on the principals and basic physics behind MRI, the reader is referred *e.g.* to [114, 115].

## 3.1 PRINCIPLES OF CLINICAL MRI

MRI is based on the phenomenon of nuclear magnetic resonance (NMR). In clinical set up, the subject is placed into a homogeneous external magnetic field ($B_0$, typically 1.5 or 3.0T, and up to 7.0T, magnetic field strength) in which the elemental nuclei that possess an uneven number of spin angular momenta, *i.e.*, spin (*e.g.*, nuclei

of hydrogen atoms ($^1H$) and sodium ions ($^{23}Na$)), will align with the direction of the $B_0$ field (*the equilibrium state*). The spinning nuclei form a net magnetization ($M_0$) that aligns with the $B_0$ -field and they start to rotate around the axis of the net magnetization at a frequency which is a characteristic of the nucleus (Larmor frequency, $\omega_0$).

The nuclei within the region of interest can be excited to the higher energy state by applying one or multiple radio frequency (RF) pulses or gradient pulses that tip the net magnetization away from the equilibrium orientation by a specific angle (*the flip angle*). Tipping the net magnetization away from the axis of the field at the equilibrium state also creates longitudinal and transverse vector components of the magnetization ($M_z$ and $M_{xy}$, respectively). The net magnetization recovers back towards the equilibrium after the application of the excitation pulse (a process known as *relaxation*), during which the nuclei exchange energy with each other (*spin-spin relaxation* or *transverse relaxation*), and with their molecular surroundings (*spin-lattice relaxation* or *longitudinal relaxation*) and emit RF -pulses, *i.e.*, the echos. The time that it takes for the longitudinal component of the net magnetization to revert back to the equilibrium state is known as the $T_1$ relaxation time, and the transverse decay time is known as the $T_2$ relaxation time. The relaxation process depends on the chemical and physical environments of the nuclei, and this results in varying relaxation times in different tissues and fluids in the human body.

Pulse sequences are used for defining the timing of the RF-pulses and gradient pulses (repetition time, $T_R$, time between consecutive excitation pulses) as well as timing when the tissue response to the pulses, *i.e.*, the acquisition of the signal (echo time, $T_E$), is measured. The pulse sequences can be roughly divided into spin echo (SE) and gradient echo (GRE) sequences depending on the method used for creating the echo. By varying the relaxation parameters in the pulse sequences, it is possible to distinguish between different tissue types and anatomical structures [104]. Images are then formed, *e.g.*, by applying Fourier transform methods

to quantify the information of the frequency and phase of the pulse that the nuclei emit during the relaxation.

## 3.2 ARTICULAR CARTILAGE STRUCTURE AND COMPOSITION FROM MRI

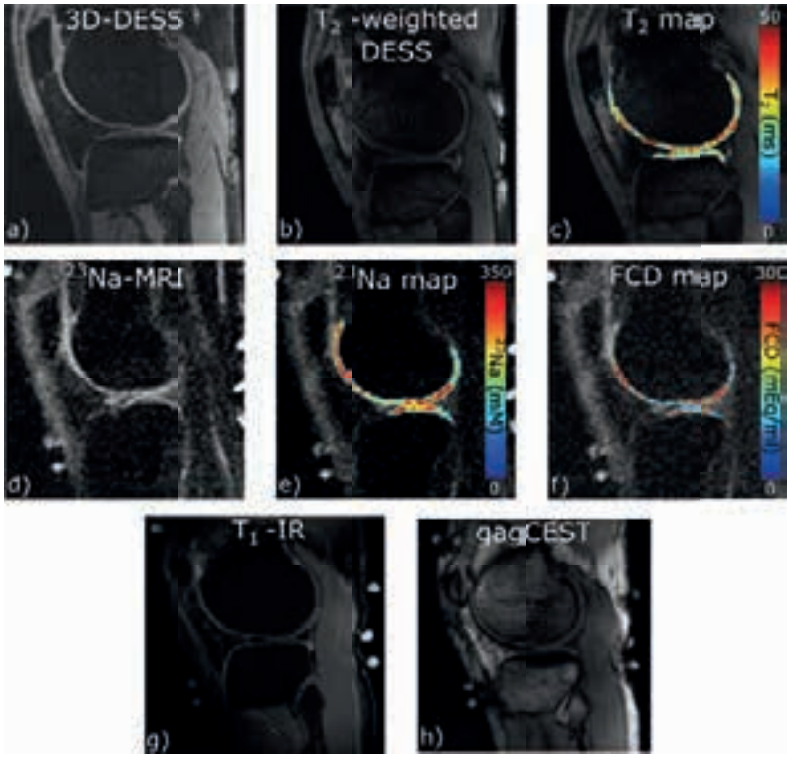


*Figure 3.1: A sagittal slice from the lateral tibiofemoral compartment of a knee joint of an asymptomatic male subject imaged at 7.0T with a) a proton density 3-D Dual-Echo Steady State sequence, b) $T_2$ weighted Dual-Echo Steady State sequence and c) calculated $T_2$ relaxation time map (from b)), d) Sodium ($^{23}$Na) MRI with Spoiled gradient recalled echo (SPGR) sequence and the calculated e) sodium and f) fixed charge density maps (from d)), g) an $T_1$ weighted Inversion Recovery sequence and h) GAG-specific Chemical Exchange Saturation Transfer image.*

The MR-imaging modalities provide a non-invasive means to assess cartilage morphology and the composition of cartilage matrix [16,

94,116–118]. For example, the standard clinical imaging sequences, *i.e.*, SE and GRE sequences in 2-D and 3-D, and more recently, *e.g.*, 3-D Dual-Echo Steady State (3D-DESS, Fig. 3.1a) and Spoiled gradient recalled echo (SPGR) sequences, are generally used for the evaluation of articular cartilage morphology [104, 118, 119]. However, specialized methods, such as $T_2$-mapping, sodium imaging ($^{23}$Na-MRI), gagCEST, dGEMRIC, $T_{1\rho}$-imaging and diffusion-weighted MR imaging, allow the evaluation of cartilage tissue composition [104].

### 3.2.1 $T_2$ -methods

$T_2$ relaxation time, *spin-spin relaxation* or *transverse relaxation*, is dependent on the vector component joining the nearby nuclei and hence is dependent on the orientation of the interacting nuclei [120]. In GRE sequences, the gradient magnetic fields are used for refocusing the spins after the initial excitation pulse, and this causes the rapid dephasing of the spins in the transverse plane. In this case, the transverse relaxation is denoted as $T_2^*$. In the general case, (a spin echo (SE) -pulse) the transverse relaxation process is exponential:

$$M_{xy} = M_{xy,0} \exp^{-T_E/T_2}, \tag{3.1}$$

where $M_{xy}$ is the apparent transverse magnetization, $M_{xy,0}$ is the transverse magnetization at equilibrium and $T_E$ is the echo time. While using GRE sequences, the transverse relaxation term ($T_2$) can be simply replaced by $T_2^*$.

Online mapping of the $T_2$ relaxation times ($T_2$ mapping, 3.1c) is becoming a more common method in clinical scanners, but the construction of relaxation time maps from multiple images increases the imaging time [104]. In order to minimize the imaging time, the imaging is usually conducted with either 2D multiecho sequences (multiecho spin-echo, *MESE*) [17, 120] or by using 3-D sequences *e.g.* 3D-DESS (Fig. 3.1b) [121, 122]. The multiecho sequences make use of multiple subsequent images, each taken with different echo times (*e.g.* $T_E$ of 10-100 ms) producing multiple images (e.g. 4-12 images per sequence) [17, 120]. $T_2$ maps can then be calculated by

fitting the signal intensities of each pixel in the image with a single, or multiple, exponential form of the signal decay equation as a function of the echo time ($T_E$, Eq 3.1) [104].

The signal intensity of $T_2$-weighted MR images varies with the cartilage tissue depth [22]. This behavior has been associated with the fluid content [123–126], and to a lesser extent with PG [127–131] and most importantly with the orientations of the collagen fibrils in the cartilage tissue [20, 22, 41, 120]. Specifically, the depth-wise changes in the collagen fibril orientations have been shown to account for approximately 60% of the depth-wise variation in the $T_2$ relaxation time in human articular cartilage [21]. The remainder may be attributable to the water content as well as to the concentration of PGs [21].

The capability of $T_2$ relaxation times to illustrate the collagen fibril organization in articular cartilage originates from the angular dependency of the relaxation time. The arrangement of collagen fibrils restricts the water flow through the cartilage tissue and causes the hydrogen nuclei of the fluid to arrange according to the orientation of the fibrils. The dipolar interaction between the adjacent, interacting nuclei is minimized when the nuclei are arranged at an angle of 54.7° with respect to the external $B_0$ -field, resulting in an increased $T_2$ relaxation time [120, 132, 133]. This behaviour is known as the *magic angle effect*, and the angle of 54.7° as the *magic angle* [132, 133]. Therefore, the anisotropic arrangement of the collagen fibrils leads to varying dipolar interactions throughout the cartilage depth and results in anisotropic variation of the $T_2$ relaxation time according to the collagen fibril orientations.

Usually, in the set-up used for MR imaging of cartilage, the external magnetic field $B_0$ is set to align with the orientation of the leg and the surface of the imaged articular cartilage is perpendicular to the $B_0$ field. In this set-up, the $T_2$ relaxation times are small in the superficial cartilage due to the parallel orientation of the collagen fibrils with respect to the $B_0$ field. The relaxation times increase significantly in the middle zone as the collagen orientations reach the magic angle and again decrease in the deep zone of the cartilage

as the orientation of the fibrils align with the $B_0$. The $T_2$ relaxation times have been reported to vary from 20-40 ms in the superficial zone to 10-20 ms in the deep cartilage tissue and to reach 50-120 ms in the middle zone of the cartilage [20, 22, 49]. In a healthy, adult human, this variation in $T_2$ relaxation times appears as a three-laminar structure in $T_2$-weighted MR-images and has been validated using histological methods in several studies. Therefore, it is possible to evaluate the collagen architecture through the almost bell-shaped, depth-wise $T_2$ relaxation time profiles throughout the tissue depth [20–22].

Local increases in $T_2$ relaxation time in articular cartilage have been associated with a degeneration of the cartilage matrix, this being attributed to increased collagen fibrillation and water content in the damaged cartilage lesion [17,94,104,134]. $T_2$ has also been correlated with the mechanical properties of cartilage [19, 111, 113, 126]. $T_2$-weighted imaging methods are clinically extensively available, fairly easily applicable and widely used for clinical investigation of cartilage condition and composition. $T_2$ mapping is generally regarded as the best method to measure collagen-related changes in cartilage composition [120, 135].

### 3.2.2 Sodium MRI ($^{23}$Na-MRI)

Sodium ($^{23}$Na) is a spin 3/2 nucleus, which allows it to interact with the external magnetic field similarly as hydrogen nuclei. However, due to the nonsymmetric distribution of charges in the sodium nucleus, it also exhibits a quadrupole moment and results in rapid bi-exponential transverse relaxation times in human soft tissues; short and long components of $T_2^*$ ($T^*_{2,SHORT}$ < 1.4 ms and $T^*_{2,LONG}$ < 15 ms) [18, 136–138]. Cartilage contains low sodium concentrations (200-300 mM) and sodium nuclei have a low gyromagnetic ratio (11.262 MHz/T) [116]. Because of these characteristics, the sensitivity of cartilage sodium MRI is only 9.3% that of the conventional proton MR sensitivity, the signal-to-noise ratio (SNR) and image resolution are low and imaging times are longer than those of proton MRI [116,138]. Furthermore, due to these factors, *in vivo* sodium

imaging requires higher magnetic field strengths (> 3 T), dedicated coils and optimized pulse sequences [127]. Cartesian 3D gradient echo (GRE) [23] and more recently variable echo time (vTE-GRE, Fig. 3.1d) [139, 140] and ultra-short echo time (UTE) [141] imaging sequences have been used in sodium MRI.

The negative fixed charge density of articular cartilage, caused by the GAG of PGs, attract positively charged sodium ions ($^{23}$Na) within the cartilage tissue [10, 142]. Therefore, the sodium concentration of the tissue is directly proportional to the FCD and to the GAG contents of cartilage and sodium MRI has been proposed as a highly specific imaging technique to illustrate these properties [10,23,142,143]. The advantage of sodium MRI is its high specificity to FCD and PG contents, through GAG, without the need of contrast agents [116, 143]. In addition, due to the low sodium content (< 50 mM) of the surrounding knee joint structures, the visualization of cartilage is possible with high tissue contrast [116].

In order to determine the GAG concentration and FCD in cartilage using sodium MRI, the sodium signal intensities need to be converted into sodium values of concentrations [144]. The quantification of sodium concentrations can be performed, *e.g.*, by measuring the subject simultaneously with agarose/saline phantoms (6–10% agar) containing known sodium concentrations [24]. Sodium concentration maps (Fig. 3.1e) of the cartilage can be calculated by fitting the cartilage sodium intensities pixel-by-pixel to a calibration curve, which is a linear fit between the signal intensity at the phantom regions and the known sodium concentrations of the phantoms [24, 138]. FCD (Fig. 3.1e) can be further derived from the sodium concentrations estimated according to Donnan equilibrium conditions between the synovial fluid and cartilage tissue in the knee joint [10].

Post-processing steps, *e.g.*, signal corrections for tissue water fraction [24, 25], $B_1$ inhomogeneity [18], mono- and biexponential $T_1$ and $T_2^*$ relaxations [137, 145, 146] and partial volume effect [147], have been demonstrated to improve the image quality and quantification of the sodium concentrations and FCD from sodium MRI.

In addition, fluid suppression techniques have been shown to improve the diagnostic capability of sodium MRI at 7 T, compared to a conventional ultra-short echo time imaging [141].

Sodium MRI has been validated *in vivo* for the quantification of the FCD distribution and the PG content of articular cartilage *in vivo* [24, 25, 148]. Sodium MRI has also been demonstrated to illustrate accurately the loss of PGs associated with osteoarthritis [25,127,145, 149,150] and to depict cartilage repair regions [17, 141, 151].

Sodium MRI is still a challenging technique and not used in clinical MR investigations. However, the recent developments in high-field MR systems (7 T) [141, 152, 153] and optimized MR sequences [154] can provide higher SNR, better resolution and shorter measurement times, making $^{23}$Na-MRI a more feasible and attractive method for imaging the composition of cartilage.

### 3.2.3 Other imaging modalities

#### $T_1$ *and dGEMRIC*

Similar to $T_2$, the $T_1$ relaxation times of cartilage tissues can also be mapped, for example by using saturation recovery (SR, repeated SE sequences) or inversion recovery (IR) sequences (Fig. 3.1g).

Native $T_1$ relaxation times remain relatively constant throughout the cartilage depth and are independent of the orientation of the tissue with respect to the magnetic field [155–157]. However, the native $T_1$ relaxation has been associated with the water content and thus also with the disruption of the cartilage tissue [158, 159].

The $T_1$ relaxation times correlate in particular with the PG content of cartilage when imaged together with gadolinium contrast agent (dGEMRIC) [104, 112, 159–161]. In delayed gadolinium enhanced MR-imaging of cartilage (dGEMRIC), negatively charged Gd-DTPA$^{2-}$ contrast agent is injected intravenously. After the injection, the contrast agent concentration is inversely proportional to the glycosaminoglycan (GAG) content in the cartilage due to the negative FCD [104, 143]. Cartilage regions with a high concentration of Gd-DTPA$^{2-}$ appear brighter in $T_1$ weighted image [104,112].

The $T_1$ values in the presence of gadolinium contrast agent have also been associated with the mechanical properties of the cartilage [111, 113, 162].

### *GAG-specific chemical exchange saturation transfer (gagCEST)*

Glycosaminoglycan specific chemical exchange dependent saturation transfer (gagCEST, Fig. 3.1h) imaging of cartilage makes use of the magnetization transfer (MT) effect between the bulk water of the tissue and the exchangeable protons bound to GAG [163]. The hydroxyl residues bound to GAGs are selectively excited in order to increase the contrast between cartilage regions with high and low GAG contents, thereby providing a direct measure of the GAG content within the articular cartilage [148, 163–165].

Despite its good specificity, previous studies have shown that gagCEST may not be feasible at lower than 7 T due to the variation of the relaxation properties of water at different field strengths [165]. In addition, the need for specific post-processing tools and complexity of the scanning make its clinical applicability somewhat limited [117, 148, 165].

### *Rotating frame methods - $T_{1\rho}$ and $T_{2\rho}$*

Relaxation process in a rotating frame of reference can be created by using a continuous wave (*CW*) RF pulse (*spin-lock pulse,* $B_{1,SL}$) or adiabatic RF pulses that lock the net magnetization into the transverse plane [18, 166]. The $T_{1\rho}$ and $T_{2\rho}$ relaxation times describe the longitudinal and transverse relaxation times, respectively, in the rotating frame around the $B_{1,SL}$ field (spin-lock method) or the $B_0$ (using an inverse adiabatic RF pulse) [18, 166]. Similar to the $T_2$ relaxation, the $T_{1\rho}$ relaxation times are directly proportional to the signal intensity in the final image [104, 167, 168].

The $T_{1\rho}$ relaxation time is sensitive to the interactions between water molecules and their adjacent molecular environment, *i.e.*, GAG [146, 169–172] and collagen content [104, 173, 174]. $T_{1\rho}$, and animal studies with $T_{2\rho}$, have demonstrated that the rotating frame relax-

ation times are sensitive to cartilage degeneration, even more so than $T_2$ [167,175–178]. However, it has also been postulated that $T_{1\rho}$ may not be sensitive to any particular constituent of cartilage [179]. Despite being an intriguing method for compositional evaluation of cartilage, rotating frame methods are not yet in common clinical use, *e.g.*, due to long imaging times and requirements for fairly complex imaging sequences [104].

# 4 Finite Element Modeling of the soft knee joint tissues

*Finite element modeling* (FEM) is a computational method that can be used for simulating the mechanics of complex structures and material models. FEM has been applied to simulate stress and strain distributions in human knee joints and has been proposed as an auspicious method for evaluating the properties of the knee joint such as its mechanics and even its condition [180, 181]. FE models of the knee have the potential to fill the void which is still inherent in the clinical imaging methods for diagnosing knee joint functions and progression of OA.

In the early FE models of the knee joint, the cartilage and meniscus tissues were modeled as isotropic or elastic materials [181–192]. The isotropic and elastic models generally fail to take into account the complex structure of cartilage tissue and constituents, and in particular, their spatial variation in the cartilage matrix [193]. The material models for cartilage and menisci were developed initially from the isotropic and elastic models, through biphasic (fluid and solid phases), transversely isotropic and poroelastic to fibril-reinforced biphasic models. The fibril-reinforced poroelastic (FRPE) and fibril-reinforced porovisoelastic (FRPVE) models are able to take into account the fibrillar (collagen fibrils) and non-fibrillar (PGs) phases in addition to tissue fluid and their spatial variation in the tissues [28, 193, 193–203]. Most recently, the FRPVE materials have been supplemented with tissue swelling properties (FRPVES), allowing the inclusion of the effect of FCD [55, 204].

In the latest iterations of knee joint models, the menisci have been modeled using transversely isotropic elastic [181, 194] or fibril-reinforced materials [195]. These materials allow the anisotropic properties of menisci, related to the circumferential collagen fibers, to be taken into account. Ligaments are mostly modeled as linear

or non-linear springs [28, 194, 205].

This chapter addresses the basics of FE modeling of the knee joint, placing an emphasis on the fibril-reinforced biphasic models of articular cartilage and their material properties. In addition, the previously-devised joint models and the applications and benefits of FE joint modeling are presented.

## 4.1 FIBRIL-REINFORCED POROVISCOELASTIC MODELING OF CARTILAGE

### *Poroelastic biphasic background*

The fibril-reinforced model properties are based on the biphasic model theory for cartilage that was first introduced by Mow et al. in 1980 [33]. The biphasic model divides the cartilage tissue into solid and fluid phases, which makes it possible to include the time dependent fluid flow in the tissue [1, 33]. The biphasic model also assumes that both the solid phase and the fluid phase are incompressible [1, 196]. The total stress is therefore expressed as a sum of the stresses in the solid matrix and the fluid [33, 206, 207]. For a more precise description, including the mathematics behind the poroelastic biphasic properties, the reader is referred to the original publication by Mow et al. [33].

### 4.1.1 Fibril-reinforced poroviscoelastic properties

In fibril-reinforced poroviscoelastic (FRPVE) materials the cartilage tissue is described as a biphasic material, where the solid phase is further divided into non-fibrillar and fibrillar components [203]. The non-fibrillar part describes the behaviour of the PGs, while the fibrillar component captures the behavior of collagen fibrils [196, 203].

### *Fibrillar matrix*

The viscoelastic (FRPVE, [203]) fibrillar network is characterized by the viscoelastic damping coefficient ($\eta$), the initial fibril net-

work modulus ($E_f^0$) and the strain-dependent fibril network modulus ($E_f^\varepsilon$). Therefore, the stress of a single fibril ($\sigma_f^i$) can be expressed as [203]:

$$\sigma_f^i = \begin{cases} -\frac{\eta}{2\sqrt{(\sigma_f^i - E_f^0 \varepsilon_f^i) E_f^\varepsilon}} \dot{\sigma_f^i} + E_f^0 \varepsilon_f + \left( \eta + \frac{\eta E_f^0}{2\sqrt{(\sigma_f^i - E_f^0 \varepsilon_f^i) E_f^\varepsilon}} \right) \dot{\varepsilon_f^i} & \varepsilon_f^i \geq 0 \\ 0 & \varepsilon_f^i \leq 0, \end{cases} \tag{4.1}$$

where $\varepsilon_f^i$ is the logarithmic fibril strain, $\dot{\sigma_f^i}$ and $\dot{\varepsilon_f^i}$ are the stress and strain rates.

The fibril network stress ($\sigma_f$) can be further divided into the stress components of primary and secondary fibrils. The primary fibrils are defined as the organized fibrils that form the arcade-like depth-wise architecture, while the secondary fibrils define the random orientation of the fibrils at each point [42, 43]. This allows the inclusion of more realistic fibril orientations into the model [193,196,197,203]. Hence, the fibril network stress is a sum of the individual primary ($\sigma_{f,p}$) and secondary ($\sigma_{f,s}$) collagen fibril stresses:

$$\sigma_f = \sum_i^{totf} \sigma_f^i \,, \tag{4.2}$$

$$= \sum_i^{totf,p} \sigma_{f,p}^i + \sum_i^{totf,s} \sigma_{f,s}^i \,, \tag{4.3}$$

$$= \rho_z \zeta \sum_i^{totf} \sigma_f^i + \rho_z \sum_i^{totf} \sigma_f^i \,, \tag{4.4}$$

where $totf$ is the total number of fibrils, $totf,p$ and $totf,s$ are the total number of primary and secondary fibrils, respectively, $\rho_z$ is the fibril volume fraction and $\zeta$ is the relative density of primary fibrils with respect to the secondary fibrils.

### *Non-fibrillar matrix*

The non-fibrillar matrix can be considered as an elastic [2,7,203,208] or neo-Hookean hyperelastic material [202]. For a linearly elastic

material, the matrix stress ($\sigma_{nf}$) is described, using the stiffness matrix $\mathbf{C}$ and the total elastic strain tensor $\varepsilon_{nf}$, according to Hooke's law:

$$\sigma_{nf} = \mathbf{C}\varepsilon_{nf}. \tag{4.5}$$

The neo-Hookean representation of the non-fibrillar stress enables the tissue matrix to exhibit larger deformations and material nonlinearities than the Hookean material [196, 203]. The neo-Hookean form of the non-fibrillar matrix stress ($\sigma_{nf}$) is:

$$\sigma_{nf} = K_m \frac{\ln(J)}{J}\mathbf{I} + \frac{G_m}{J}(\mathbf{F}\cdot\mathbf{F}^T - J^{\frac{2}{3}}\mathbf{I}), \tag{4.6}$$

where $J$ is the determinant of the deformation tensor $\mathbf{F}$, $K_m$ the bulk modulus and $G_m$ the shear modulus. The bulk and shear moduli can be expressed using the elastic modulus ($E_m$) and Poisson's ratio ($\nu_m$), respectively:

$$K = \frac{E_m}{3(1-2\nu_m)}, \tag{4.7}$$

$$G = \frac{E_m}{2(1+\nu_m)}. \tag{4.8}$$

The neo-Hookean model parameters also include permeability ($k$) which is dependent on the void ratios:

$$k = k_0\left(\frac{1+e}{1+e_0}\right)^M, \tag{4.9}$$

where $k_0$ is the initial permeability, $e_0$ and $e$ are the initial and current void ratios and $M$ is a material constant [202].

### *Total stress in FRPVE model*

In the FRPVE model, the stress in the tissue ($\sigma_{tot}$) is the sum of the fibrillar and non-fibrillar stress components ($\sigma_f$ and $\sigma_{nf}$, respec-

tively) and fluid pressure ($p$) [202–204]:

$$\sigma_{tot} = \sigma_{nf} + \sigma_f - p\mathbf{I}, \tag{4.10}$$

$$= \sigma_{nf} + \sum_{i}^{totf} \sigma_f^i - p\mathbf{I}\,. \tag{4.11}$$

### 4.1.2 Fibril-reinforced poroviscoelastic materials with swelling

The fibril-reinforced material models with swelling properties (fibril-reinforced poroviscoelastic swelling, FRPVES) take into account the fibrillar and non-fibrillar components of the tissue in a similar manner as the FRPVE models, but also include the effect of the fixed charge density ($c_{FCD}$) of the tissue. In the FRPVES models, the FCD can be expressed as a function of the tissue deformation gradient tensor **F** [202]:

$$c_{FCD} = c_{FCD,eq}\left(\frac{n_{f,0}}{n_{f,0} - 1 + J}\right), \tag{4.12}$$

where $c_{FCD,eq}$ is the initial fixed charge density at equilibrium, $n_{f,0}$ is the initial fluid fraction and $J$ is the determinant of the tissue deformation tensor (**F**) [202].

The FCD cause a swelling pressure gradient, also known as the Donnan osmotic pressure gradient, in the tissue [202, 209]:

$$\Delta\pi = \Phi_{int} RT\left(\sqrt{c_{FCD}^2 + 4\frac{(\gamma_{ext}^{\pm})^2}{(\gamma_{int}^{\pm})^2}c_{ext}^2}\right) - 2\Phi_{int} RT c_{ext}\,, \tag{4.13}$$

where $c_{FCD}$ is the fixed charge density, $\Phi_{int}$ and $\Phi_{ext}$ are internal and external osmotic coefficients, $\gamma_{int}^{\pm}$ and $\gamma_{ext}^{\pm}$ internal and external activity coefficients, $c_{ext}$ is the external salt concentration (0.15M), $R$ is the molar gas constant (8.3145 J/mol K) and $T$ is the absolute temperature (293 K).

The stress caused by the chemical expansion takes the form [210]:

$$T_C = a_0 c_{FCD} \exp\left(\kappa\frac{\gamma_{ext}^{\pm}}{\gamma_{int}^{\pm}}\sqrt{c^-(c^- + c_{FCD})}\right), \tag{4.14}$$

where $a_0$ and $\kappa$ are material constants and $c^-$ is the mobile anion constant [202]. The chemical expansion stress describes the stress in the solid tissue matrix caused by the repulsion of negative charges within the tissue [210].

### *Total stress in FRPVES model*

The total stress ($\sigma_{tot}$) in the FRPVES material is the sum of the fibrillar ($\sum_i^{totf} \sigma_f^i$) and non-fibrillar ($\sigma_{nf}$) stresses and the stresses caused by the osmotic pressure ($\Delta\pi$, 4.13) and the chemical expansion stress ($T_C$, 4.14) [202]:

$$\sigma_{tot} = \sigma_{nf} + \sum_i^{totf} \sigma_f^i - \Delta\pi\mathbf{I} - T_C\mathbf{I} - \mu^f\mathbf{I}\,. \tag{4.15}$$

where $\mu_f$ is the electrochemical potential of water [210] and $\mathbf{I}$ is a unit tensor.

## 4.2 APPLICATIONS AND BENEFITS OF THE KNEE JOINT MODELS

Cartilage mechanics have been widely studied and, *e.g.*, the cartilage and meniscus tissue strains have been measured *in vivo* during static loading of the knee [108, 110, 195, 211, 212]. However, the assessment of stresses and strains in articular cartilage is not possible *in vivo* in an intact knee joint during dynamic loading such as during gait. FEM has been used to illustrate the mechanics and function of the knee joint and the knee joint cartilage in a number of studies [180, 187, 213, 214]. The studies have shown that FEM can be used to describe accurately knee joint functions, cartilage response to loading and even condition of the knee [180, 181].

The 2-D and 3-D geometries of the articular cartilage obtained from MR or computed tomography (CT) images have been used in FE knee joint models [181–192, 215–218]. These isotropic and elastic 3-D joint models have been used extensively *e.g.* for investigating tibiofemoral contact in the knee joint by changing the joint alignment [182, 190], joint kinematics and flexion [215–218] and joint me-

chanics under dynamic loading [184, 185, 191]. However, the elastic and isotropic models have been demonstrated to be unable to simulate the cartilage response under impact loading of the knee joint [193] and those cannot take into account the anisotropic structure and material properties of cartilage tissue. Therefore, more recently cartilage has been modelled using fibril-reinforced poroviscoelastic (FRPVE) or fibril-reinforced viscoelastic (FRVE) material properties incorporated with anisotropic distribution of collagen fibrils, proteoglycans and fluid [105, 193–195, 197, 199–201, 219–221].

The FRPVE joint models of human have been used to investigate the effect of cartilage constituents on cartilage and joint mechanics in various loading schemes, both in 2-D [193, 196] and 3-D [194, 197, 200, 205, 219]. Julkunen et al. (2008) [105] demonstrated the effect of collagen orientations, as obtained from MRI of *in vitro* human cartilage samples, on the mechanical response of cartilage. The studies conducted by Shirazi et al. (2008) [205], Mononen et al. (2012) and Gu et al. (2011) have emphasized the importance of the anisotropic structure of the collagen fibrils and that their splitline orientations in human knee joint cartilage control the stress distribution, as well as the fluid flow in the knee joint cartilage, respectively.

Knee joint models can also be used for the evaluation of joint disorders and condition, as well as the outcome of joint operations. Mononen et al. (2011, 2012) noted that the progressive depthwise [193] and spatial [197] fibrillation of the cartilage matrix altered the cartilage stresses and could reveal possible failure sites associated with the early stages of OA [222] in the cartilage tissue. Furthermore, the increased collagen fibrillation also increased the collagen fibril stresses and lead to increased fibril strains [193, 197]. Mononen et al. (2012, 2013) and Zielinska & Donahue (2006) investigated the effects of bilateral meniscectomy [197, 198], partial meniscectomy [28, 192] and radial tears in menisci [28] on the joint response to loading. The study of Kazemi et al. (2011) [223] also demonstrated, that meniscectomy slowed the dissipation of fluid pressures and produced higher tension in the collagen network of

the cartilage, than that observed in a healthy joint. The effect of total knee arthroplasty and total knee replacement [224,225] and the impact of ACL rupture and reconstruction have been studied on knee joint function and on the distribution of loads in the joint [226,227]. Also, recently Venäläinen et al. (2014) investigated the effect of bone porosity that can be associated with osteoporosis on knee joint cartilage mechanics [201].

One common result observed in all the models evaluating joint disorders is the increased cartilage stress, which inevitably leads to increased fibril strains [28, 197, 214, 223]. Since the tissue stress is dependent on the collagen fibril orientations and, possibly, on the swelling of the tissue [196,197,204], a method to obtain the subject-specific variation of the cartilage constituents and implement it into the model might achieve a more specific estimate of the condition of the joint. Even though realistic and subject-specific joint geometries have been used in the studies mentioned above, the subject-specific structure of articular cartilage has been mostly neglected.

### *Imaging combined with modeling of the knee joint*

The combination of clinical imaging and biomechanical FE modeling has been proposed as a valid and feasible noninvasive technique for the diagnostics of OA. As stated in the previous chapters, the joint response to loading is dependent on the composition of articular cartilage which can vary extensively between subjects, *e.g.*, depending on the joint condition [53,228].

It is possible to conduct a non-invasive evaluation of cartilage structure and composition, *e.g.*, collagen fibril network, orientation and PG or FCD distributions and contents, with the use of clinically-available imaging modalities, such as MRI. The clinical imaging modalities are also capable of revealing spatial and local variations in the cartilage tissue composition.

By implementing the cartilage structure into a biomechanical model, it is possible to investigate the stress, strain and pressure distributions in the knee joint in a non-invasive, subject-specific manner. Modeling methods could also pinpoint possible failure

sites in the joint cartilage, *e.g.*, due to local variations or defects in the cartilage composition during specific activities. These methods could therefore act as a tool to determine optimal treatment to apparent joint dysfunctions and to diagnose the early stages, progression or the onset of OA.

Nonetheless, the subject-specific cartilage structure has not been implemented into a biomechanical modeling before. The methods presented here may thus provide a novel technique for the prevention and diagnostics of osteoarthritis in a subject-specific manner.

# 5 Aims

In this thesis, subject-specific collagen architecture and FCD distributions are determined using MRI and are implemented into biomechanical models of the knee joint. This is done in order to assess the influence of subject-specific spatial variation in cartilage composition on knee joint stresses and strains.

The methods used and developed in this thesis can provide a more accurate, non-invasive tool for the subject-specific assessment of the joint mechanical properties, condition and possible risks related or leading to OA in a knee joint.

**Specific aims of the thesis:**

**Study I** To determine the subject-specific collagen fibril orientations in tibial cartilage from clinical $T_2$-weighted MRI and then to implement this information into a 2-D model of the knee joint. Furthermore, the aim was to investigate the effect of the depth-wise and local variations in collagen fibril orientations on the knee joint response to dynamic loading.

**Study II** To determine the collagen fibril orientations in 3-D in tibial cartilage, using clinical $T_2$-weighted MRI, and implement it into a 3-D joint model of the same subject. A further aim was to examine the effect of the spatial and local variation of the collagen fibril orientations on the distribution of stresses and strains during gait.

**Study III** To determine the spatial 3-D variation of FCD in tibial cartilage from sodium MRI and to implement it into a 3-D joint model of the same subject. The effect of the spatial variation of FCD on the distribution of stresses and strains was investigated during standing in tibial cartilage.

**Study IV** To investigate the effect of FCD and tissue swelling on the cartilage response to dynamic loading, *i.e.*, gait, in a 3-D model of the joint.

# 6 Materials and methods

This chapter summarizes the methods used in this thesis to create the subject-specific knee joint models, and also describes the methods used to analyze and implement the cartilage structure from MRI to the knee joint models and the simulations performed in studies **I** to **IV**.

## 6.1 CARTILAGE STRUCTURE AND TISSUE DEFORMATION FROM MRI

MRI was used in all studies to create the model geometries as well as for determining the collagen architectures and FCD distributions of knee joint cartilages of the corresponding test subjects (Fig. 6.1). All of the imaged subjects were asymptomatic males (providing informed consents) and the imaging parameters were chosen in order to optimize the imaging resolution and SNR for the intended purpose.

### 6.1.1 Magnetic resonance imaging and segmentation

**Study I:** MR data of a healthy right knee joint of a healthy male patient (46 -years-old male, weight 84.6kg) was obtained from the Osteoarthritis Initiative (OAI) database, image dataset 0.E.1). The MR imaging was performed with a 3T magnet (Siemens Trio, Erlangen, Germany) using a multi-echo spin-echo (MESE) imaging sequence ($T_R$ = 2.7 s and seven $T_E$'s between 10.0 and 70.0 ms, in-plane resolution 0.322 mm and slice thickness 3 mm, Fig. 6.1a,b). TpsDIG2 software (v2.05) was used for manual segmentation of the femoral and tibial articular cartilages and menisci from a sagittal slice located in the middle of the tibiofemoral contact area in the knee joint (Fig. 6.1a) [193].

*Figure 6.1: Summary of the methods used for the creation of the subject-specific models in studies* **I-IV** *starting from a) cartilage tissue segmentation from MRI, to b) determination of the cartilage tissue structure and finally to c) the final model geometry and FE meshing. RP = the reference point located between the femoral epicondyles in all studies, into which the simulated loading is applied.*

***Study II***:
The left knee joint of a 28-year old, healthy male subject (weight: 80kg) was imaged using a 3T MRI scanner (Oulu University Hospital; Siemens Skyra, Siemens Healthcare, Erlangen, Germany). The knee joint was imaged with a proton density weighted double echo steady state (DESS) sequence (0.5mm isotropic voxel, $T_R$ = 1.2 s and $T_E$ = 28 ms, bandwidth (BW) of 76.8 kHz and a total imaging time of 7 minutes 55 seconds, Fig. 6.1a). Tibial and femoral cartilages, as well as menisci, were manually segmented from the DESS data set (whole set, 3-D) using Mimics software (v15.0, Materialise, Leuven, Belgium). The subject was further imaged with multi echo spin echo (MESE) $T_2$ mapping sequence (in-plane resolution 0.34 mm, slice thickness 2.4 mm, $T_R$ = 1.3 s and $T_E$ = 13.8, 27.6, 41.4, 55.2 and 69.0 ms, BW = 88.32 kHz; the total imaging time was 8 minutes 22 seconds, Fig. 6.1b).

***Studies III and IV***:
All the imaging was performed on the left knee joint of an asymptomatic 39 years old male volunteer (weight 69.6 kg), using a 7T MRI scanner (Siemens Magnetom, Erlangen, Germany) and a dedicated knee coil. The scans were performed on two consecutive days (Day 1 and 2). First (Day 1), the knee joint was imaged using a 3D-DESS sequence ($T_R/T_E$ = 7.81/2.62 ms, 0.34 mm isotropic voxel, Fig. 6.1a). Second (Day 2), the same knee was subjected to a 120 N axial compression using a MR-compatible pneumatically controlled compression device [229]. The joint was further imaged 13 minutes after the application of the load, while keeping the load constant through the scan (3D-DESS: $T_R/T_E$ = 8.86/2.55 ms, 0.4 mm isotropic voxel). The same imaging parameters were initially used on both days for the 3D-DESS sequences. However, the 3D-DESS sequence on Day 2 was reoptimized to achieve optimal SNR for segmentation purposes. The femoral and tibial cartilages, menisci and ligament attachments (ACL, PCL, MCL and LCL) were manually segmented from the 3D-DESS data sets of the unloaded and compressed joint using Mimics software (v15.0, Materialise, Leuven, Belgium).

Sodium ($^{23}Na$) MR imaging of the subject was performed using spoiled gradient echo sequence with variable echo time scheme (vTE-SPGR) at 7T ($T_R$ = 11 ms, $T_{E1}$ = 1.42 ms, flip angle ($\phi$) = 33°, resolution 1.5 x 1.5 x 2.8 mm$^3$, Fig. 1d, Fig. 6.1b) [139]. For the calibration of the cartilage sodium concentration, six small cylindrical phantoms, filled with 10% agarose/saline solution and containing known concentrations of sodium (100 - 350 mM), were imaged simultaneously along with the subject. In addition, in order to depict the magnetic field inhomogeneity, a large cylindrical phantom, covering the knee field of view in the images, filled with $^{23}$Na solution was imaged subsequently with the same imaging set-up. The sodium images were acquired using a 15-channel sodium-only knee array coil (QED, Quality Electrodynamics LLC, Cleveland, OH).

### 6.1.2 Collagen architecture from $T_2$ maps of MRI

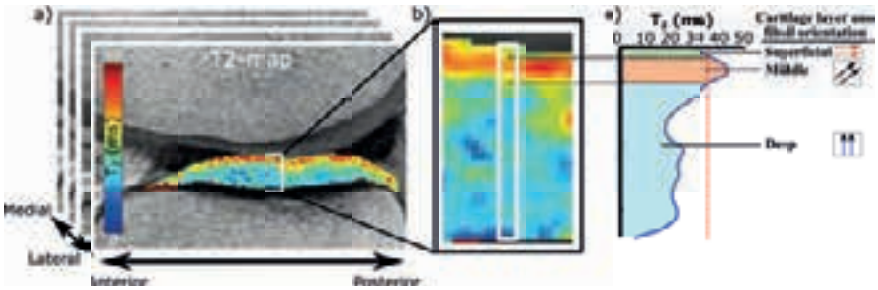


*Figure 6.2: Determination of collagen architecture (and cartilage layers) from $T_2$ mapped MRI: a) $T_2$ mapped region of interest (ROI) of tibial cartilage, b) a close-up of the tibial cartilage and c) a depth-wise $T_2$ profile and the layer boundaries from a single vertical line in the cartilage ROI.*

***Study I***:
$T_2$ map of the tibial cartilage (Figs. 6.1b,6.2a,b) was calculated by fitting the mono-exponential form of the relaxation equation (Eq. 3.1) into the pixel intensities of the MESE data set. The patient-specific collagen architecture (three laminar structure; superficial, middle and deep zones) of tibial cartilage was determined along the segmented cartilage width from depth-wise $T_2$ profiles (sagittal

slice, 2-D).

***Study II***:
The methodology used in this study was the same as in Study **I**. Again, $T_2$ maps of the cartilage tissues were calculated from the $T_2$ mapped MR-images (MESE) with an in-house MATLAB (MathWorks Inc., Natick, MA) script assuming a mono-exponential decay (Eq. 3.1, Fig. 6.1b). The patient-specific collagen architecture of tibial cartilage tissue was determined based on the depth-wise $T_2$ profiles of each sagittal MRI slice (whole joint, 3-D) through the tissue length in a pixel-wise manner.

In both studies (**I** and **II**), three zones, *i.e.*, superficial, middle and deep [41], were determined using a custom made Matlab (MathWorks Inc., Natick, MA, USA) script. The first laminar boundary, *i.e.*, the interface between the superficial and middle zone, was determined by locating the half–maximum of the rising part of each (ideally) bell-shaped $T_2$ profile throughout the tissue geometry (Fig. 6.2c) [22]. Correspondingly, the interface between the middle and deep zones was localized to the corresponding $T_2$ value at the descending part of the profile (Fig. 6.2c) [22].

Each zone was assumed to have a specific fibril orientation [5]. The low $T_2$ values in the superficial zone were assumed to indicate fibrils oriented in parallel to the cartilage surface, the high $T_2$ values referred to the randomly oriented (study **I**) or bending (study **II**) collagen fibrils and the low $T_2$ values in the deep zone collagen fibrils aligned perpendicularly to the cartilage surface.

### 6.1.3 Fixed charge density from sodium MRI

***Studies III and IV***:
The FCD distribution of tibial cartilage was determined from sodium MRI. All of the sodium images (Fig. 6.3a) were corrected for the attenuation of the initial signal intensity ($S_0$) due to magnetic field inhomogeneity ($B_1$), partial volume effect (PVE) (Moon et al., 2013), biexponential $T_2^*$ and monoexponential $T_1$ relaxations.

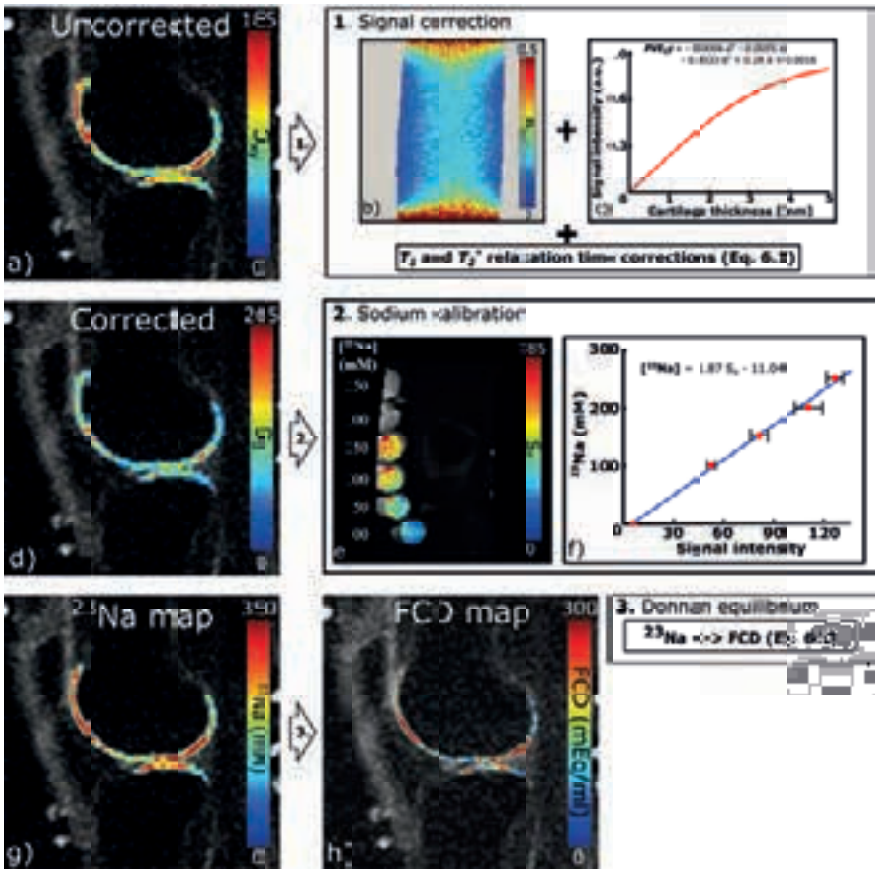


*Figure 6.3: Post-processing steps and calculation of sodium and fixed charge density maps from sodium MRI: a) original (uncorrected) sodium MR slice, signal attenuation corrections: b) $B_1$ magnetic field inhomogeneity (correction factors from a sodium phantom), c) partial volume effect correction with respect to tissue thickness at 2.5mm resolution [147] and exponential $T_1$ and biexponential $T_2$ relaxations (Equation 6.1), d) the same sodium slice after the signal corrections. e) Sodium calibration phantoms which were used to obtain the f) calculated calibration curve. g) The sodium map calculated using the calibration curve. h) The fixed charge density map calculated assuming an ideal Donnan equilibrium (Equation 6.2).*

First, each $^{23}$Na MRI slice was corrected for $B_1$ magnetic field inhomogeneity by multiplying the slices pixel-by-pixel with a correction map calculated using the cylindrical phantom filled with $^{23}$Na solution. The $B_1$ correction factors ($B_{1,cf}$, Fig. 6.3b) were calculated

pixel-by-pixel from the phantom ROIs by dividing the observed signal intensities by the maximum signal intensity of the whole image stack (from the phantom ROI).

Second, the relaxation times of the tibial cartilage tissue regions were corrected using a spoiled gradient echo signal equation with monoexponential $T_1$ and biexponential $T_2^*$ signal decays [25,137,145]. Therefore, the biexponential form of the signal equation includes the $T_1$ relaxation of the tissue ($T_1$ = 20 ms), the short and long components of the $T_2^*$ relaxation ($T^*_{2,short}$ = 0.9 ms and $T^*_{2,long}$ = 13.3 ms, respectively) and the amplitudes of the $T_2^*$ exponential terms ($A_{short}$ = 0.34 and $A_{long}$ = 0.66, respectively) [137].

Third, the signal attenuation due to the PVE was corrected using correction factors ($PVE_{cf}$). Those were obtained by determining the mean tibial and femoral cartilage thickness ($d_{tibia}$ = 2.8 ± 0.9 mm, $d_{femur}$ = 2.5 ± 0.8 mm) from the 3D-DESS images and fitting them to a function describing the attenuation of signal intensity due to the PVE at 2.5 mm resolution ($PVE_{cf} = -0.0004d^4 - 0.0055d^3 - 0.0033d^2 + 0.28d + 0.0016$, Fig. 6.3c) [147]. The correction factors were calculated separately for each MR slice, where the tibial cartilage was visible.

Fourth, the signal intensities were divided with the average water fraction ($n_f$ = 0.75) [59]. Hence by combining the postprocessing steps, the correction was performed to the observed signal intensities ($S_{xy}$, Fig. 6.3a) according to the following equation (Equation 1):

$$S_0 = \frac{1 - \cos\theta(exp^{-T_R/T_1})}{(1 - exp^{-T_R/T_1})\sin\theta(A_{short}exp^{-T_{E,1}/T^*_{2,short}} + A_{long}exp^{-T_{E,1}/T^*_{2,long}})} * \frac{B_{1,cf}(x,y)}{n_f PVE_{cf}} S_{xy}(x,y)\,, \quad (6.1)$$

where $S_0$ (Fig. 6.3d) is the corrected signal intensity, $\theta$ is the flip angle, $T_R$ and $T_{E,1}$ are the repetition and echo times, $T_1$ is the spin-lattice relaxation of the tissue, $T^*_{2,short}$ and $T^*_{2,long}$ are the short and long components of the $T_2^*$ relaxation, $A_{short}$ and $A_{long}$ are amplitudes of the $T_2^*$ exponential terms and $n_f$ is the average fluid frac-

tion of the tissue.

In order to quantify the sodium concentrations from the signal intensities, a calibration curve was created by plotting the known sodium concentrations of the four agarose phantoms ($[^{23}Na]$ = 100-250 mM, Fig. 6.3e) against the corrected signal intensity (monoexponential $T_1$ (30.1 ms) and $T_2^*$ (6.2 ms)) of the phantoms (mean values for each phantom throughout the image stacks) and the mean background noise ($[^{23}Na]$ = 0 mM). A sodium calibration curve ($[^{23}Na](x,y) = 1.87S_0 - 11.04$, Fig. 6.3e) was calculated by performing a linear fit to the plotted data [24]. Sodium maps for the tibial cartilage tissues ($[^{23}Na]$, Fig. 6.3f) were then calculated by fitting the corrected signal intensities ($S_0$) pixel-by-pixel to the linear sodium calibration curve [24].

Finally, FCD of the tissue (Fig. 6.3g) was calculated according to the ideal Donnan equilibrium conditions, with respect to the sodium concentration of synovial fluid ($^{23}Na_{sf}$ = 150 mM) [10, 24, 230]:

$$FCD(x,y) = \frac{[^{23}Na_{sf}]^2}{[^{23}Na(x,y)]} - [^{23}Na(x,y)]\,, \tag{6.2}$$

where $FCD(x,y)$ is the fixed charge density of the tissue (pixel-by-pixel) and $[^{23}Na_{sf}]$ is the sodium concentration of synovial fluid.

### 6.1.4 Tibial cartilage deformation under 120 N load

In order to validate the deformation of the subject-specific joint model in study **III**, the same male subject was imaged while the knee joint was subjected to an axial load of 120 N (as described above) [229]. The experimental deformation of tibial cartilage in the subject was measured from the tibiofemoral contact region of both medial and lateral tibial cartilages from the 3D-DESS data obtained 13 minutes after the application of the load. First, the cartilage-bone interfaces from tibial cartilage of the uncompressed and compressed MR data were coregistered using a custom-made ICP algorithm. Second, the tibial cartilage thicknesses were measured at the tibiofemoral contact regions from both uncompressed

and compressed MR data sets. Finally, the relative deformation (strain) was obtained by subtracting the compressed tissue thickness location-wise from the uncompressed thickness and dividing it with the corresponding uncompressed tissue thickness.

## 6.2 MODEL PARAMETERS

### 6.2.1 Model geometries and finite element meshes

In all studies, the manually segmented tissue geometries (from MRI, Fig. 6.1c) were imported via Matlab into the FE modeling package (Abaqus v6.12, Dassault Systèmes, Providence, RI, USA).

In study **I**, a finite element mesh was created for the segmented 2-D tissue geometry using porous plane strain elements of type CPE4P11 with the characteristic element length of 0.7 mm (Fig. 6.1c). In study **II**, the 3-D tibial and femoral cartilage and meniscus geometries were meshed with linear 8-node porous brick elements (C3D8P), with an average characteristic element length of 0.8 mm for the femoral cartilage and 0.6 mm for the tibial cartilage (*global model*, *i.e.* a 3-D model of the whole joint, Fig. 6.1c). Furthermore, a submodel was created to the medial tibial compartment in order to investigate how the more precise implementation of the cartilage structure into the model affects the local model results. The submodel was located in accordance with the $T_2$ mapped MR-slices and its width was 2.4 mm, equal to the slice thickness of the MR-images, and was meshed with an average characteristic element length of 0.3 mm corresponding to the resolution of the $T_2$ mapped MR-images (Fig. 6.1c).

In studies **III** and **IV**, the 3-D tibial and femoral cartilage and meniscus geometries were meshed with linear 8-node porous brick elements (C3D8P) to form the global joint model (3-D model of the whole joint tissues, characteristic element length in tibial cartilage was 0.6 mm, Fig. 6.1c). In study **III**, the cartilages of the medial and lateral tibial compartments were further meshed with denser mesh to form the medial and lateral compartment models (average characteristic element lengths 0.3 mm in tibial cartilage, Fig. 6.1c).

In the compartment models, the mesh of the femoral cartilage and meniscus were identical to those in the joint level model, but the ligaments were removed. The compartment models were created in order to use a denser mesh and achieve a more precise implementation of the fibril orientations.

### 6.2.2 Material parameters

In studies **I** and **II**, femoral and tibial cartilages were modeled as fibril-reinforced poroviscoelastic (FRPVE, Table 6.1) and in studies **III** and **IV** as FRPVE with swelling (FRPVES, Table 6.1). In all studies, the fluid fraction in the cartilage tissues was considered to be depth-dependent [35]. In studies **III** and **IV**, the depth-dependent variation in the collagen content was also included [53].

The collagen fibrils consisted of four primary fibrils with depth-dependent architectures and evenly distributed secondary fibrils orienting in 13 directions. The cartilage tissues were implemented with three-laminar primary fibril architectures with the fibrils oriented in parallel to the cartilage surface in the superficial zone, randomly (study **I**), in 45° (study **II**) or tangentially bending (Studies **III** and **IV**) in the middle zone and perpendicular to the cartilage surface in the deep zone. The zone thicknesses in tibial cartilages were defined either from MRI (Studies **I** and **II**, Table 6.2) or from previous studies (Table 6.2). In all studies, the femoral cartilages were implemented with the collagen fibril architectures obtained from the literature; the thicknesses of the superficial, middle and deep zone were 12%, 26% and 62%, respectively, of the total cartilage thickness [220]. In addition, in studies **II** to **IV**, the radial split-line orientations of the fibrils were included in all models in both tibial and femoral cartilages [50,197,231]. The FCD distributions in tibial cartilage from MRI and literature [53, 228] were included in studies **III** and **IV** (as discussed above, Table 6.2), while the FCD distributions in femoral cartilages were the same as previously presented in literature [53,228].

The menisci were modeled as FRPVE (study **I**), transversely isotropic (study **II**) and FRPES (studies **III** and **IV**). In study **I**,

the superficial layers of the meniscus were implemented with the collagen fibrils oriented in parallel to the meniscus surface and randomly in the deeper meniscus. In study **II**, the menisci were transversely isotropic elastic with the Young's modulus set to 20 MPa in the axial and radial directions and to 140 MPa in the circumferential direction, Poisson's ratios to 0.2 in-plane and 0.3 out-of-plane and with a shear modulus of 50 MPa out-of-plane [181, 192]. In studies **III** and **IV**, the menisci were implemented with the collagen fibrils oriented circumferentially at all depths of the menisci [195] and the FCD was constant (0.03 mEq/ml) [1]. In studies **II-IV**, the meniscal horns were fixed to bone using linear spring elements (element type SPRINGA) with a total stiffness of 350 N/mm at each horn [195, 232].

Ligaments were not included in the models in studies **I** and **II** and in the compartment models in study **III**, but their effect had been already included in the loading inputs as well as in the rotations and translations of femur with respect to tibia as obtained in previous experimental studies [222, 233–235] and from the global joint models, respectively. In studies **III** and **IV**, the ligaments in the global joint models were modeled using non-linear spring elements that were connected between the attachment points located at the femoral and tibial bones. The ligaments were assumed to be pre-elongated (ACL and PCL = 5%; MCL and LCL = 4% of the unloaded length) at the segmented length [195, 236]. The stiffness of the ligaments (ACL 108 N/mm, PCL 135 N/mm, MCL 81 N/mm and LCL 53 N/mm) were scaled from those presented by Momersteeg et al. (1995) in a way that the total force subjected to the tibial cartilage from the ligaments was approximately half of the body weight, a total of 322 N [195, 214, 233, 235, 237]. Therefore, the total force to which the tibial cartilage was subjected was the load applied as the reference force during the simulations added with the force produced by the ligaments.

In the submodels, the material parameters were identical to those in the global models described in study **II** and in compartment models to those in the global joint models in study **III** (Tables

6.1 and 6.2).

*Table 6.1: FRPVE and FRPVES material parameters used in the studies for femoral and tibial cartilages ("Cartilage") and menisci.*

| | Study I | | Study II | Studies III & IV | |
|---|---|---|---|---|---|
| **Parameter** | **Cartilage** | **Meniscus** | **Cartilage** | **Cartilage** | **Meniscus** |
| Material | FRPVE[1] | FRPVE[1] | FRPVE[1] | FRPVES[2] | FRPES[3] |
| $E_m$ (MPa) | 0.31 | 0.075 | 0.31 | 0.31 | 0.253 |
| $E_f^0$ (MPa) | 0.47 | 0.47 | 0.47 | 2.737 | 49.93 |
| $E_f^\varepsilon$ (MPa) | 673 | 673 | 673 | 867.7 | - |
| $\nu_m$ | 0.42 | 0.30 | 0.42 | 0.01 | 0.30 |
| $\eta$ (MPas) | 947 | 947 | 947 | 1418 | - |
| $k_0$ ($10^{-15}$ $m^4$/Ns) | 1.74 | 1.26 | 1.74 | 1.522 | 0.08 |
| $M$ | 7.1 | 7.1 | 5.09 | 5.661 | 12.1 |
| $n_f$ | 0.9-0.1$h_z$ | 0.85 | 0.8-0.15$h_z$ | 0.8-0.15$h_z$ | 0.72 |
| $\rho_{c,tot}$ | 1.0 | 1.0 | 1.0 | 0.89-1.16 | 1.0 |
| $\zeta$ | 12.16 | 12.16 | 12.16 | 12.16 | 12.16 |

$E_m$ = non-fibrillar matrix modulus, $E_f^0$ = initial fibril network modulus, $E_f^\varepsilon$ = strain-dependent fibril network modulus, $\nu_m$ = Poisson's ratio of the non-fibrillar matrix, $\eta$ = damping coefficient, $k_0$ = initial permeability, $M$ = material constant for void ratio dependent permeability, $n_f$ = fluid fraction, $h_z$ = normalized depth, $\rho_{c,tot}$ = the depth-dependent total collagen fraction (depth-dependent as a function of $h_z$) and $\zeta$ = density ratio of primary fibrils to secondary fibrils.
**REFERENCES:** [1] [2, 105, 193, 203, 208]; [2] [35, 202, 203, 228]; [3] [72, 203, 238–240]

## 6.3 CARTILAGE STRUCTURE IN THE MODELS

The collagen fibril architecture and FCD distribution, obtained from MRI, were implemented into the patient- and subject-specific model geometries in studies **I-II** and **III-IV**, respectively. In addition models with alternative collagen fibril network structures (studies **I** and **II**) and FCD distributions were created in order to assess the effect of the subject-specific variation in the cartilage structure on knee joint mechanics.

### 6.3.1 Implementation of collagen fibril orientations and FCD into the joint models

Implementation of the subject-specific collagen fibril orientations and FCD into the model geometries were done in a similar fashion in all the studies using custom-made Matlab scripts.

In studies **I** and **II**, the patient-specific collagen architecture was implemented into the model geometry. First, the superficial, middle and deep laminar boundaries of tibial cartilages were determined from $T_2$ mapped MR images. This was conducted as discussed above for each MR image used to obtain the model geometry according to the apparent collagen fibril orientations. The manually segmented tibial geometries were then manually coregistered with the corresponding location in the final model geometry (Fig. 6.4a). Each nodal point in the model was then assigned to one of the cartilage laminae, *i.e.* the lamina that the closest pixel was assigned to in the corresponding MR image (Fig. 6.4b). In study **II**, the laminae in each slice location was further assigned to the nodal points over the slice thickness in 3-D (all the way to the next slice, (Fig. 6.4b). The nodal points were finally assigned with split-line orientations and primary fibril orientations with respect to the cartilage surface according to the lamina, *i.e.* parallel, random (study **I**) or 45 degrees (study **II**) and perpendicular in the superficial, middle and deep layers of the cartilage, respectively (Fig. 6.4c).

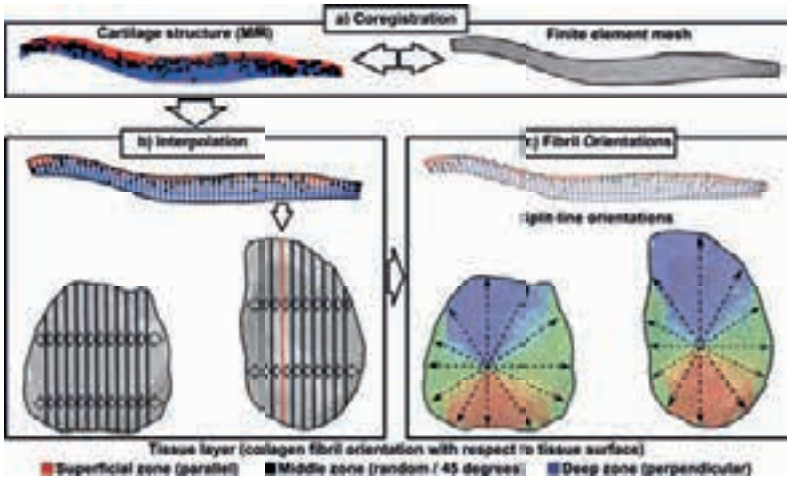


*Figure 6.4: A schematic presentation of the implementation of collagen fibril architecture from MRI into the FE-model. a) Coregisteration of MRI and model geometries mesh. b) Interpolation of the cartilage structure to the model geometry. c) Implementation of collagen fibril orientations into the model.*

In studies **III** and **IV**, the subject-specific FCD of tibial cartilage was implemented into the *subject-specific model* from sodium MRI. First, the segmented sodium MRI and the model geometry (both in 3-D) were coregistered using a custom-made iterative closest point method (ICP). The ICP method iteratively minimizes the difference between the locations of the segmented MR-image coordinates and the coordinates in the model geometry. Second, after the coregistration, the calculated FCD values were interpolated into the model coordinates from the sodium MRI using linear interpolation in 3-D.

### 6.3.2 Subject-specific and alternative models

The collagen architectures and FCD distributions in the different models are presented in Table 6.2.

**Study I (*Models I - V*):**
The patient-specific collagen architecture was implemented in the tibial cartilage as described above (*model I* (patient-specific model), Fig. 6.5b, Table 6.2). In order to evaluate potential uncertainties due to inaccurate estimation of the collagen architecture from MRI, particularly in the estimation of the superficial zone thickness, models *II* and *III* were created with alternative collagen architectures. In *model II*, the thickness of the superficial zone was increased with two pixels (*i.e.* 0.643 mm) as compared to *model I* and in *model III*, the superficial zone was replaced with randomly oriented collagen fibrils, representing the absence of the superficial zone, *e.g.*, due to fibrillation such as occurring in OA (Fig. 6.5b, Table 6.2). In addition, two models (*models IV* and *V*) were created with generic, constant depth-dependent collagen architectures (constant zone thicknesses) as obtained from the previous studies (Fig. 6.5b, Table 6.2) [48,241]. In *models IV* and *V*, the collagen fibril orientations in the laminae were assigned in the model geometry according to the relative tissue thickness at the model nodal location.

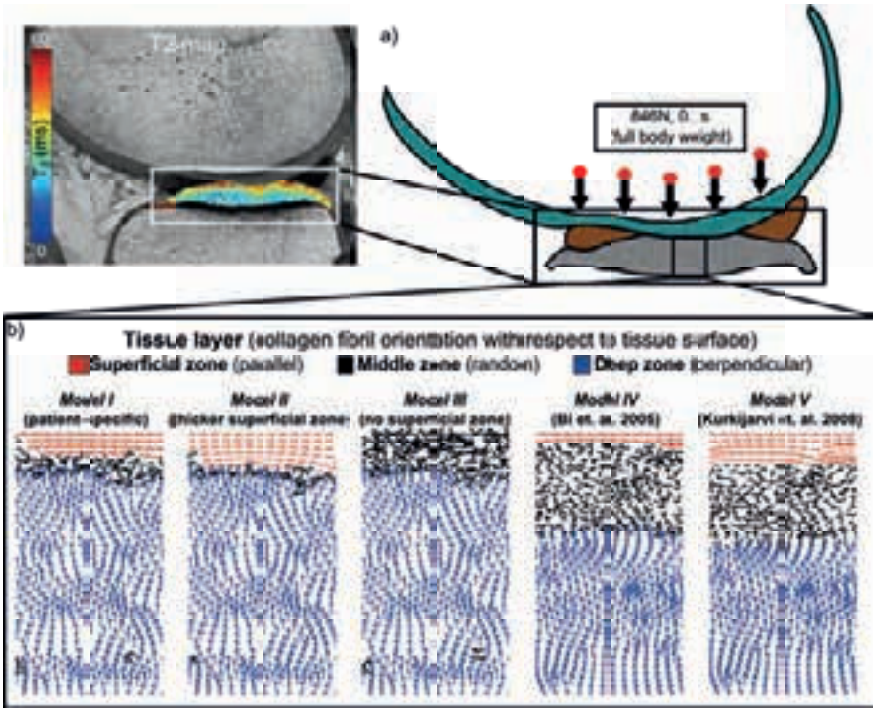


*Figure 6.5: a) The model geometry and load applied to the femoral cartilage-bone interface. b) The different collagen architectures in models I - V at the middle of the tibiofemoral contact in tibial cartilage (a)).*

**Study II (*patient-specific and literature global and submodels*):**
The collagen architecture, obtained from MRI, was implemented into the tibial cartilage of the *patient-specific global model* (Fig. 6.6b, Table 6.2). For comparison, a global model with constant depth-dependent fibril orientations in the tibial cartilage was created (*literature global model*, Fig. 6.6c, Table 6.2) [220]. Furthermore, a *patient-specific submodel* was created on an area in the medial tibial cartilage that described the weight bearing region during the maximum peak loads of the gait cycle in the global models (Fig. 6.6a). Submodeling was used in order to create a more detailed FE mesh to achieve a more precise material implementation and more accurate examination of a region of interest in the joint. Submodeling also

simultaneously decreased the total calculation times of the models in comparison to a whole joint model with a very fine FE mesh.

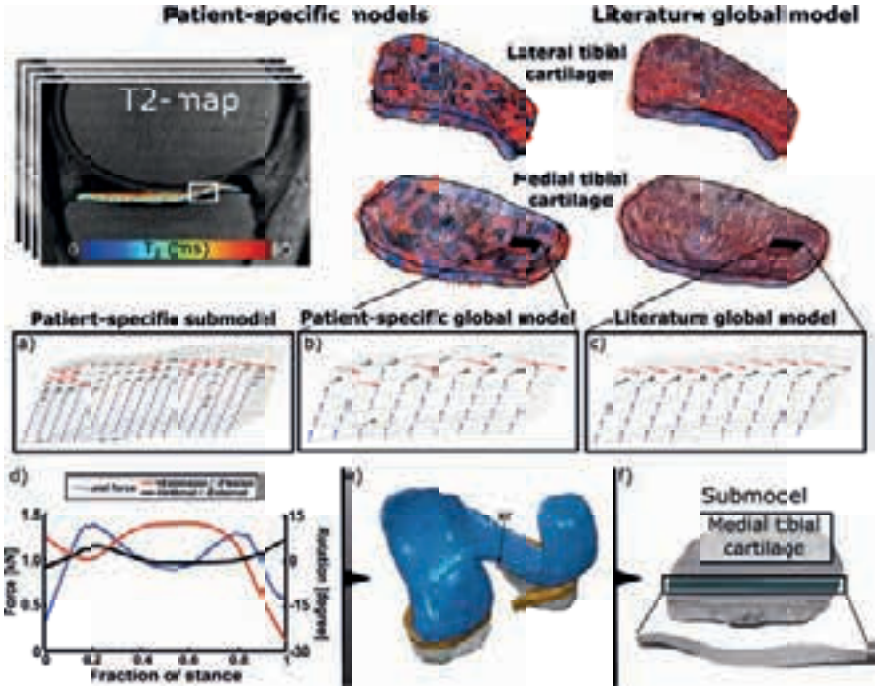


*Figure 6.6: Collagen architectures in the a) patient-specific submodel and b) global model, as well as in the c) literature model at the location of tibial cartilage, as indicated in the upper row in the MR slice, and full tibial geometries. d) The axial force and the extension-flexion and internal-external rotations used for the simulation of gait in the e) global joint model and translated into the f) submodel.*

**Study III (*subject-specific, literature and homogeneous global and compartment models*):** The FCD content of the tibial cartilage, determined from $^{23}$Na-MRI, was implemented into the tibial cartilage of the *subject-specific joint model* (Fig. 6.7a, Table 6.2). For comparison, two models with alternative FCD distributions in the tibial cartilage were created; a model with a homogeneous FCD distribution (*homogeneous model*, Fig. 6.7a, Table 6.2) and a model with a depth-dependent FCD distribution according to the depth-wise

variation in the FCD (*literature model* [53], Fig. 6.7a, Table 6.2). In both of these models, the mean FCD of the tissue was equal to the mean value in the *subject-specific model*. The *homogeneous* and *literature models* were created in order to demonstrate the importance of the subject-specific spatial variation of FCD in articular cartilage on the stresses and strains to which the medial and lateral tibial cartilages are subjected during standing.

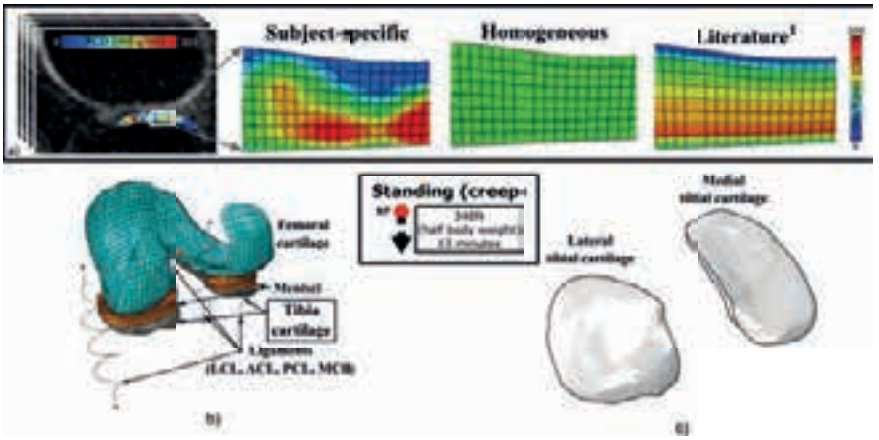


*Figure 6.7: a) FCD distribution in one location of the tibial cartilage in the models (indicated with a white box in the MR-image). b) The whole knee joint model geometry and the load applied to the reference point (RP), from which the model output is translated to the c) compartment models.*

**Study IV (*Healthy, EarlyOA, AdvancedOA and NoFCD models*):** The subject-specific global model from study *III* was used, and named here as the *Healthy model* (Figs. 6.7a,6.8a, Table 6.2). In addition, two models with alternative FCD distributions were created. The models were implemented with decreased FCD in a depth-wise manner, first, by (avg. over tissue depth) 17% (*EarlyOA model*) and, second, by 47% (*AdvancedOA model*) corresponding to the decrease in FCD in early and advanced stages of OA, respectively [228] (Fig. 6.8a,b, Table 6.2). The fibril network moduli ($E_f^0$ & $E_f^\varepsilon$, Table 6.1) were further decreased to 50% and 20% from that in the *healthy*, *Ear-*

*lyOA* and *AdvancedOA* models. Finally, a model without swelling (*NoFCD* model, FCD = 0 mEq/ml) was created with 20% of the fibril network moduli value. The models with reduced FCD and fibril network stiffnesses were created in order to investigate how the variation of FCD and tissue swelling would affect the model results and, in particular, the stresses and strains in the fibril network.

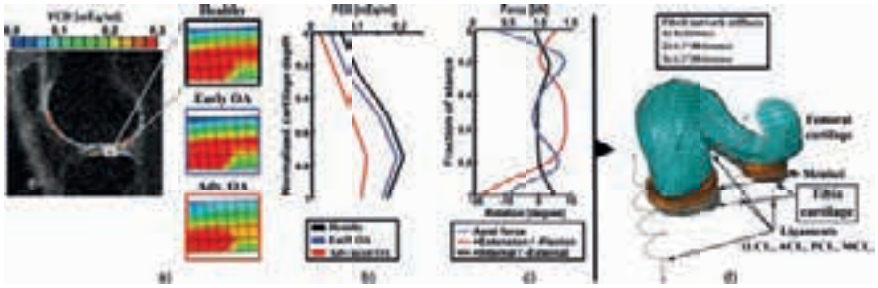


*Figure 6.8: a) FCD distributions in one location of the tibial cartilage in the models (indicated with a white box in the MR-image). b) The depth-wise mean FCD values at the tibiofemoral contact region of tibial cartilage in the models. c) The loading applied to the reference point d) in the whole joint model.*

The tibial cartilage tissues in all the models in studies **III** and **IV** were implemented with three-laminar primary fibril architectures (superficial, middle and deep zones) with constant zone thicknesses (mean thickness calculated in study *II* throughout the tibial cartilage) (Table 6.2).

*Table 6.2: Collagen fibril architectures ("Layer thickness") and FCD in the global/whole joint models.*

| Model | Layer thickness (%) Superficial | Middle | FCD (mEq/ml) | % of $E_0$ & $E_\varepsilon$ (Table 6.1) | Method (bold parameter) |
|---|---|---|---|---|---|
| **Study I (impact)** | | | - | | |
| *I (Patient-specific)* | **11 ± 6** | **18 ± 12** | - | 100 | MRI ($T_2$) |
| *II (Thicker SZ*)* | **19 ± 9** | **12 ± 11** | - | 100 | Modified MRI |
| *III (No SZ*)* | **-** | **29 ± 14** | - | 100 | Modified MRI |
| *IV (Literature)* | **5** | **33** | - | 100 | PLM [46] |
| *V (Literature)* | **11** | **32** | - | 100 | PLM [48] |
| **Study II (gait)** | | | - | | |
| *Patient-specific* | **12 ± 3** | **32 ± 4** | - | 100 | MRI ($T_2$) |
| *Literature* | **11** | **17** | - | 100 | PLM[1] [220] |
| **Study III (standing)** | | | | | |
| *Subject-specific* | 12 | 32 | **0.18 ± 0.08** | 100 | $^{23}$Na-MRI |
| *Homogeneous* | 12 | 32 | **0.18** | 100 | Mean $^{23}$Na-MRI |
| *Literature* | 12 | 32 | **0.01 - 0.31** | 100 | DD[2] [228] |
| **Study IV (gait)** | | | | | |
| *Healthy* | 12 | 32 | **0.18 ± 0.08** | 100, 50 & 20 | $^{23}$Na-MRI (REF) |
| *EarlyOA* | 12 | 32 | **0.15 ± 0.07** | 100, 50 & 20 | 0.83×REF |
| *AdvancedOA* | 12 | 32 | **0.09 ± 0.04** | 100, 50 & 20 | 0.53×REF |
| *NoFCD* | 12 | 32 | **0** | 20 | - |

*SZ = Superficial zone/layer
[1]PLM = Polarized Light Microscopy
[2]DD = Digital Densitometry

## 6.4 BOUNDARY CONDITIONS AND SIMULATIONS

In all studies, the tibial cartilage-bone interface was fixed in all directions and the bones were assumed to be rigid.

### *Study I: Subject-specific collagen architecture during impact loading (2-D)*

In order to investigate the effect of the patient-specific depth-wise and local variations in collagen fibril orientations in a knee joint, an axial impact load of 846 N of 0.1 second duration was applied to the femoral cartilage-bone interface (Fig. 6.5a). The load is equivalent to the total body weight subjected to the subject's knee. The menisci were allowed to move freely in the anterior-posterior direction. The

resulting stress, strain and pore pressure distributions of *models II-V* were compared to those predicted from the model with the subject-specific collagen architecture (*model I*).

***Study II: 3-D subject-specific collagen architecture during gait***

The aim was to investigate the effect of the patient-specific spatial and local variations in the collagen fibril orientations in 3-D during gait (dynamic loading). The global patient-specific and literature-based models were implemented with the knee joint motion and axial force during the stance phase of the gait cycle (duration 0.55s, Fig. 6.6d) [28, 233, 234]. The axial force was adjusted to the patient weight at each time point of gait (0.4 – 1.8 times the body-weight) [28, 233]. Finally, the femoral translations and rotations with respect to tibia and the axial force were implemented into a reference point (RP) located at the rotation center of femur (*e.g.* the midpoint between the lateral and medial epicondyles of femur, Fig. 6.6e) by coupling the femoral cartilage-bone interface to the RP [28, 194]. The varus-valgus rotation of the femur was unrestricted during the simulations [28].

Submodel analyses were performed by interpolating the nodal displacements and pore pressures obtained throughout the stance from the outer surfaces of the submodel location in tibial cartilage of the *patient-specific global model* to the integration points in the outer surfaces of the submodel as time-dependent boundary conditions (Fig. 6.6f). A submodeling approach was used in order to: 1) examine more accurately certain specific location in the tibiofemoral contact region in the joint, 2) implement the collagen architecture of the cartilage more accurately to the region of interest (mesh density corresponds to the MRI resolution), and to 3) minimize the calculation time needed for the joint level analysis.

The resulted maximum principal stresses, maximum principal strains, fibril strains and pore pressures in the tibiofemoral contact regions in all models were analysed as a function of time. The results obtained from the *patient-specific global joint model* were compared to those obtained with the *literature global model* and the

*patient-specific submodel*.

### *Study III: 3-D subject-specific fixed charge density distribution during standing (creep)*

In order to investigate the effect of the local, subject-specific, variation of FCD values in tibial cartilage, the models were subjected to a load which simulated standing (Fig. 6.7b). In addition, the model deformation was compared (validated) to that observed *in vivo* while the MR imaging was conducted in the presence of the 120 N load. In both simulations, the internal-external/extension-flexion rotations and medial-lateral/anterior-posterior translations of femur were fixed with respect to tibia and free varus-valgus rotation of the femoral cartilage was allowed [194,198,222]. The boundary conditions in the compartment models remained identical to those in the corresponding global joint models (apart from varus-valgus rotation and applied axial force). In all of the models, the cartilages were allowed to swell for 30000 seconds (free-swelling to equilibrium) prior to the application of loads.

***Model validation***:
In order to validate the deformation of the subject-specific joint model, the model was simulated using 120 N axial load for 13 minutes, the duration of the MRI experiment. The deformations in the tibial cartilage in the same subject were measured at the tibiofemoral contact regions of the medial and lateral tibial cartilages from the subject-specific model and the experimental MRI data.

***Simulation of Standing***:
First, the subject-specific, homogeneous and literature models of the whole joint were subjected to 348 N axial force (half body weight), for 13 minutes. The force was applied to the reference point located in the center of the femoral epicondyle, thereby simulating standing of the subject on two feet (Fig. 6.7b). Second, the varus-valgus rotation and the total axial reaction forces subjected to the medial

and lateral tibial cartilage compartments were collected from the whole knee joint model outputs as a function of time. Finally, the collected rotations and reduced axial forces were implemented as an input into the reference point in the medial and lateral compartment models (same location as in the global model, Figs. 6.1c,6.7c) [222, 235, 242]. These methods take into account the effect of ligaments in restricting the motion of the femur with respect to tibia in the compartment models [222].

The depth-wise maximum principal stresses, maximum principal strains, fibril strains and pore pressures in tibial cartilage of the subject-specific compartment models were compared to those of the homogeneous and literature models. All the results were calculated at the tibiofemoral contact region of the tibial cartilage.

***Study IV: Fixed charge density distribution during gait***

The aim of the study was to investigate the effect of FCD and tissue swelling on collagen fibril strains in tibial cartilage during dynamic loading. This was done by varying the FCD and fibril network moduli in the models and simulating them during gait cycle loading (6.8c). The gait data [28, 233, 234], the boundary conditions and the implementation of the gait into the models were conducted in the same way as in the global models in study **II**, apart from the free swelling (30000 s) of the tissues before the gait simulation. The resulting stress, strain and pore pressures were calculated from the tibiofemoral contact regions throughout the stance.

# 7 Results

The most important results of studies **I-IV** are summarized in this chapter. The emphasis here is on maximum principal stresses and strains, as well as fibril strains and pore pressures, which all are possible indicators for the disruption of the collagen network. For details and the remainder of the results, see the original publications.

## 7.1 EFFECT OF SUBJECT-SPECIFIC COLLAGEN ARCHITECTURE

### *Subject specific variation of collagen fibril orientations in articular cartilage*

The average superficial and middle zone/layer thicknesses of tibial cartilage were determined from $T_2$ profiles of a slice located in the lateral tibiofemoral contact region (study **I**), and slices of the whole cartilage (study **II**). The layer thicknesses obtained in study **I** were (mean $\pm$ SD through 137 depth-wise $T_2$ profiles): 11.1 $\pm$ 6.0% and 17.7 $\pm$ 12.0% (Fig. 7.1a, Table 6.2), and in study **II** (mean $\pm$ SD from 20 MR slices): 12.4 $\pm$ 3.4% and 31.5 $\pm$ 4.4% of the total tissue thickness, respectively (Table 6.2). In both cases, the superficial and middle zone thicknesses increased while moving further from the weight bearing area. The average thicknesses of the superficial, middle and deep zones in the region of *patient-specific submodel* (study **II**, mean from a single slice), were 12.7%, 24.5% and 62.7%, respectively (Fig. 7.1b).

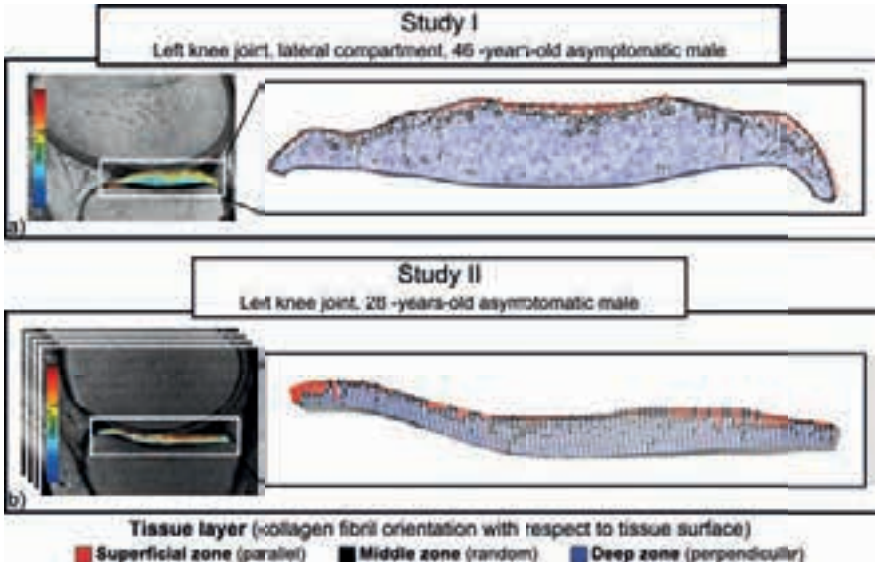


*Figure 7.1: a) The subject-specific collagen fibril orientations in the tibial cartilage determined using $T_2$ mapped MRI in study **I**. b) Subject-specific collagen fibril orientations at the location of the submodel in the tibial cartilage, determined from $T_2$ MRI **II**.*

### *Impact loading*

Compared to *model I* (patient-specific model, Fig. 7.2, 1st row), the increase in the superficial zone thickness in *model II* (Fig. 7.2, 2nd row) increased the maximum principal stresses and fibril strains in the superficial and middle layers of cartilage (up to +83% and +136%, respectively, Fig. 7.2a,b). Consequently, the maximum principal strains were reduced especially in the central parts of the tibia (up to -24%, Fig. 7.2c). Pore pressures were also decreased in tibial cartilage, particularly under the meniscus (up to -11%, Fig. 7.2d).

The removal of the tangentially oriented collagen fibrils in the superficial zone of tibial cartilage (*model III*, Fig. 7.2, 3rd row) decreased the maximum principal stresses and fibril strains (up to -69% in both parameters, Fig. 7.2a,b) in the superficial tissue in the tibial-femoral cartilage contact region. Maximum principal stresses and fibril strains were increased, particularly in the middle tissue

depths in the central regions of cartilage (up to +99% and +108%, respectively, Fig. 7.2a,b), while maximum principal strains were increased at the cartilage-cartilage contact region, especially in the superficial cartilage (up to +35%, Fig. 7.2c). Pore pressures were increased in the tibial cartilage, particularly under the meniscus (up to +13%, Fig. 7.2d).

Due to the thinner superficial layer thickness in *model IV* (Fig. 7.2, 4th row), maximum principal stresses and fibril strains were decreased in the superficial cartilage in comparison to the values obtained with *model I* (up to -37% and -42%, respectively, Fig. 7.2a,b) and consequently increased in the middle and deep layers of tibial cartilage at the central region of the model (up to +62% and +122%, respectively, Fig. 7.2a,b). However, the stresses and fibril strains were reduced below the meniscus (-46% in both parameters, Fig. 7.2a,b). The maximum principal strains and pore pressures were decreased in the superficial and middle layers (up to -14% and -15%, respectively), particularly under the meniscus (Fig. 7.2c,d).

The thicker superficial and middle layers in *model V* (Fig. 7.2, 5th row), compared to *model I*, increased maximum principal stresses and fibril strains at the tibiofemoral contact region throughout the tissue depth (up to +73% and +143%, respectively, Fig. 7.2a,b). However, those were decreased under the meniscus, especially in the middle layer of cartilage (up to -59% and -53%, respectively, Fig. 7.2a,b). Similarly, maximum principal strains were decreased particularly in the middle layers of cartilage (up to -26%) in the contact region (Fig. 7.2c). Pore pressures were also reduced under the menisci (up to -23% in the middle layers, Fig. 7.2d).

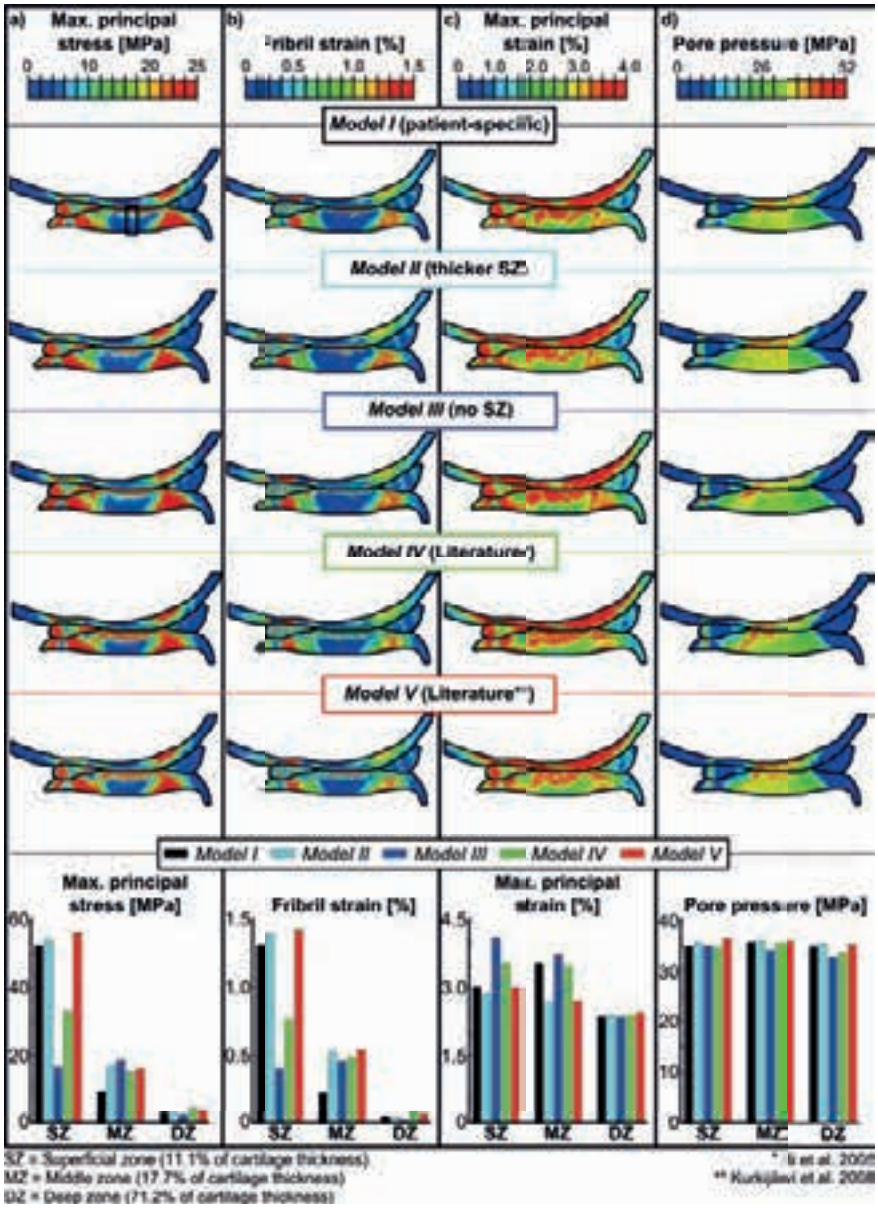


*Figure 7.2: The (a) maximum principal stress, (b) fibril strain, (c) maximum principal strain and (d) pore pressure distributions and the mean values at each tissue layer in models I to V, respectively, after the impact loading in study* ***I****. The values in the bar graphs (bottom row) are mean values from the layer depth in model I at the tibiofemoral contact region of tibial cartilage (indicated with the black box in a)).*

### *Gait loading*

All the results were collected from the tibiofemoral contact regions at each time point in the gait.

***Patient-specific global model vs. Literature global model***:
In lateral tibial cartilage, the implementation of patient-specific collagen architecture had the most notable effect on the fibril strains and maximum principal stresses during the terminal stance (at 80% of the stance) *i.e.* it reduced them in the middle tissue depths (up to -231% and -20%, respectively, Fig. 7.3a,c,e,f), as compared to the *literature model*. Similarly, in the medial tibial cartilage of the patient-specific model, the fibril strains and maximum principal stresses were clearly decreased, particularly in the superficial tissue depths of the medial tibial cartilage in the *patient-specific model* during the midstance (up to -413% and -26% at 43% of the stance, respectively, Fig. 7.3b,d).

Implementation of patient-specific collagen architecture into the model had a smaller impact on pore pressures and maximum principal strains, when compared to the *literature model*. In lateral tibial cartilage, the pore pressures declined while maximum principal strains increased in the superficial and middle regions during the terminal stance (up to -6% and +13% at 80% of stance, respectively). Similarly, pore pressures decreased and maximum principal strains increased in the superficial and middle regions in the medial tibial cartilage of the *patient-specific model* particularly during the midstance (up to -10% and +7% at 40% of the stance, respectively).

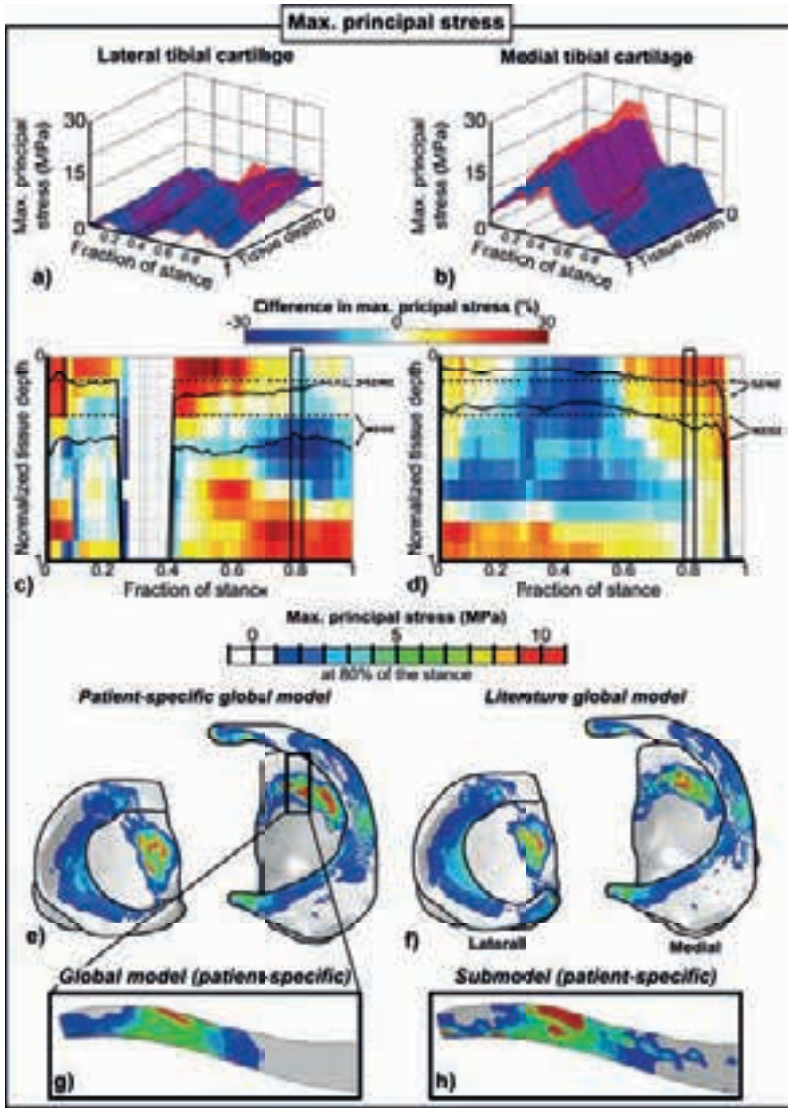


*Figure 7.3: Maximum principal stresses during the stance phase of gait with respect to the tissue depth in the tibiofemoral contact region in (a) lateral and (b) medial tibial cartilage in the patient-specific (blue) and in the literature global model (red). The relative differences in maximum principal stresses (patient-specific – literature) in (c) lateral and (d) medial tibia. The depth-wise superficial-middle zone (SZ/MZ) and the middle-deep zone (MZ/DZ) boundaries in the contact region at each time point of the stance in the patient-specific and literature global models are shown as solid and dashed lines, respectively. e) The distribution of maximum principal stress in the tibial cartilage and meniscus surfaces in the patient-specific and f) literature models. g) A sagittal close-up from the tibiofemoral contact region (indicated in e), at the location of the submodel) in the medial tibial cartilage in the global joint model and h) the corresponding location in the submodel.*

***Patient-specific submodel vs. Patient-specific global model***:
The more accurate implementation of the collagen fibril orientations into the submodel did not alter the stress and strain distributions between the *patient-specific global model* and the *patient-specific submodel* (Fig. 7.3g,h). However, when compared to the global model, the magnitudes of fibril strains and maximum principal stresses were increased, particularly in the superficial cartilage of the submodel throughout the entire duration of stance (up to +81% and +72% at 20% - 50% of the stance, respectively). Pore pressures were rather similar between the global and the submodel, although the pressure values were decreased in the submodel during the midstance at middle tissue depth (up to -23% at 50% of the stance). Maximum principal strains mostly decreased in the superficial and middle regions of the submodel, in particular during the midstance (up to -26% at 50% of stance).

## 7.2 EFFECT OF SUBJECT-SPECIFIC VARIATION OF FCD

### *Fixed charge density distribution*

The mean FCD in the tibial cartilage of the left knee of the volunteer was 0.18 $\pm$ 0.08 mEq/ml (mean $\pm$ SD from the segmented MR slices), as determined from sodium MRI (Fig. 7.4). The FCD increased along the tissue depth from the cartilage surface toward the deep cartilage and reached its maximum at about 80% of the total tissue depth (Fig. 7.4c), in both medial and lateral compartments.

In comparison with the homogeneous FCD distribution in the *homogeneous model*, the FCD determined from sodium MRI in the *subject-specific model* was smaller in the superficial tissue at the tibiofemoral contact region (more than -40% in the lateral compartment (Fig. 7.6a,c,e) and -11% in the medial compartment (Fig. 7.6a,d,f)), while it was mainly higher in the middle/deep tissue depths (up to +57% in the lateral compartment (Fig. 7.6c,e) and +51% in the medial compartment (Fig. 7.6d,f)). When compared to the generic distribution of FCD in the *literature model*, the FCD content in the *subject-specific model* was higher in the superficial tissue at the lat-

eral and medial tibiofemoral contact region (more than +7% and +27%, respectively, Fig. 7.6a,c-f), while it decreased (up to -47% in the middle tissue depth) in lateral compartment (Fig. 7.6c,e) and increased in the deep tissue in both lateral and medial tibial compartments (more than +20% and +8%, respectively, Fig. 7.6c-f).

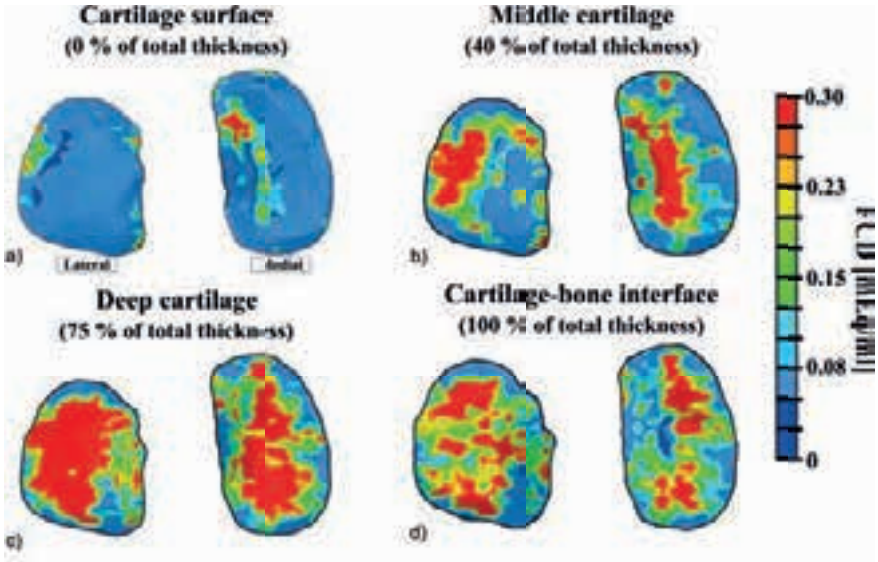


*Figure 7.4: a-c) FCD distributions at different tibial cartilage depths, as determined from the sodium MRI.*

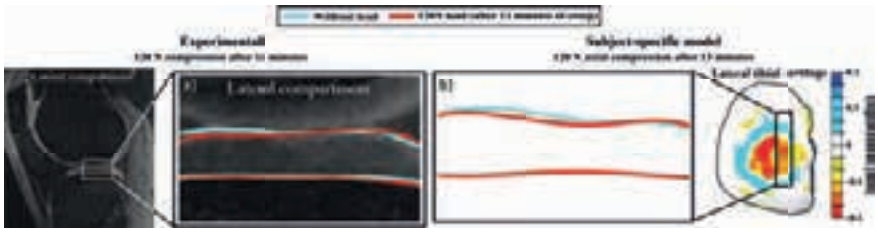


*Figure 7.5: An example from one location in the tibial cartilage of the experimentally determined deformation under a 120N load at 13 minutes. a) A close up of the tibiofemoral contact region from that particular slice. b) The deformation of the tibial cartilage observed in the subject-specific model, with a close up of the compressed (red) and uncompressed (blue) geometries from the same location as in a).*

### *Model validation*

When a 120 N compression (after 13 minutes) was applied in the experimental MRI set-up, the mean strains observed in the tibiofemoral contact regions of medial and lateral tibial plateaus were 4.8% and 1.6% of the uncompressed cartilage thickness, respectively (Fig. 7.5a). The mean strains observed in the corresponding tibiofemoral contact regions of the subject-specific model were 2.3% and 3.8% in the medial and lateral tibial compartments, respectively, after similar loading of 120 N for 13 minutes (Fig. 7.5b).

### *Standing*

Again, all the results were collected from the tibiofemoral contact regions at the beginning (dynamic response, $t \approx 0$ minutes) and at the end of the simulations (end of creep, $t \approx 13$ minutes).

***The Dynamic phase***:
In comparison to the *homogeneous model*, the smaller FCD values in the superficial tibial cartilage of the *subject-specific model* had no effect on the axial strains, maximum principal stresses and pore pressures between the models (Fig. 7.6c,d). Minor variations in fibril strains were observed, particularly in the superficial tissue (up to -3% in lateral tibial cartilage (Fig. 7.6c)).

When compared to the *literature model*, again the increase in FCD in the superficial tibial cartilage of the *subject-specific model* did not exert any notable effect on the differences in axial strains between the models (Fig. 7.6c,d). The same behavior was also observed in maximum principal stresses (up to $\pm$ 3% in both compartments) and in fibril strains (up to $\pm$ 5% in both compartments) between the models (Fig. 7.6c,d). Pore pressures were only slightly different between the models (Fig. 7.6c,d).

***The End of Creep***:
When compared to the *homogeneous model*, the axial strains in the superficial tissue were increased in the lateral and medial tibial car-

tilages (up to +9% and +13%, respectively, Fig. 7.6b,e,f) due to the lower FCD in the superficial cartilage in the *subject-specific model* (Fig. 7.6a). In the deep tibial cartilage in the *subject-specific model*, the maximum principal stresses were increased while the fibril strains were only slightly decreased in the superficial/middle tissue depths (up to +19% in the lateral tibial cartilage and up to -5% in both lateral and medial compartments, respectively, Fig. 7.6e,f). Pore pressures were increased, particularly in the superficial tissue in the lateral tibial cartilage (up to +3%, Fig. 7.6e), while the pressures were slightly decreased throughout the tissue depth in the medial tibial cartilage (up to -3%, Fig. 7.6f).

When compared to the *literature model*, the implementation of FCD from sodium MRI decreased the axial strain in the superficial tissue of the *subject-specific model* both in the lateral and medial cartilages (up to -18%, Fig. 7.6b,e,f) due to the increase in FCD. In the middle tibial cartilage, the axial strains were increased in the lateral tibial compartment (up to +4%, Fig. 7.6e). The maximum principal stresses and fibril strains were mostly decreased throughout the tissue depth in both tibial cartilage compartments (up to -8% and -5%, respectively, Fig. 7.6e,f). Pore pressures were again slightly decreased throughout the tissue depth in both tibial cartilage compartments (up to -5% in the superficial tissue depth in the medial tibial cartilage, Fig. 7.6f).

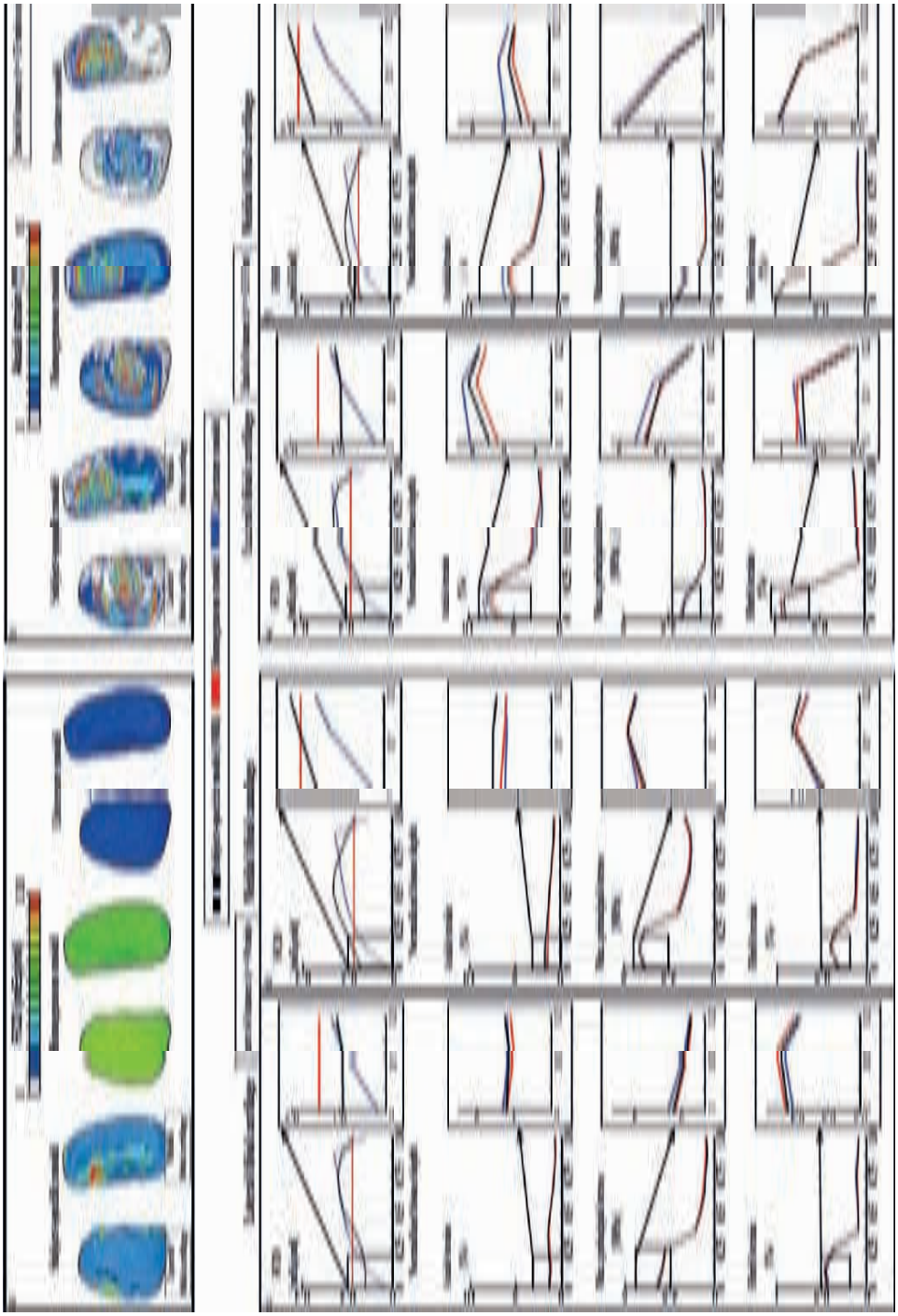

*Figure 7.6: The a) FCD and b) axial strain distributions at the surface of the tibial cartilage in the models after 13 minutes of standing. The depth-wise variation of the stresses and strains in the tibiofemoral contact region of c,e) lateral and d,f) medial tibial cartilages at the beginning of the simulation (application of load) and at the end of standing (13 minutes), respectively.*

### *Effect of FCD and fibril network stiffness during gait*

Fibril strains and axial strains were analyzed between the models with normal (healthy) and decreased FCD values and collagen fibril network stiffness in the tibial cartilage. The differences in fibril strains and axial strains, as compared to the *healthy models* (with varying fibril network stiffness from the reference ("Ref", Table 6.2)), remained rather similar throughout the entire stance. However, the differences were most notable during the first peak load of gait (approx 20% of the stance phase):

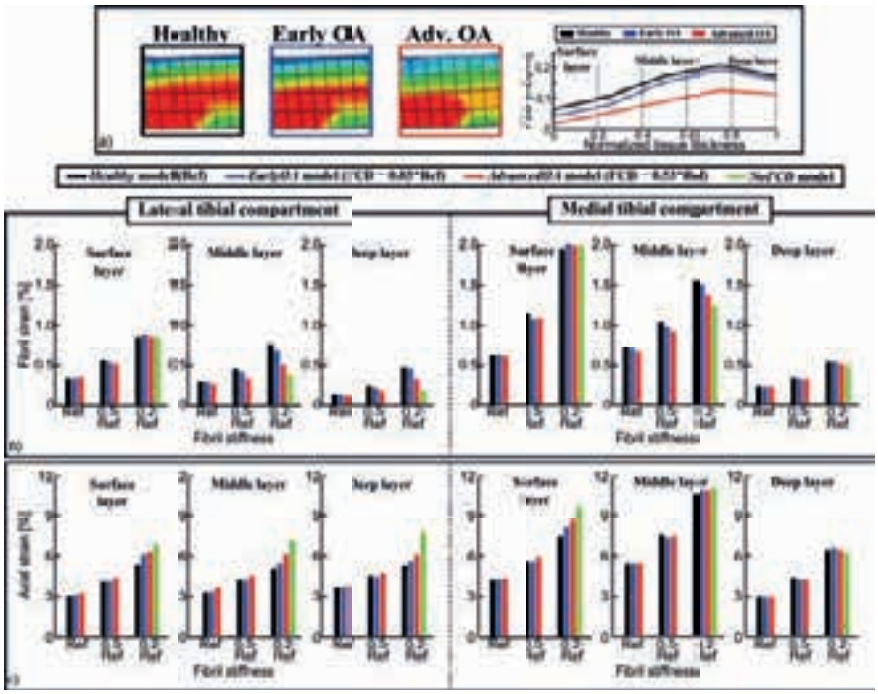


*Figure 7.7: a) Variation (an example from the tibial cartilage) and the depth-wise distributions of FCD the tibiofemoral contact region in the models. The mean b) fibril strains and c) axial strains in the superficial, middle and deep layers (indicated in a)) of lateral and medial tibial cartilages with different fibril network stiffnesses.*

***Fibril network stiffness = Reference***:
Compared to the *Healthy model*, the 17% decrease in FCD in *EarlyOA model* (Fig. 7.7a) decreased fibril strains (avg. throughout the tissue thickness in the tibiofemoral contact region of tibial cartilage) only by -2% and -1% (Fig. 7.7b) and increased axial strains only by +2% and +1% in lateral and medial compartments, respectively (Fig. 7.7c). Similarly, the 47% decrease in FCD in the *AdvancedOA model* (Fig. 7.7a) decreased fibril strains by -8% and -3% (Fig. 7.7b), and increased axial strains by +9% and +1% in lateral and medial compartments, respectively (Fig. 7.7c).

***Fibril network stiffness = 0.5 $\times$ Reference***:
The decreased FCD in *EarlyOA model* (with 50% reduced fibril stiffness) decreased fibril strains by -6% and -4% in lateral and medial compartments, respectively (Fig. 7.7b) and increased axial strains by +1% in both compartments (Fig. 7.7c), when compared to the *Healthy model*. In the *AdvancedOA model*, the fibril strains were decreased by -20% and -6% (Fig. 7.7b), while axial strains were increased by +7% and +6% in the lateral and medial tibial compartments, respectively, as compared to the *Healthy model* (Fig. 7.7c).

***Fibril network stiffness = 0.2 $\times$ Reference***:
In comparison with the *Healthy model*, the lower FCD in *EarlyOA model* decreased fibril strains by -5% and -1% (Fig. 7.7b) and increased axial strains by +9% and +6% in lateral and medial compartments (Fig. 7.7c), respectively. Again, in the *AdvancedOA model*, fibril strains decreased by -23% and -6% (Fig. 7.7b), while axial strains increased by +19% and +7% in the lateral and medial tibial compartments (Fig. 7.7c), respectively, when compared to the *Healthy model*. When the FCD was neglected altogether, in *NoFCD model*, fibril strains decreased by -39% and -11% (Fig. 7.7b), and axial strains increased by +39% and +19% in lateral and medial compartments (Fig. 7.7c), respectively, when compared to the *Healthy model*.

# 8 Discussion

This chapter elaborates on the meaning and evaluates the significance of the methods used in the studies and the results obtained.

## 8.1 MODEL VALIDITY

Direct validation of the model results (*e.g.*, validation of stresses, fibril strains, contact pressures etc.) is very challenging, if not impossible, with live test subjects. However, in all the studies, the modeling results were compared to earlier experimental and computational studies. In addition, study **I** investigated how the results and thus the conclusions vary between subjects. In addition, the tissue strain was compared to experimental results in study **III** [195].

In study **I**, the validity of conclusions was tested by modeling another subject obtained from the OA Initiative (67-year-old male, weight 88.5kg, Kellgren-Lawrence grade 0; no symptoms of joint diseases). The MR-imaging and the protocol for the creation and analysis of *models I-V* were consistent with those used in the original model. As expected, due to differences in the geometry and load, the absolute values between the models from individual subjects differed. However, the distributions of stresses, strains and pore pressures were similar in all models (data not shown) and the conclusions were the same. Most importantly, this suggests that the study results and conclusions are independent on the input geometry. In addition, fluid carried approximately 90% of the total load at the contact area between tibial and femoral cartilages in *model I*, which is in line with the values presented previously in the literature [243, 244]. Furthermore, the observed maximum principal stress and strain distributions as well as fibril strains and pore pressures in different tissue layers and locations of cartilage corresponded well with those reported in previous studies (Fig. 7.2) [105, 193, 205].

In study **II** on average 44% of the total load was transferred

through the lateral compartment and 56% through the medial compartment in the *patient-specific model* during the gait. In addition, the lateral meniscus absorbed on average 80% of the load subjected to the lateral tibial compartment, therefore, reducing the tibiofemoral contact stresses, particularly during the beginning of the midstance (Fig. 7.3a). On the medial side, on average, the meniscus absorbed 57% of the load to which the medial compartment was subjected, causing higher stresses on the tibial cartilage (Fig. 7.3b). This behavior, along with the distribution of loads during the stance in different locations, correspond well with the previously-reported results [28, 191, 205, 245, 246]. The average contact pressures observed throughout the stance in the lateral and medial tibiofemoral contact regions ($3.7 \pm 0.7$ MPa and $5.5 \pm 2.3$ MPa) are also consistent with earlier experimental results [247, 248].

Finally, in study **III** the deformation of the tibial cartilage in *subject-specific model* was compared to experimental values, *i.e. in vivo* loading of the joint conducted with a MR-compatible compression device [229]. The deformation of tibial cartilage attributable to the 120 N axial load in the presented model corresponded well with the experimentally measured deformations in the knee joint cartilage *in vivo* (Fig. 7.5). However, the free varus-valgus rotation of the femoral cartilage in the model resulted in only a slightly smaller deformation in the lateral and a slightly larger deformation in medial tibial cartilages in the subject-specific model, when compared to the experimental observations. The varus-valgus was set free in the model in order to maintain stable and constant contact between the femoral and tibial cartilages through the simulation. In addition, the varus-valgus orientation of the femur with respect to tibia and the tibiofemoral contact regions were similar in the model after the simulation as was observed in the experimental MR images after the compression. It is also worth noting that the mean deformations of the lateral and medial tibial cartilages observed in the experimental *in vivo* MRI study (less than 5% of the total tibial cartilage thickness) are smaller than the in-plane pixel size in the scan. However, the reported mean deformations were calculated

from the tibiofemoral contact regions from approximately 10 slices for both compartments and therefore can be considered valid.

## 8.2 IMPORTANCE OF SUBJECT-SPECIFIC CARTILAGE COMPOSITION

### 8.2.1 Collagen architecture

In studies **I** and **II**, computational FE-modeling methods were developed and applied to evaluate the importance of the patient-specific collagen architecture of the tibial plateau cartilage on knee joint mechanics under impact loading in 2-D and during the stance phase of gait in 3-D, respectively.

*Collagen fibril architecture from $T_2$ mapped MRI*

The variation of the collagen fibril orientations in the tibial cartilage of an intact human knee joint was determined from clinical $T_2$ mapped MRI and presented for the first time in 2-D and 3-D. The patient-specific layered structures of tibial cartilages that were determined and presented in studies **I** and **II** (superficial and middle zone thicknesses: 11.1 $\pm$ 6.0% and 17.7 $\pm$ 12.0% (Fig. 7.1a), 12.4 $\pm$ 3.4% and 31.5 $\pm$ 4.4% (Figs. 7.1b, 6.6a), respectively) are consistent with those determined previously for human articular cartilage using MRI and polarized light microscopy (superficial and middle zone thicknesses 5.2 $\pm$ 2.2% - 11.0 $\pm$ 8.2% and 18.0 $\pm$ 7.0% – 32.0 $\pm$ 13.1%, respectively) [21,48,249]. Furthermore, as observed in studies **I** and **II**, the patient-specific collagen architecture and layer thicknesses vary within the cartilage tissue. In particular, the thicknesses of the superficial and middle zones increase in the anterior/posterior and medial/lateral directions from the central weight bearing regions of tibial cartilage. This corresponds well with previous findings [41].

In study **II**, the tibiofemoral contact area in tibial cartilage varied during the stance phase of gait (Fig. 7.3c,d). Therefore, the zonal thicknesses vary from one time point to the next according to the

variation in the contact region. This highlights the importance of including the subject-specific spatial variation in the collagen architecture and the fibril orientations when evaluating the mechanical response of knee joint cartilage.

The same method to delineate the zonal boundaries was used in both studies **I** and **II**. The method is only dependent on each of the depth-wise $T_2$ profiles at a time and, therefore, is independent of the differences in the imaging sequences used in the studies.

### *Impact on cartilage mechanics during dynamic loading*

In both studies **I** and **II**, the patient-specific collagen architecture modulated the observed stresses and strains in tibial cartilage. Specifically, the observed alterations in the stress, strain and fluid pressure patterns between the *patient-specific models* and the models with alternative collagen architectures are related to the differences in spatial and local zone thicknesses (Figs. 6.5b,7.2).

Collagen fibrils resist effectively tension in the direction of the fibril. Therefore, in the FRPVE material, the highest tensile stiffness (measured parallel to the cartilage surface) is highest in the superficial tissue where the collagen fibrils lie parallel to the cartilage surface and lowest in the deep zone where the collagen fibrils are perpendicular to the cartilage surface [61, 64]. Therefore, *e.g.*, the increase in the superficial zone thickness results in stiffer cartilage in the tensile direction at the extended zonal depths.

As observed in study **I**, the increase in superficial layer thickness in *model II* increased the tensile stiffness simultaneously increasing the fibril strains compared to the model with patient-specific collagen architecture (*model I*, Fig. 7.2b). This also reduced the maximum principal strains and increased stresses in *model II*, particularly at the intermediate tissue depths, and reduced pore pressures under the meniscus (Fig. 7.2b-d)). Similarly, the removal of the tangentially oriented collagen fibrils from the superficial tissue in *model III* impaired the capability of the cartilage to resist tensile forces and resulted in significantly increased maximum principal strains and reduced maximum principal stresses in the superfi-

cial cartilage (Fig. 7.2c,d) [105]. Consequently, maximum principal stresses increased in the deeper parts of cartilage, while due to the increased tissue strain, the pressurization of the fluid was increased under the meniscus (Fig. 7.2c-e). On the other hand, as the middle zone extended in the direction of the deep zone, the perpendicularly oriented collagen fibrils were replaced with randomly oriented collagen fibrils at those tissue depths. This also increased the tensile stiffness of the tissue. Therefore, when compared to *model I*, the thicker middle zone in *models IV* and *V* increased the overall stiffness of the cartilage and led to increased fibril strains and the principal stresses in the middle tissue depths, particularly below the tibiofemoral contact region (Fig. 7.2b,c). Consequently, this also reduced the principal strains (Fig. 7.2d).

In study **II**, as compared to the *literature model*, the superficial and middle zone thicknesses were larger in the lateral and smaller in the medial tibial cartilages in the *patient-specific model*. Similarly to study **I**, this increased the tensile stiffness in the lateral tibial cartilage and led to larger fibril strains and maximum principal stresses at those tissue depths in the *patient-specific model* (Fig. 7.3a,c,e). The reduced thickness of the superficial and middle zones are responsible for an opposite behaviour in the medial tibial cartilage, *i.e.*, a decrease in the fibril strains and principal stresses, particularly in the middle cartilage depths (Fig. 7.3b,d,f). The differences between the two models in pore pressure were consistent with the stress distributions, while maximum principal strain exhibited an inverse behavior. The behavior of stresses and strains was highly dependent on the phase of stance and the alternating tibiofemoral contact due to the local and depth-wise variations in the collagen fibril orientations between the models.

These results show that the use of non-specific collagen architecture is able to alter the modeled tissue response to dynamic loading of the joint. As demonstrated in the present studies, patient-specific evaluation of stresses and strains in normal and diseased cartilage in the knee joint may be inaccurate if the patient-specific collagen fibril network architecture is not available.

*Precision of fibril implementation (submodeling)*

A submodel was created in study **II** in order to investigate a specific region of interest with a fine FE mesh. This approach enables a more precise implementation of the fibril orientations into the region of interest, and led to more accurate representation of the material properties in the location of the submodel (Fig. 6.6a,b). The results with the submodel (*i.e.* in comparison to those obtained from the global joint model) suggest that the use of a finer element mesh influences the model results, particularly when examining fibril strains and maximum principal stresses (Fig. 7.3g,h). However, the use of a finer mesh might not be needed, *e.g.*, for modelling fluid flow or maximum principal strains in the tissue. Most importantly, the submodel can be created for any location in the global model and hence enables the evaluation of a local region of interest, *e.g.*, a specific location with a visible cartilage rupture in the MR images. Submodeling also enables the use of larger element size in the global model, which decreases the total calculation time of the joint models, especially in the 3-D models with large amount of elements and complex loading schemes.

### 8.2.2 Fixed charge density

In studies **III** and **IV**, FE-modeling was used with FRPVES material, that is capable of taking into account the swelling of cartilage tissue due to the negative charge (FCD) [55,202]. Hence, the subject-specific variation of FCD was determined from sodium MRI and its importance on knee joint function was evaluated under static and dynamic loading, simulating standing and gait.

*FCD from Sodium MRI*

Quantification of both sodium concentration and FCD from sodium MRI depend on the post processing steps and corrections applied to the measured signal intensity [24, 25, 144, 145, 147, 250]. In the present studies, the corrections for the inhomogeneous $B_1$ magnetic field, partial volume effects, biexponential $T_2^*$ and monoexponential

$T_1$ relaxations to the observed signal intensity were necessary for the calculation of the sodium concentrations and most importantly, the FCD of the cartilage tissue even at high field strengths (7 T) and with images of fair resolution (in-plane 1.5 x 1.5 mm, slice thickness 2.8 mm, Fig. 6.3). The sodium concentration of tibial cartilage, calculated for the tibial cartilage in study **III**, and used in study **IV**, (260 $\pm$ 70 mM) is in agreement with previously reported values (mean values 240 mM – 270 mM) [24, 25]. In addition, the calculated mean FCD and the depth-wise variation of the FCD (Fig. 7.4) correspond well with those presented in previous studies (FCD: 0.1 – 0.3 mEq/ml) [53, 54, 228].

***Impact on cartilage mechanics during creep***

As observed in study **III**, the subject-specific variation of FCD in the tibial cartilage had no substantial effect on the stresses and strains during the beginning of the simulated standing (*subject-specific model* vs. the *homogeneous* and *literature models*) (Fig. 7.6c,d). This observation was expected, as the cartilage response to dynamic loading is mainly determined by the interplay between the fluid and the collagen fibrils [1–3]. Furthermore, the negligible differences observed mostly in the maximum principal stresses and fibril strains between the models are due to the similar mean FCD of cartilage, resulting in rather similar, bulk cartilage stiffness in the models. Nevertheless, the increase in FCD also increases the tissue swelling, and leads to slightly increased fibril strains within the tissue (Fig. 7.6c,d) [1]. This was observed also in the current models in the unloaded joints, immediately after the free swelling period of the tissues (the 30000 second simulation without loading, during which the cartilage swelling reaches equilibrium). Therefore, alterations in the FCD content and tissue swelling, *e.g.*, due to OA, would alter the pre-strain in the collagen network, tissue stiffness and thus can exert an effect on the tissue response also to dynamic loading, *e.g.*, during walking (as discussed above).

After 13 minutes of standing (creep), the implementation of the subject-specific FCD from sodium MRI into the *subject-specific joint*

*model* displayed a notable effect on axial strains, when compared to the models with the homogeneous FCD distribution and to the model with the FCD obtained from the literature (Fig. 7.6a,b,e,f). When compared to the *homogeneous model*, the locally smaller FCD content in the superficial cartilage in the *subject-specific model* decreased the local tissue stiffness and increased the tissue strains and also the local fibril strains (Fig. 7.6e,f). The higher amount of FCD in the deeper tissue in the *subject-specific model* also increased the local tissue stiffness in the deep tissue, resulting in decreased strains (Fig. 7.6e,f). When compared to the *literature model*, the FCD in the tibiofemoral contact region was either higher or lower throughout the tissue depth in the *subject-specific model*. Consequently, this led to correspondingly altered strains at the corresponding tissue depths (Fig. 7.6e,f). These results suggest that, in particular, the axial strains follow the pattern of the FCD.

***Impact on cartilage mechanics during gait***

Previous, mostly modeling studies have proposed that variation of the nonfibrillar matrix stiffness of cartilage tissue plays no role on the knee joint response to dynamic loading [194]. However, the tissue swelling and the variation of the FCD has also been neglected in the previous knee joint models. The observations made during the free swelling period in study **III** proposed that the swelling due to FCD might influence the internal strain in the collagen network, and should have an effect on the tissue response to dynamic loading.

In study **IV**, the decrease in FCD content from that in *Healthy models* reduced fibril strains particularly during the first peak load of the stance phase of gait (at 20% of the stance, the loading response, Fig. 7.7a,b). This is due to the reduced swelling of the cartilage tissue which resulted in a smaller internal swelling pressure and, hence reduced the strain in the collagen network. Reduced FCD also decreased the stiffness of the cartilage tissue, thus resulting in larger deformations in the tibial cartilage in *EarlyOA*, *AdvancedOA* and *NoFCD* models (Fig. 7.7c).

The importance of FCD on the cartilage response was further emphasized when the fibril stiffness was decreased in the *EarlyOA* and *AdvancedOA models*, as compared to the *Healthy model* (Fig. 7.7b,c). This behavior was observed since the softer fibril network allows the tissue to swell more due to (constant) FCD, hence amplifying the effect of FCD and creating larger strains on the fibrils and increasing the difference between the healthy and OA models. This behaviour was most apparent when the FCD was reduced to zero (*NoFCD model*). In more specific terms, as the FCD is neglected, also the internal pressure of the tissue and the swelling are negligible (equations 4.13,4.14). This leads to notably softer tissue stiffness and hence to a larger deformation of the cartilage [204, 221]. However, it must be noted that this is a parametric study on the effect of FCD and the OA models did not include any other variations in the tissue composition other than decreased FCD. Thus, direct conclusions related to OA may be only drawn from the *EarlyOA models*.

This tissue behavior has been lacking in previous computational models and these have led to the earlier assumptions that the PG loss does not contribute to the cartilage response during gait [194]. The results in study **IV** demonstrate that FCD does exert a small effect, though smaller than that of the collagen fibrils, on the mechanical response of cartilage during dynamic loading of the knee. In particular, FCD and tissue swelling play an increasingly important role on joint mechanics when the fibril stiffness decreases, *e.g.*, due to degradation of the fibril network during the progression of OA.

## 8.3 LIMITATIONS

Modeling studies are rarely without limitations and studies **I - IV** included in this thesis are no exceptions in this respect.

First, in the methodologies, the MR imaging imposes certain limitations. The main limitation of MRI is the relatively large imaging resolution and voxel size, which results in a certain amount

of information loss, *e.g.*, due to the partial volume effect (PVE) [16, 106, 251, 252]. The resolution of MRI can pose a problem in the inter-scan repeatability, and in particular in the determination of the thin superficial zone from the $T_2$ profiles [253]. The MR data used in this thesis consisted of MR-images with in-plane resolutions of 0.3 - 1.5 mm. Therefore, in studies **I** and **II**, one pixel in the image was equivalent to a size corresponding to approximately 5-10 % of the tibial cartilage thickness, which is also close to the superficial layer thickness of articular cartilage. With this level of precision, it is possible that one may not detect small changes and variations, especially in the superficial tissue. In thin cartilage, the superficial collagen fibril layer may thus remain invisible, *e.g.*, due to the partial-volume effect [16]. The same phenomenon is most apparent also in the case of sodium MRI (in-plane resolution 1.5mm and slice thickness 2.8mm), where the SNR and signal intensities are notably affected by the low resolution (PVE, [147]) and, *e.g.*, by inhomogeneities in the magnetic field [250]. However, the signal loss in sodium MRI can be countered by carefully choosing the appropriate methods to correct the apparent signal intensities, as was done in study **III**.

The imaging plane and joint geometry can also cause inaccuracies in the estimation of collagen architecture [16]. Specifically, the $T_2$ relaxation times reach their maximum value when the imaged object or structure is at the *magic angle* with respect to the static magnetic field [133]. Therefore, variations in the positioning of the knee in the MR scanner can affect the signal intensities observed in the joint ROI and may alter the laminar appearance of the cartilage in the final MR image. In addition, the curvature of the cartilage surface may modify the observed signal intensity and can increase uncertainties in the architectural evaluation, especially in those regions where the direction of the cartilage surface is not perpendicular to the main magnetic field [16]. The curvature of the cartilage surface in the anterior-posterior and medial-lateral edges of the cartilage can result in a more uniform depth-wise $T_2$ profile (due to the *magic angle* effect) [16, 254]. This behavior makes the

delineation of the zonal boundaries cumbersome and may exaggerate the thickness of the middle zone in those regions with a curved cartilage surface. However, in the MR images used in the current studies, the joints were perpendicular to the external magnetic field, and hence the delineation of the collagen architecture should be rather precise, particularly in the relatively flat tibiofemoral contact regions.

In the best case scenario, in order to minimize the possible information loss that can occur in the implementation of the cartilage composition from MRI into the models, *e.g.* due to interpolation, the element size should be equal to the resolution in the MRI. Nonetheless, the use of a coarser element mesh in the models may improve the repeatability of the results between separate scans through smoothing and interpolation of the MR data. However, the use of a coarser mesh also smooths out the small variations in the orientations of the collagen fibrils within the tissue. Therefore, the use of a finer element mesh (*e.g.* submodeling (study **II**) or by adopting the compartment model approach (study **III**)) can make it easier to reveal the changes in the cartilage composition and hence lead to more accurate and more localized results.

However, the main purpose of the studies was to investigate the effect of subject-specific variations in the orientations of the collagen fibrils and in FCD in comparison to generic or alternative distributions. Therefore, the behavior between the models with alternative composition and the conclusion drawn from them remain the same, even if there were to be some uncertainties in the determination or implementation of the tissue composition from MRI into the models.

Second, certain compromises were needed in the models, *e.g.*, due to the tissue and model geometries. In study **I**, due to 2-D geometry, the middle zone in the tibial and femoral cartilages and the bulk meniscus were implemented with random fibrils instead of the tangentially and circumferentially oriented fibrils, respectively. Similarly, the split-line pattern of collagen fibrils in cartilage could not be implemented into the 2-D geometry. In study **II**, the middle

layers in the cartilages were implemented with a mean fibril orientation ranging from 0° (superficial) in the arcade-like structure to 90° (deep), which is 45° degrees with respect to the cartilage surface. This was done due to the local multilaminar appearance in the collagen architecture as obtained from MRI, which would have made the implementation of the arcade-like structure cumbersome and even potentially inaccurate, particularly in the deep tissue.

In addition, in all the models, including the subject-specific models, the femoral cartilages were implemented with generic depth dependent tissue compositions. Therefore, this eliminates any possible uncertainties in the determination of the zonal boundaries in studies **I** and **II**, due to the convexity of the femoral cartilage tissue with respect to the main magnetic field. In study **III**, the femoral cartilage was also implemented with generic depth-dependent FCD distribution. This was done due to the thickness of the femoral cartilage, which was locally as low as one pixel in the sodium MR images, and this might have provided a non-realistic estimate of the FCD value in these regions of the femoral cartilage. Furthermore, the implementation of similar cartilage tissue compositions in the femoral cartilages into each model made it possible to make a more valid comparison of the results in the tibial cartilage between the models in each study. In addition, the tibial cartilages in studies **III** and **IV** were implemented with constant depth dependent collagen architectures, as this standardization of the depth-wise variation of collagen fibril orientations in the models permits a better estimate of the effect of the FCD variation on the knee joint mechanics.

Third, the loading and boundary conditions in the models have their limitations. In studies **II** and **IV**, the implemented gait loading was obtained from the literature [233, 234] instead of a subject-specifically measured gait cycle. The differences in gait patterns between subjects may cause alterations in the distribution of loads at specific time points during the stance [214]. Hence, in order to obtain a subject-specific estimate of the joint condition, it would be preferable to utilize the subject-specific gait information. However, again this simplification does not affect the results and conclusions

emerging from the studies, since the purpose was to investigate the influence of the tissue compositions on joint mechanics. Furthermore, in studies **I,II** and **IV**, and in the compartment models in study **III**, the ligaments were not included into the model geometries. Instead, the effect of the ligaments were taken into account in the boundary conditions and in the implemented forces and motions. In addition, the effect of the ligaments would be identical between the models in each study, and therefore, would not affect the conclusions.

Finally, all the studies included only one test subject (the results from the second subject in study **I** were not published). As the cartilage geometries and compositions can vary between subjects, *e.g.*, according to the joint status (OA), also the absolute results are likely to vary from one subject to the next.

Despite the limitations in the studies, it should be emphasized that in the currently described knee joint models in the literature, the FRPVE and in particular, the FRPVES material properties and the tissue composition which were implemented here, have been either neglected or are based on values from the literature. For example, typically generic, constant zone thicknesses are applied (as in models *IV* and *V* in study **I** and in *literature model* in study **II**), hence the combination of imaging and biomechanical modeling applying the methods presented here represents a step towards the realization of subject-specific evaluation of joint mechanics with computational methods.

# 9 Summary and Conclusions

In these studies, the subject-specific variation of collagen fibril orientations and fixed charge density of articular cartilage were derived from *in vivo* MRI data. Their roles were investigated on the cartilage response to every-day loading scenarios, *e.g.* standing and walking, using 2-D and 3-D biomechanical models of the knee joint. Specifically, this was achieved by defining the collagen architectures of tibial cartilages in 2-D and 3-D using $T_2$ maps of clinical MR data sets and the models based on those were simulated under impact loading and during the stance phase of gait (one step). Furthermore, the FCD distribution of tibial cartilage of a healthy volunteer was calculated from sodium MRI and its effect was investigated on the knee joint response to standing (static, creep load) and during gait. The models with subject-specific collagen architectures and FCD distributions were compared to models with alternative compositions and to those with generic, non-specific, tissue compositions.

**The main conclusions from the studies:**

**Study I** The patient-specific variations in the zone thicknesses of cartilage alter the local stress and strain distributions throughout the width of the tibial cartilage. The results also suggest that minor inaccuracies in the collagen architecture, *e.g.* caused by the limited resolution of MRI or the use of generic collagen architecture, may lead to significant uncertainties in computational model prediction of the mechanics and condition of the knee joint. Specifically, the results highlight the importance of the superficial zone of cartilage in distributing the stresses, strains and pore pressures in the knee joint cartilage.

**Study II** The 3-D variation of the patient-specific collagen architecture (as obtained from MRI) influences the distribution of

load in a depth-, location- and time-dependent manner in the tibial cartilage during gait. Submodeling can be adapted to evaluate the effect of patient-specific collagen architecture at any location in the knee joint (in 3-D) and this also makes it possible to achieve a more precise implementation of cartilage structure into the model simultaneously improving the model accuracy.

**Study III** The results demonstrate that the subject-specific variation in FCD of cartilage (*e.g.* determined from the sodium MRI) modulates the mechanical response of human knee joint cartilage while the subject is standing (under static loading) in accordance with the spatial variation of FCD. Hence, the subject-specific FCD and the swelling of the tissue should be taken into account when evaluating local strains of cartilage in the knee, especially for diagnostic purposes.

**Study IV** The results demonstrate that FCD has an effect on the mechanical response of cartilage also during dynamic loading of the knee. The results also suggest that cartilage FCD has even more of an influence on knee joint function when the cartilage tissue degenerates, such as in OA. This may be important to consider when evaluating through modeling possible failure points in joints.

In conclusion, the subject-specific variation of collagen orientations and FCD modulate the cartilage response to both static and dynamic loading, such as standing and walking. The determination of the cartilage tissue composition from clinical and pre-clinical MRI is also feasible and may be advantageous when evaluating the subject-specific joint mechanics, particularly the condition of the joint. The presented modeling techniques are able to reveal the compositional variation in the cartilage tissue and its influence on the joint mechanics with the precision provided by the imaging modality in use. The presented methods can therefore be a springboard for developing a diagnostic tool to investigate the joint condi-

tion and possible failure sites in joint tissues as well as functioning as a clinical tool, *e.g.*, to evaluate the need for surgical interventions.

## 9.1 FUTURE ASPECTS

Knee joint modelling has progressed a long way from the linearly elastic models to the fibril-reinforced multimodal approaches available today. However, there is still room for improvement.

With respect to advancing the findings emerging from the present thesis, the first step forward will include further model validation and increasing the number of test subjects. As highlighted throughout the thesis, the tissue composition as well as the loading patterns vary between individuals and therefore the methods presented here should also be applied to larger subject groups and to subjects with varying (clinically diagnosed) joint conditions. In addition, the use of follow-up data would be extremely valuable as a way of validating the capability of the model to assess the condition of the joint and to pinpoint possible failure sites in the knee.

Second, the subject-specific joint modelling and, in particular, the implementation of data reflecting the subject-specific composition of cartilage into the model still lacks an accurate depiction of tissue fluid and, most importantly, fluid flow in and out of the cartilage tissue. It is known that the fluid content and fluid flow in the tissue are altered during the progression of OA. Therefore, taking these factors into account might be one way to improve how well the model is able to predict joint mechanics. The clinical methods to evaluate the fluid content (*e.g.* $T_1$ and $T_{1\rho}$ of MRI) could be more profoundly studied for the use of joint modeling. In general, the development of the clinical imaging modalities and methods will undoubtedly be of benefit also for the future development of joint modeling.

Third, the modeled physical activities could be (even at the moment) expanded to cover more than the most common gait and standing patterns, *e.g.* kneeling, stair-climbing, jumping etc. This could also allow the model to evaluate possible causes of knee pain,

*e.g.,* during a certain activity or in a particular joint orientation.

Finally, in order to forge the presented modeling methods into a clinically feasible tool, the segmentation of image data and meshing should be automated. Currently, those two phases take most of the time in the model creation. In particular, testing of the element mesh and convergence criteria for the model convergence are laborious and time-consuming.

Due to the work already done and the work ahead, biomechanical modeling when combined with clinical imaging modalities is an auspicious method to aid, *e.g.*, clinicians with joint diagnostics.

# *Bibliography*


[1] W. C. Mow, W. Y. Gu, and F. H. Chen, "Structure and Function of Articular Cartilage and Meniscus," in *Basic Orthopaedic Biomechanics and Mechano-Biology*, 3rd ed., V. C. Mow and R. Huiskes, eds. (Lippincott Williams & Wilkins, Philadelphia, 2005), pp. 181–258.

[2] R. K. Korhonen, M. S. Laasanen, J. Toyras, R. Lappalainen, H. J. Helminen, and J. S. Jurvelin, "Fibril reinforced poroelastic model predicts specifically mechanical behavior of normal, proteoglycan depleted and collagen degraded articular cartilage," *J Biomech* **36,** 1373–1379 (2003).

[3] M. S. Laasanen, J. Töyräs, R. K. Korhonen, J. Rieppo, S. Saarakkala, M. T. Nieminen, J. Hirvonen, and J. S. Jurvelin, "Biomechanical properties of knee articular cartilage," *Biorheology* **40,** 133–140 (2003).

[4] V. C. Mow, W. Zhu, and A. Ratcliffe, "Structure and function of articular cartilage and meniscus," in *Basic orthopaedic biomechanics*, V. C. Mow and W. C. Hayes, eds. (Raven Press, Ltd, New York, 1991), pp. 143–198.

[5] A. Benninghoff, "Form und bau der gelenkknorpel in ihren beziehungen zur function. II. Der aufbau des gelenkknorpels in seinen beziehungen zur funktion," *Zeitschrift fur Zellforschung* **2,** 783–862 (1925).

[6] J. M. Clark, "The organisation of collagen fibrils in the superficial zones of articular cartilage," *J Anat* **171,** 117–130 (1990).

[7] L. P. Li, M. D. Buschmann, and A. Shirazi-Adl, "A fibril reinforced nonhomogeneous poroelastic model for articular cartilage: inhomogeneous response in unconfined compression," *J Biomech* **33,** 1533–41. (2000).

[8] I. I. Kiviranta, J. J. Jurvelin, M. M. Tammi, A. M. A. Säämänen, and H. J. H. Helminen, "Microspectrophotometric quantitation of glycosaminoglycans in articular cartilage sections stained with Safranin O," *Histochemistry* **82,** 249–255 (1985).

[9] J. Rieppo, M. M. Hyttinen, R. Lappalainen, J. S. Jurvelin, and H. J. Helminen, "Spatial determination of water, collagen and proteoglycan contents by fourier transform infrared imaging and digital densitometry," *Trans Orthop Res Soc* **29,** 1021 (2004).

[10] L. M. Lesperance, M. L. Gray, D. Burstein, and B. D. Lesperance LM, Gray ML, "Determination of fixed charge density in cartilage using nuclear magnetic resonance," *Journal of Orthopaedic Research* **10,** 1–13 (1992).

[11] J. Rieppo, J. Töyräs, M. T. Nieminen, V. Kovanen, M. M. Hyttinen, R. K. Korhonen, J. S. Jurvelin, and H. J. Helminen, "Structure-Function Relationships in Enzymatically Modified Articular Cartilage," *Cells Tissues Organs* **175,** 121–132 (2003).

[12] R. A. Bank, M. Soudry, A. Maroudas, J. Mizrahi, and J. M. TeKoppele, "The increased swelling and instantaneous deformation of osteoarthritic cartilage is highly correlated with collagen degradation," *Arthritis rheum* **43,** 2202–2210 (2000).

[13] J. A. Buckwalter and H. J. Mankin, "Articular Cartilage, Part II: Degeneration and osteoarthritis, repair, regeneration, and transplantation," *J Bone Joint Surg Am* **79,** 612–632 (1997).

[14] J. A. Buckwalter and J. Martin, "Degenerative joint disease," *Clinical Symposia* **47,** 1–32 (1995).

[15] J.-A. Choi and G. E. Gold, "MR Imaging of Articular Cartilage Physiology," *Magnetic Resonance Imaging Clinics of North America* **19,** 249–282 (2011).

[16] G. E. Gold, C. A. Chen, S. Koo, B. A. Hargreaves, and N. K. Bangerter, "Recent advances in MRI of articular cartilage," *AJR Am J Roentgenol* **193,** 628–638 (2009).

[17] S. Trattnig, S. Domayer, G. W. Welsch, T. Mosher, and F. Eckstein, "MR imaging of cartilage and its repair in the knee - a review," *European Radiology* **19,** 1582–1594 (2009).

[18] A. Borthakur, E. Mellon, S. Niyogi, W. Witschey, and J. B. Kneeland, "Sodium and T 1rho MRI for molecular and diagnostic imaging of articular cartilage y," 781–821 (2006), doi:10.1002/nbm.

[19] M. J. Nissi, J. Rieppo, J. Töyräs, M. S. Laasanen, I. Kiviranta, M. T. Nieminen, and J. S. Jurvelin, "Estimation of mechanical properties of articular cartilage with MRI – dGEMRIC, T2 and T1 imaging in different species with variable stages of maturation," *Osteoarthritis and cartilage / OARS, Osteoarthritis Research Society* **15,** 1141–1148 (2007).

[20] M. T. Nieminen, J. Töyräs, J. Rieppo, M. J. Silvennoinen, J. M. Hakumäki, M. M. Hyttinen, H. J. Helminen, and J. S. Jurvelin, "T2 relaxation reveals spatial collagen architecture in articular cartilage: a comparative quantitative MRI and polarized light microscopic study," *Magn Reson Med* **46,** 487–493 (2001).

[21] M. J. Nissi, J. Rieppo, J. Toyras, M. S. Laasanen, I. Kiviranta, J. S. Jurvelin, and M. T. Nieminen, "T2 relaxation time mapping reveals age- and species-related diversity of collagen network architecture in articular cartilage," *Osteoarthritis and cartilage / OARS, Osteoarthritis Research Society* **14,** 1265–1271 (2006).

[22] Y. Xia, J. B. Moody, N. Burton-Wurster, and G. Lust, "Quantitative in situ correlation between microscopic MRI and polarized light microscopy studies of articular cartilage.," *Osteoarthritis and cartilage / OARS, Osteoarthritis Research Society* **9,** 393–406 (2001).

[23] R. Reddy, E. K. Insko, E. A. Noyszewski, R. Dandora, J. B. Kneeland, and J. S. Leigh, "Sodium MRI of Human Articular Cartilage In Vivo," *Magnetic resonance in medicine* **39,** 697–701 (1998).

[24] E. M. Shapiro, A. Borthakur, A. Gougoutas, and R. Reddy, "23Na MRI accurately measures fixed charge density in articular cartilage.," *Magnetic Resonance in Medicine* **47,** 284–291 (2002).

[25] A. J. Wheaton, A. Borthakur, E. M. Shapiro, R. R. Regatte, S. V. S. Akella, J. B. Kneeland, and R. Reddy, "Proteoglycan Loss in Human Knee Cartilage : Quantitation with Sodium MR Imaging — Feasibility Study 1," *Radiology* **231,** 900–5. (2004).

[26] M. Adouni and A. Shirazi-Adl, "Evaluation of knee joint muscle forces and tissue stresses-strains during gait in severe OA versus normal subjects.," *Journal of orthopaedic research : official publication of the Orthopaedic Research Society* **32,** 69–78 (2014).

[27] M. Akbarshahi, J. W. Fernandez, A. G. Schache, and M. G. Pandy, "Subject-specific evaluation of patellofemoral joint biomechanics during functional activity.," *Medical engineering & physics* **36,** 1122–33 (2014).

[28] M. E. Mononen, J. S. Jurvelin, and R. K. Korhonen, "Effects of radial tears and partial meniscectomy of lateral meniscus on the knee joint mechanics during the stance phase of the gait cycle—A 3D finite element study," *Journal of Orthopaedic Research* **31,** 1208–1217 (2013).

[29] R. Mootanah, C. W. Imhauser, F. Reisse, D. Carpanen, R. W. Walker, M. F. Koff, M. W. Lenhoff, S. R. Rozbruch, A. T. Fragomen, Z. Dewan, Y. M. Kirane, K. Cheah, J. K. Dowell, and H. J. Hillstrom, "Development and validation of a computational model of the knee joint for the evaluation of surgical treatments for osteoarthritis.," *Computer methods in biomechanics and biomedical engineering* **17,** 1502–17 (2014).

[30] V. C. Mow, D. C. Fithian, and M. A. Kelly, "Fundamentals of articular cartilage and meniscus biomechanics," in *Articular cartilage and knee joint function: basic science and arthroscopy*, J. W. Ewing, ed. (Raven Press Ltd., New York, 1990), pp. 1–18.

[31] S. D. Masouros, A. M. J. Bull, and A. A. Amis, "(i) Biomechanics of the knee joint," *Orthopaedics and Trauma* **24,** 84–91 (2010).

[32] H. J. Mankin, "The response of articular cartilage to mechanical injury.," *The Journal of bone and joint surgery. American volume* **64,** 460–6 (1982).

[33] V. C. Mow, S. C. Kuei, W. M. Lai, and C. G. Armstrong, "Biphasic creep and stress relaxation of articular cartilage in compression: Theory and experiments," *J Biomech Eng* **102,** 73–84 (1980).

[34] J. A. Buckwalter, H. J. Mankin, and A. J. Grodzinsky, "Articular cartilage and osteoarthritis.," *Instructional course lectures* **54,** 465–80 (2005).

[35] V. C. Mow and X. E. Guo, "Mechano-Electrochemical Properties Of Articular Cartilage: Their Inhomogeneities and Anisotropies," *Annual Review of Biomedical Engineering* **4,** 175–209 (2002).

[36] V. C. Mow, M. H. Holmes, and W. Michael Lai, "Fluid transport and mechanical properties of articular cartilage: A review," *Journal of Biomechanics* **17,** 377–394 (1984).

[37] V. C. Mow, A. Ratcliffe, and A. Robin Poole, "Cartilage and diarthrodial joints as paradigms for hierarchical materials and structures," *Biomaterials* **13,** 67–97 (1992).

[38] J. A. Buckwalter and H. J. Mankin, "Articular cartilage. Part I: Tissue design and chondrocyte-matrix interactions," *Journal of Bone and Joint Surgery (American)* **79A,** 600–611 (1997).

[39] D. R. D. Eyre, M. A. M. Weis, and J. J. J. Wu, "Articular cartilage collagen: an irreplaceable framework?," *European cells & materials* **12,** 57–63 (2006).

[40] M. M. Huber, S. S. Trattnig, and F. F. Lintner, "Anatomy, biochemistry, and physiology of articular cartilage," *Invest Radiol* **35,** 573–580 (2000).

[41] D. W. Goodwin, Y. Z. Wadghiri, H. Zhu, C. J. Vinton, E. D. Smith, and J. F. Dunn, "Macroscopic structure of articular cartilage of the tibial plateau: influence of a characteristic matrix architecture on MRI appearance," *AJR. American journal of roentgenology* **182,** 311–318 (2004).

[42] J. M. Clark, "The organization of collagen in cryofractured rabbit articular cartilage: a scanning electron microscopic study," *J Orthop Res* **3,** 17–29 (1985).

[43] J. M. J. Clark, "Variation of collagen fiber alignment in a joint surface: a scanning electron microscope study of the tibial plateau in dog, rabbit, and man," *Journal of orthopaedic research : official publication of the Orthopaedic Research Society* **9,** 246–257 (1991).

[44] M. J. Kääb, I. a. Gwynn, and H. P. Nötzli, "Collagen fibre arrangement in the tibial plateau articular cartilage of man and other mammalian species.," *Journal of anatomy* **193 ( Pt 1,** 23–34 (1998).

[45] J. P. Arokoski, J. S. Jurvelin, U. Väätäinen, and H. J. Helminen, "Normal and pathological adaptations of articular cartilage to joint loading," *Scand J Med Sci Sports* **10,** 186–198 (2000).

[46] X. Bi, G. Li, S. B. Doty, and N. P. Camacho, "A novel method for determination of collagen orientation in cartilage by Fourier transform infrared imaging spectroscopy (FT-IRIS)," *Osteoarthritis and cartilage / OARS, Osteoarthritis Research Society* **13,** 1050–1058 (2005).

[47] A. M. Chaudhari, P. L. Briant, S. L. Bevill, S. Koo, and T. P. Andriacchi, "Knee kinematics, cartilage morphology, and osteoarthritis after ACL injury," *Med Sci Sports Exerc* **40,** 215–222 (2008).

[48] J. E. Kurkijarvi, M. J. Nissi, J. Rieppo, J. Toyras, I. Kiviranta, M. T. Nieminen, and J. S. Jurvelin, "The zonal architecture of human articular cartilage described by T2 relaxation time in the presence of Gd-DTPA2," *Magnetic Resonance Imaging* **26,** 602–607 (2008).

[49] Y. Xia, J. B. Moody, H. Alhadlaq, and J. Hu, "Imaging the physical and morphological properties of a multi-zone young articular cartilage at microscopic resolution," *Journal of Magnetic Resonance Imaging* **17,** 365–374 (2003).

[50] P. Bottcher, M. Zeissler, J. Maierl, V. Grevel, and G. Oechtering, "Mapping of split-line pattern and cartilage thickness of selected donor and recipient sites for autologous osteochondral transplantation in the canine stifle joint," *Vet Surg* **38,** 696–704 (2009).

[51] S. J. S. Erickson, R. W. R. Prost, and M. E. M. Timins, "The "magic angle" effect: background physics and clinical relevance," (1993).

[52] M. J. Kääb, K. Ito, B. Rahn, J. M. Clark, and H. P. Nötzli, "Effect of Mechanical Load on Articular Cartilage Collagen Structure: A Scanning Electron-Microscopic Study," *Cells Tissues Organs* **167,** 106–120 (2000).

[53] S. Saarakkala and P. Julkunen, "Specificity of Fourier Transform Infrared (FTIR) Microspectroscopy to Estimate Depth-Wise Proteoglycan Content in Normal and Osteoarthritic Human Articular Cartilage," *Cartilage* **1,** 262–269 (2010).

[54] S. S. Chen, Y. H. Falcovitz, R. Schneiderman, A. Maroudas, and R. L. Sah, "Depth-dependent compressive properties of normal aged human femoral head articular cartilage : relationship to fixed charge density," 561–569 (2001), doi:10.1053/joca.2001.0424.

[55] P. Tanska, S. M. Turunen, S. K. Han, P. Julkunen, W. Herzog, and R. K. Korhonen, "Superficial collagen fibril modulus and pericellular fixed charge density modulate chondrocyte volumetric behaviour in early osteoarthritis," *Computational and mathematical methods in medicine* **2013,** 164146 (2013).

[56] A. Maroudas and M. Venn, "Chemical composition and swelling of normal and osteoarthrotic femoral head cartilage. II. Swelling," *Ann Rheum Dis* **36,** 399–406 (1977).

[57] A. I. Maroudas, "Balance between swelling pressure and collagen tension in normal and degenerate cartilage," *nature* **260,** 808–9. (1976).

[58] A. Maroudas and R. Schneiderman, ""Free" and "exchangeable" or "trapped" and "non-exchangeable" water in cartilage," *J Orthop Res* **5,** 133–138 (1987).

[59] A. Maroudas, P. Bullough, S. A. Swanson, and M. A. Freeman, "Permeability of articular cartilage," *J Bone Joint Surg Br* **219,** 166–77. (1968).

[60] W. C. Bae, V. W. Wong, J. Hwang, J. M. Antonacci, G. E. Nugent-Derfus, M. E. Blewis, M. M. Temple-Wong, and R. L. Sah, "Wear-lines and split-lines of human patellar cartilage: relation to tensile biomechanical properties," *Osteoarthritis and cartilage / OARS, Osteoarthritis Research Society* **16,** 841–845 (2008).

[61] S. S. Akizuki, V. C. V. Mow, F. F. Müller, J. C. J. Pita, D. S. D. Howell, and D. H. D. Manicourt, "Tensile properties of human knee joint cartilage: I. Influence of ionic conditions, weight bearing, and fibrillation on the tensile modulus," *Journal of orthopaedic research : official publication of the Orthopaedic Research Society* **4,** 379–392 (1986).

[62] P. Kiviranta, J. Rieppo, R. K. Korhonen, P. Julkunen, J. Töyräs, and J. S. Jurvelin, "Collagen network primarily controls Poisson's ratio of bovine articular cartilage in compression," *Journal of Orthopaedic Research* **24,** 690–699 (2006).

[63] R. M. R. Schinagl, D. D. Gurskis, A. C. A. Chen, and R. L. R. Sah, "Depth-dependent confined compression modulus of full-thickness bovine articular cartilage," *Journal of orthopaedic research : official publication of the Orthopaedic Research Society* **15,** 499–506 (1997).

[64] L. A. L. Setton, H. H. Tohyama, and V. C. V. Mow, "Swelling and curling behaviors of articular cartilage," *Journal of Biomechanical Engineering* **120,** 355–361 (1998).

[65] J. Z. Wu and W. Herzog, "Elastic anisotropy of articular cartilage is associated with the microstructures of collagen fibers and chondrocytes," *Journal of Biomechanics* **35,** 931–942 (2002).

[66] J. L. Silverberg, S. Dillavou, L. Bonassar, and I. Cohen, "Anatomic variation of depth-dependent mechanical properties in neonatal bovine articular cartilage," *Journal of Orthopaedic Research* **31,** 686–691 (2013).

[67] S. Federico and W. Herzog, "On the anisotropy and inhomogeneity of permeability in articular cartilage," *Biomechanics and Modeling in Mechanobiology* **7,** 367–378 (2008).

[68] J. M. Mansour, "Biomechanics of Cartilage," in *Kinesiology: The Mechanics and Pathomechanics of Human Movement*, C. Oatis, ed. (Lippincott Williams and Wilkins, 2004), pp. 66–79.

[69] A. Maroudas, "Biophysical chemistry of cartilaginous tissues with special reference to solute and fluid transport," *Biorheology* **12,** 233–48. (1975).

[70] J. Mizrahi, A. Maroudas, Y. Lanir, I. Ziv, and T. J. Webber, "The "instantaneous" deformation of cartilage: effects of collagen fiber orientation and osmotic stress," *Biorheology* **23,** 311–330 (1986).

[71] J. K. Suh, Z. Li, and S. L. Woo, "Dynamic behavior of a biphasic cartilage model under cyclic compressive loading," *J Biomech* **28,** 357–364 (1995).

[72] E. A. Makris, P. Hadidi, and K. a. Athanasiou, "The knee meniscus: structure-function, pathophysiology, current repair techniques, and prospects for regeneration.," *Biomaterials* **32,** 7411–31 (2011).

[73] S. D. Masouros, I. D. McDermott, A. A. Amis, and A. M. J. Bull, "Biomechanics of the meniscus-meniscal ligament construct of the knee," *Knee Surg Sports Traumatol Arthrosc* **16,** 1121–1132 (2008).

[74] C. R. Clark and J. A. Ogden, "Development of the menisci of the human knee joint. Morphological changes and their potential role in childhood meniscal injury.," *The Journal of bone and joint surgery. American volume* **65,** 538–47 (1983).

[75] R. M. Aspden, Y. E. Yarker, and D. W. Hukins, "Collagen orientations in the meniscus of the knee joint," *J Anat* **140,** 371–380 (1985).

[76] G. A. Ateshian and C. T. Hung, "Patellofemoral Joint Biomechanics and Tissue Engineering," *Clinical Orthopaedics and Related Research* **&NA;,** 81–90 (2005).

[77] G. A. Ateshian, L. J. Soslowsky, and V. C. Mow, "Quantitation of articular surface topography and cartilage thickness in knee joints using stereophotogrammetry," *Journal of Biomechanics* **24,** 761–776 (1991).

[78] I. D. McDermott, S. D. Masouros, and A. A. Amis, "Biomechanics of the menisci of the knee," *Current Orthopaedics* **22,** 193–201 (2008).

[79] P. G. P. Bullough, L. L. Munuera, J. J. Murphy, and A. M. A. Weinstein, "The strength of the menisci of the knee as it relates to their fine structure," *The Journal of bone and joint surgery. British volume* **52,** 564–567 (1970).

[80] I. D. McDermott, S. D. Masouros, A. M. J. Bull, and A. A. Amis, "Anatomy," in *The Meniscus*, 1st ed., P. Beaufils and R. Verdonk, eds. (Springer-Verlag, Berlin, Heidelberg, 2010), pp. 11–18.

[81] M. Tissakht and A. M. Ahmed, "Tensile Stress-Strain Characteristics of the Human Meniscal Material," *J. Bromechmics* **28,** 411–422 (1995).

[82] K. Lechner, M. L. Hull, and S. M. Howell, "Is the circumferential tensile modulus within a human medial meniscus affected by the test sample location and cross-sectional area?," *Journal of orthopaedic research : official publication of the Orthopaedic Research Society* **18,** 945–51 (2000).

[83] M. A. Sweigart, C. F. Zhu, D. M. Burt, P. D. DeHoll, C. M. Agrawal, T. O. Clanton, and K. A. Athanasiou, "Intraspecies and Interspecies Comparison of the Compressive Properties of the Medial Meniscus," *Annals of Biomedical Engineering* **32,** 1569–1579 (2004).

[84] H. E. Cabaud, "Biomechanics of the anterior cruciate ligament.," *Clinical orthopaedics and related research* 26–31 (1983).

[85] S. Claes, E. Vereecke, M. Maes, J. Victor, P. Verdonk, and J. Bellemans, "Anatomy of the anterolateral ligament of the knee," *Journal of Anatomy* **223,** 321–328 (2013).

[86] D. L. Butler, F. R. Noyes, and E. S. Grood, "Ligamentous restraints to anterior-posterior drawer in the human knee. A biomechanical study.," *The Journal of bone and joint surgery. American volume* **62,** 259–70 (1980).

[87] L.-Y. Woo, T. Q. Lee, S. D. Abramowitch, and T. W. Gilbert, "Structure and Function of Ligaments and Tendons," in *Basic Orthopaedic Biomechanics and Mechano-Biology*, 3rd ed., V. C. Mow and R. Huiskes, eds. (Lippincott Williams & Wilkins, Philadelphia, 2005), pp. 301–342.

[88] R. D. Altman and G. E. Gold, "Atlas of individual radiographic features in osteoarthritis, revised.," *Osteoarthritis and cartilage / OARS, Osteoarthritis Research Society* **15 Suppl A,** A1–56 (2007).

[89] M. Huang and M. E. Schweitzer, "The Role of Radiology in the Evolution of the Understanding of Articular Disease Online SA-CME," *Radiology* **273,** S1–22 (2014).

[90] F. W. Roemer, F. Eckstein, D. Hayashi, and A. Guermazi, "The role of imaging in osteoarthritis," *Best Practice & Research Clinical Rheumatology* **28,** 31–60 (2014).

[91] D. J. Hunter, Y. Q. Zhang, X. Tu, M. Lavalley, J. B. Niu, S. Amin, A. Guermazi, H. Genant, D. Gale, and D. T. Felson, "Change in joint space width: hyaline articular cartilage loss or alteration in meniscus?," *Arthritis and Rheumatism* **54,** 2488–95 (2006).

[92] R. Kijowski, D. G. Blankenbaker, P. T. Stanton, J. P. Fine, and A. a. De Smet, "Radiographic findings of osteoarthritis versus arthroscopic findings of articular cartilage degeneration in the tibiofemoral joint.," *Radiology* **239,** 818–824 (2006).

[93] R. Burgkart, C. Glaser, A. Hyhlik-Dürr, K. H. Englmeier, M. Reiser, and F. Eckstein, "Magnetic resonance imaging-based assessment of cartilage loss in severe osteoarthritis: accuracy, precision, and diagnostic value.," *Arthritis and rheumatism* **44,** 2072–7 (2001).

[94] G. Gold, D. Burstein, B. Dardzinski, P. Lang, F. Boada, and T. Mosher, "MRI of articular cartilage in OA: novel pulse sequences and compositional/functional markers," *Osteoarthritis and Cartilage* **14,** 76–86 (2006).

[95] T. Stammberger, F. Eckstein, K. H. Englmeier, and M. Reiser, "Determination of 3D cartilage thickness data from MR imaging: computational method and reproducibility in the living.," *Magnetic resonance in medicine : official journal of the Society of Magnetic Resonance in Medicine / Society of Magnetic Resonance in Medicine* **41,** 529–36 (1999).

[96] D. T. Felson, M. C. Nevitt, M. Yang, M. Clancy, J. Niu, J. C. Torner, C. E. Lewis, P. Aliabadi, B. Sack, C. McCulloch, and Y. Zhang, "A new approach yields high rates of radiographic progression in knee osteoarthritis.," *The Journal of rheumatology* **35,** 2047–54 (2008).

[97] D. D. Chan and C. P. Neu, "Probing articular cartilage damage and disease by quantitative magnetic resonance imaging.," *Journal of the Royal Society, Interface / the Royal Society* **10,** 20120608 (2013).

[98] C. P. Neu, "Functional imaging in OA: role of imaging in the evaluation of tissue biomechanics.," *Osteoarthritis and cartilage / OARS, Osteoarthritis Research Society* **22,** 1349–59 (2014).

[99] D. D. D'Lima, S. Hashimoto, P. C. Chen, C. W. Colwell, and M. K. Lotz, "Human chondrocyte apoptosis in response to mechanical injury.," *Osteoarthritis and cartilage / OARS, Osteoarthritis Research Society* **9,** 712–9 (2001).

[100] B. J. Ewers, D. Dvoracek-Driksna, M. W. Orth, and R. C. Haut, "The extent of matrix damage and chondrocyte death in mechanically traumatized articular cartilage explants depends on rate of loading.," *Journal of orthopaedic research : official publication of the Orthopaedic Research Society* **19,** 779–84 (2001).

[101] I. Hannila, M. T. Nieminen, E. Rauvala, O. Tervonen, and R. Ojala, "Patellar cartilage lesions: comparison of magnetic resonance imaging and T2 relaxation-time mapping," *Acta radiologica* **48,** 444–448 (2007).

[102] R. Kijowski, "Clinical Cartilage Imaging of the Knee and Hip Joints," *American Journal of Roentgenology* **195,** 618–628 (2010).

[103] P. Kiviranta, J. Toyras, M. T. Nieminen, M. S. Laasanen, S. Saarakkala, H. J. Nieminen, M. J. Nissi, and J. S. Jurvelin, "Comparison of novel clinically applicable methodology for sensitive diagnostics of cartilage degeneration," *European cells & materials* **13,** 46–55 (2007).

[104] M. D. Crema, F. W. Roemer, M. D. Marra, D. Burstein, G. E. Gold, F. Eckstein, T. Baum, T. J. Mosher, J. A. Carrino, and A. Guermazi, "Articular Cartilage in the Knee: Current MR Imaging Techniques and Applications in Clinical Practice and Research," *Radiographics* **31,** 37–U76 (2011).

[105] P. Julkunen, W. Wilson, J. S. Jurvelin, J. Rieppo, C. J. Qu, M. J. Lammi, and R. K. Korhonen, "Stress-relaxation of human patellar articular cartilage in unconfined compression: prediction of mechanical response by tissue composition and structure," *J Biomech* **41,** 1978–1986 (2008).

[106] J. J. Rubenstein, M. M. Recht, D. G. D. Disler, J. J. Kim, and R. M. R. Henkelman, "Laminar structures on MR images of articular cartilage," (1997).

[107] A. Williams, Y. Qian, D. Bear, and C. R. Chu, "Assessing degeneration of human articular cartilage with ultra-short echo time (UTE) T2* mapping," *Osteoarthritis and cartilage / OARS, Osteoarthritis Research Society* **18,** 539–546 (2010).

[108] D. D. Chan, L. Cai, K. D. Butz, S. B. Trippel, E. A. Nauman, and C. P. Neu, "In vivo articular cartilage deformation: noninvasive quantification of intratissue strain during joint contact in the human knee.," *Scientific reports* **6,** 19220 (2016).

[109] D. D. Chan, C. P. Neu, and M. L. Hull, "In situ deformation of cartilage in cyclically loaded tibiofemoral joints by displacement-encoded MRI.," *Osteoarthritis and cartilage / OARS, Osteoarthritis Research Society* **17,** 1461–8 (2009).

[110] A. J. Griebel, S. B. Trippel, and C. P. Neu, "Noninvasive dualMRI-based strains vary by depth and region in human osteoarthritic articular cartilage.," *Osteoarthritis and cartilage / OARS, Osteoarthritis Research Society* **21,** 394–400 (2013).

[111] J. E. Kurkijärvi, M. J. Nissi, I. Kiviranta, J. S. Jurvelin, and M. T. Nieminen, "Delayed gadolinium-enhanced MRI of cartilage (dGEMRIC) and T2 characteristics of human knee articular cartilage: Topographical variation and relationships to mechanical properties," *Magnetic Resonance in Medicine* **52,** 41–46 (2004).

[112] E. Lammentausta, P. Kiviranta, M. J. Nissi, M. S. Laasanen, I. Kiviranta, M. T. Nieminen, and J. S. Jurvelin, "T2 relaxation time and delayed gadolinium-enhanced MRI of cartilage (dGEMRIC) of human patellar cartilage at 1.5 T and 9.4 T: Relationships with tissue mechanical properties," *Journal of orthopaedic research : official publication of the Orthopaedic Research Society* **24,** 366–374 (2006).

[113] M. T. Nieminen, J. Toyras, M. S. Laasanen, J. Silvennoinen, H. J. Helminen, and J. S. Jurvelin, "Prediction of biomechanical properties of articular cartilage with quantitative magnetic resonance imaging," *J Biomech* **37,** 321–328 (2004).

[114] M. H. Levitt, *Spin dynamics: basics of nuclear magnetic resonance*, 2nd ed. (John Wiley & Sons, 2008).

[115] D. W. McRobbie, E. A. Moore, M. J. Graves, and M. R. Prince, *MRI from picture to proton*, 3rd ed. (Cambridge University Press, 2010).

[116] X. Li and S. Majumdar, "Quantitative MRI of articular cartilage and its clinical applications.," *Journal of magnetic resonance imaging : JMRI* **38,** 991–1008 (2013).

[117] E. H. G. Oei, J. Van Tiel, W. H. Robinson, and G. E. Gold, "Quantitative radiologic imaging techniques for articular cartilage composition: Toward early diagnosis and development of disease-modifying therapeutics for osteoarthritis," *Arthritis Care and Research* **66,** 1129–1141 (2014).

[118] F. W. Roemer, M. D. Crema, S. Trattnig, and A. Guermazi, "Advances in imaging of osteoarthritis and cartilage.," *Radiology* **260,** 332–54 (2011).

[119] W. Wirth, M. Nevitt, M.-P. Hellio Le Graverand, O. Benichou, D. Dreher, R. Y. Davies, J. Lee, K. Picha, A. Gimona, S. Maschek, M. Hudelmaier, and F. Eckstein, "Sensitivity to change of cartilage morphometry using coronal FLASH, sagittal DESS, and coronal MPR DESS protocols–comparative data from the Osteoarthritis Initiative (OAI).," *Osteoarthritis and cartilage / OARS, Osteoarthritis Research Society* **18,** 547–54 (2010).

[120] T. J. T. J. Mosher and B. J. B. J. Dardzinski, "Cartilage MRI T2 relaxation time mapping: overview and applications," *Seminars in musculoskeletal radiology* **8,** 355–368 (2004).

[121] E. Staroswiecki, K. L. Granlund, M. T. Alley, G. E. Gold, and B. A. Hargreaves, "Simultaneous estimation of T(2) and apparent diffusion coefficient in human articular cartilage in vivo with a modified three-dimensional double echo steady state (DESS) sequence at 3 T.," *Magnetic resonance in medicine : official journal of the Society of Magnetic Resonance in Medicine / Society of Magnetic Resonance in Medicine* **67,** 1086–96 (2012).

[122] G. H. Welsch, T. C. Mamisch, L. Zak, A. Mauerer, S. Apprich, D. Stelzeneder, S. Marlovits, and S. Trattnig, "Morphological and biochemical T2 evaluation of cartilage repair tissue based on a hybrid double echo at steady state (DESS-T2d) approach.," *Journal of magnetic resonance imaging : JMRI* **34,** 895–903 (2011).

[123] S. Lüssea, H. Claassen, T. Gehrke, J. Hassenpflug, M. Schünke, M. Heller, and C.-C. Glüer, "Evaluation of water content by spatially resolved transverse relaxation times of human articular cartilage," *Magnetic Resonance Imaging* **18,** 423–430 (2000).

[124] C. Liess, S. Lusse, N. Karger, M. Heller, and C.-C. Gluer, "Detection of changes in cartilage water content using MRI T2-mapping in vivo," *Osteoarthritis and Cartilage* **10,** 907–913 (2002).

[125] E. Shapiro, A. Borthakur, J. Kaufman, J. Leigh, and R. Reddy, "Water distribution patterns inside bovine articular cartilage as visualized by1H magnetic resonance imaging," *Osteoarthritis and Cartilage* **9,** 533–538 (2001).

[126] M. Son, S. B. Goodman, W. Chen, B. A. Hargreaves, G. E. Gold, and M. E. Levenston, "Regional variation in T1$\rho$ and T2 times in osteoarthritic human menisci: correlation with mechanical properties and matrix composition.," *Osteoarthritis and cartilage / OARS, Osteoarthritis Research Society* **21,** 796–805 (2013).

[127] A. Borthakur, E. M. Shapiro, J. Beers, S. Kudchodkar, J. B. Kneeland, and R. Reddy, "Sensitivity of MRI to proteoglycan depletion in cartilage: Comparison of sodium and proton MRI," *Osteoarthritis and Cartilage* **8,** 288–293 (2000).

[128] K. E. Keenan, T. F. Besier, J. M. Pauly, E. Han, J. Rosenberg, R. L. Smith, S. L. Delp, G. S. Beaupre, and G. E. Gold, "Prediction of glycosaminoglycan content in human cartilage by age, T1$\rho$ and T2 MRI.," *Osteoarthritis and cartilage / OARS, Osteoarthritis Research Society* **19,** 171–9 (2011).

[129] R. R. Regatte, J. H. Kaufman, E. a. Noyszewski, and R. Reddy, "Sodium and proton MR properties of cartilage during compression," *Journal of Magnetic Resonance Imaging* **10,** 961–967 (1999).

[130] R. Toffanin, V. Mlynárik, S. Russo, P. Szomolányi, a. Piras, and F. Vittur, "Proteoglycan depletion and magnetic resonance parameters of articular cartilage.," *Archives of biochemistry and biophysics* **390,** 235–42 (2001).

[131] C. S. Wong, C. H. Yan, N. J. Gong, T. Li, Q. Chan, and Y. C. Chu, "Imaging biomarker with T1$\rho$ and T2 mappings in osteoarthritis - in vivo human articular cartilage study.," *European journal of radiology* **82,** 647–50 (2013).

[132] C. W. Hayes and J. A. Parellada, "Hayes 1996.pdf," *Topics in magnetic resonance imaging : TMRI* **8,** 51–6 (1996).

[133] Y. Y. Xia, "Magic-angle effect in magnetic resonance imaging of articular cartilage: a review," *Investigative radiology* **35,** 602–621 (2000).

[134] T. C. Dunn, Y. Lu, H. Jin, M. D. Ries, and S. Majumdar, "T2 relaxation time of cartilage at MR imaging: comparison with severity of knee osteoarthritis.," *Radiology* **232,** 592–8 (2004).

[135] E. David-Vaudey, S. Ghosh, M. Ries, and S. Majumdar, "T2 relaxation time measurements in osteoarthritis.," *Magnetic resonance imaging* **22,** 673–82 (2004).

[136] G. Jaccard, S. Wimperis, and G. Bodenhausen, "Multiple-quantum NMR spectroscopy of S=3/2 spins in isotropic phase: A new probe for multiexponential relaxation," *The Journal of Chemical Physics* **85,** 6282 (1986).

[137] G. Madelin, A. Jerschow, and R. R. Regatte, "Sodium relaxation times in the knee joint in vivo at 7T," *NMR in biomedicine* 530–537 (2012), doi:10.1002/nbm.1768.

[138] S. Zbýň, V. Mlynárik, V. Juras, P. Szomolanyi, S. Trattnig, S. Zbyn, V. Mlynarik, V. Juras, P. Szomolanyi, S. Trattnig, S. Zbýň, V. Mlynárik, V. Juras, P. Szomolanyi, and S. Trattnig, "Sodium MR Imaging of Articular Cartilage Pathologies," *Current radiology reports* **2,** 41 (2014).

[139] X. Deligianni, P. Bär, K. Scheffler, S. Trattnig, and O. Bieri, "High-resolution Fourier-encoded sub-millisecond echo time musculoskeletal imaging at 3 Tesla and 7 Tesla," *Magnetic Resonance in Medicine* **70,** 1434–1439 (2013).

[140] S. Haneder, V. Juras, H. J. Michaely, X. Deligianni, O. Bieri, S. O. Schoenberg, S. Trattnig, and Š. Zbýň, "In vivo sodium (23Na) imaging of the human kidneys at 7 T: preliminary results.," *European radiology* **24,** 494–501 (2014).

[141] G. Chang, G. Madelin, O. H. Sherman, E. J. Strauss, D. Xia, M. P. Recht, A. Jerschow, and R. R. Regatte, "Improved assessment of cartilage repair tissue using fluid-suppressed $^{23}$Na inversion recovery MRI at 7 Tesla: preliminary results.," *European radiology* **22,** 1341–9 (2012).

[142] E. K. Insko, J. H. Kaufman, J. S. Leigh, and R. Reddy, "Sodium NMR evaluation of articular cartilage degradation.," *Magnetic resonance in medicine* **41,** 30–4 (1999).

[143] A. Bashir, M. L. Gray, J. Hartke, and D. Burstein, "Nondestructive Imaging of Human Cartilage Glycosaminoglycan Concentration by MRI," **865,** 857–865 (1999).

[144] E. M. Shapiro, "Sodium Visibility and Quantitation in Intact Bovine Articular Cartilage Using High Field 23 Na MRI and MRS," **31,** 24–31 (2000).

[145] G. Madelin, J. Babb, and S. B. Abramson, "Articular cartilage: evaluation with fluid-suppressed 7.0-T sodium MR imaging in subjects with and subjects without osteoarthritis.," *Radiology* **268,** 481–91 (2013).

[146] A. J. Wheaton, A. Borthakur, E. M. Shapiro, R. R. Regatte, S. V. S. Akella, J. B. Kneeland, and R. Reddy, "Proteoglycan loss in human knee cartilage: quantitation with sodium MR imaging–feasibility study.," *Radiology* **231,** 900–5 (2004).

[147] C. H. Moon, J.-h. Kim, T. Zhao, and K. T. Bae, "Quantitative 23Na MRI of Human Knee Cartilage Using Dual-Tuned 1H/23Na Transceiver Array Radiofrequency Coil at 7 Tesla," *Journal of Magnetic Resonance Imaging* **38,** 1063–1072 (2013).

[148] B. Schmitt, S. Zbýn, D. Stelzeneder, V. Jellus, D. Paul, L. Lauer, P. Bachert, and S. Trattnig, "Cartilage quality assessment by using glycosaminoglycan chemical exchange saturation transfer and (23)Na MR imaging at 7 T.," *Radiology* **260,** 257–64 (2011).

[149] R. D. Newbould, S. R. Miller, J. A. W. Tielbeek, L. D. Toms, A. W. Rao, G. E. Gold, R. K. Strachan, P. C. Taylor, P. M. Matthews, and A. P. Brown, "Reproducibility of sodium MRI measures of articular cartilage of the knee in osteoarthritis," *Osteoarthritis and Cartilage* **20,** 29–35 (2012).

[150] L. Wang, Y. Wu, G. Chang, N. Oesingmann, M. E. Schweitzer, A. Jerschow, and R. R. Regatte, "Rapid isotropic 3D-sodium MRI of the knee joint in vivo at 7T.," *Journal of magnetic resonance imaging : JMRI* **30,** 606–14 (2009).

[151] S. Zbýň, D. Stelzeneder, G. H. Welsch, L. L. Negrin, V. Juras, M. E. Mayerhoefer, P. Szomolanyi, W. Bogner, S. E. Domayer, M. Weber, S. Trattnig, S. Zbyn, D. Stelzeneder, G. H. Welsch, L. L. Negrin, V. Juras, M. E. Mayerhoefer, P. Szomolanyi, W. Bogner, S. E. Domayer, M. Weber, and S. Trattnig, "Evaluation of native hyaline cartilage and repair tissue after two cartilage repair surgery techniques with 23Na MR imaging at 7 T: initial experience.," *Osteoarthritis and cartilage / OARS, Osteoarthritis Research Society* **20,** 837–45 (2012).

[152] E. Staroswiecki, N. K. Bangerter, P. T. Gurney, T. Grafendorfer, G. E. Gold, and B. A. Hargreaves, "In Vivo Sodium Imaging of Human Patellar Cartilage With a 3D Cones Sequence at 3 T and 7 T," **451,** 446–451 (2010).

[153] S. Trattnig, Š. Zbý, B. Schmitt, K. Friedrich, V. Juras, and P. Szomolanyi, "Advanced MR methods at ultra-high field ( 7 Tesla ) for clinical musculoskeletal applications," (2012), doi:10.1007/s00330-012-2508-0.

[154] G. Madelin, J.-S. Lee, S. Inati, A. Jerschow, and R. R. Regatte, "Sodium inversion recovery MRI of the knee joint in vivo at 7T.," *Journal of magnetic resonance (San Diego, Calif. : 1997)* **207,** 42–52 (2010).

[155] W. Li, H. Du, R. Scheidegger, Y. Wu, and P. V. Prasad, "Value of precontrast T(1) for dGEMRIC of native articular cartilage.," *Journal of magnetic resonance imaging : JMRI* **29,** 494–7 (2009).

[156] V. Mlynárik, A. Degrassi, R. Toffanin, F. Vittur, M. Cova, and R. S. Pozzi-Mucelli, "Investigation of laminar appearance of articular cartilage by means of magnetic resonance microscopy," *Magnetic Resonance Imaging* **14,** 435–442 (1996).

[157] Y. Xia, "Relaxation anisotropy in cartilage by NMR microscopy ($\mu$MRI) at 14-$\mu$m resolution," *Magnetic resonance in medicine* **39,** 941–949 (1998).

[158] J. E. Berberat, M. J. Nissi, J. S. Jurvelin, and M. T. Nieminen, "Assessment of interstitial water content of articular cartilage with T1 relaxation.," *Magnetic resonance imaging* **27,** 727–32 (2009).

[159] M. J. Nissi, J. Töyräs, M. S. Laasanen, J. Rieppo, S. Saarakkala, R. Lappalainen, J. S. Jurvelin, and M. T. Nieminen, "Proteoglycan and collagen sensitive MRI evaluation of normal and degenerated articular cartilage.," *Journal of orthopaedic research : official publication of the Orthopaedic Research Society* **22,** 557–64 (2004).

[160] M. L. Gray, D. Burstein, Y.-j. Kim, and A. Maroudas, "2007 ELIZABETH WINSTON LANIER AWARD WINNER Magnetic Resonance Imaging of Cartilage Glycosaminoglycan : Basic Principles , Imaging Technique , and Clinical Applications," 281–291 (2008), doi:10.1002/jor.20482.

[161] G. H. Welsch, T. C. Mamisch, T. Hughes, C. Zilkens, S. Quirbach, K. Scheffler, O. Kraff, M. E. Schweitzer, P. Szomolanyi, and S. Trattnig, "In vivo biochemical 7.0 Tesla magnetic resonance: preliminary results of dGEMRIC, zonal T2, and T2* mapping of articular cartilage.," *Investigative radiology* **43,** 619–26 (2008).

[162] J. T. Samosky, D. Burstein, W. Eric Grimson, R. Howe, S. Martin, and M. L. Gray, "Spatially-localized correlation of dGEMRIC-measured GAG distribution and mechanical stiffness in the human tibial plateau.," *Journal of orthopaedic research : official publication of the Orthopaedic Research Society* **23,** 93–101 (2005).

[163] W. Ling, R. R. Regatte, G. Navon, and A. Jerschow, "Assessment of glycosaminoglycan concentration in vivo by chemical exchange-dependent saturation transfer ( gagCEST )," (2008).

[164] I. Krusche-Mandl, B. Schmitt, L. Zak, S. Apprich, S. Aldrian, V. Juras, K. M. Friedrich, S. Marlovits, M. Weber, and S. Trattnig, "Long-term results 8 years after autologous osteochondral transplantation: 7 T gagCEST and sodium magnetic resonance imaging with morphological and clinical correlation.," *Osteoarthritis and cartilage / OARS, Osteoarthritis Research Society* **20,** 357–63 (2012).

[165] A. Singh, M. Haris, K. Cai, V. B. Kassey, F. Kogan, D. Reddy, H. Hariharan, and R. Reddy, "Chemical exchange saturation transfer magnetic resonance imaging of human knee cartilage at 3 T and 7 T.," *Magnetic resonance in medicine* **68,** 588–94 (2012).

[166] S. Mangia, T. Liimatainen, M. Garwood, and S. Michaeli, "Rotating frame relaxation during adiabatic pulses vs. conventional spin lock: simulations and experimental results at 4 T.," *Magnetic resonance imaging* **27,** 1074–87 (2009).

[167] R. R. Regatte, S. V. S. Akella, J. H. Lonner, J. B. Kneeland, and R. Reddy, "T1rho relaxation mapping in human osteoarthritis (OA) cartilage: comparison of T1rho with T2.," *Journal of magnetic resonance imaging : JMRI* **23,** 547–53 (2006).

[168] R. B. Souza, D. Kumar, N. Calixto, J. Singh, J. Schooler, K. Subburaj, X. Li, T. M. Link, and S. Majumdar, "Response of knee cartilage T1rho and T2 relaxation times to in vivo mechanical loading in individuals with and without knee osteoarthritis.," *Osteoarthritis and cartilage / OARS, Osteoarthritis Research Society* **22,** 1367–76 (2014).

[169] U. Duvvuri, S. Kudchodkar, R. Reddy, and J. Leigh, "T1$\rho$ relaxation can assess longitudinal proteoglycan loss from articular cartilage in vitro," *Osteoarthritis and Cartilage* **10,** 838–844 (2002).

[170] A. J. Wheaton, G. R. Dodge, D. M. Elliott, S. B. Nicoll, and R. Reddy, "Quantification of cartilage biomechanical and biochemical properties via T1rho magnetic resonance imaging.," *Magnetic resonance in medicine* **54,** 1087–93 (2005).

[171] A. J. Wheaton, G. R. Dodge, A. Borthakur, J. B. Kneeland, H. R. Schumacher, and R. Reddy, "Detection of changes in articular cartilage proteoglycan by T(1rho) magnetic resonance imaging.," *Journal of orthopaedic research : official publication of the Orthopaedic Research Society* **23,** 102–8 (2005).

[172] A. J. Wheaton, F. L. Casey, A. J. Gougoutas, G. R. Dodge, A. Borthakur, J. H. Lonner, H. R. Schumacher, and R. Reddy, "Correlation of T1rho with fixed charge density in cartilage.," *Journal of magnetic resonance imaging : JMRI* **20,** 519–25 (2004).

[173] L. M. Jazrawi, M. J. Alaia, G. Chang, E. F. Fitzgerald, and M. P. Recht, "Advances in magnetic resonance imaging of articular cartilage.," *The Journal of the American Academy of Orthopaedic Surgeons* **19,** 420–9 (2011).

[174] N. Wang and Y. Xia, "Depth and orientational dependencies of MRI T(2) and T(1$\rho$) sensitivities towards trypsin degradation and Gd-DTPA(2-) presence in articular cartilage at microscopic resolution.," *Magnetic resonance imaging* **30,** 361–70 (2012).

[175] J. Ellermann, W. Ling, M. J. Nissi, E. Arendt, C. S. Carlson, M. Garwood, S. Michaeli, and S. Mangia, "MRI rotating frame relaxation measurements for articular cartilage assessment.," *Magnetic Resonance Imaging* **31,** 1537–1543 (2013).

[176] J. Rautiainen, M. J. Nissi, T. Liimatainen, W. Herzog, R. K. Korhonen, and M. T. Nieminen, "Adiabatic rotating frame relaxation of MRI reveals early cartilage degeneration in a rabbit model of anterior cruciate ligament transection.," *Osteoarthritis and cartilage / OARS, Osteoarthritis Research Society* **22,** 1444–52 (2014).

[177] R. Stahl, A. Luke, X. Li, J. Carballido-Gamio, C. B. Ma, S. Majumdar, T. M. Link, B. C. Ma, S. Majumdar, and T. M. Link, "T1rho, T2 and focal knee cartilage abnormalities in physically active and sedentary healthy subjects versus early OA patients - A 3.0-Tesla MRI study," *European Radiology* **19,** 132–143 (2009).

[178] Y. Takayama, M. Hatakenaka, H. Tsushima, K. Okazaki, T. Yoshiura, M. Yonezawa, K. Nishikawa, Y. Iwamoto, and H. Honda, "T1$\rho$ is superior to T2 mapping for the evaluation of articular cartilage denaturalization with osteoarthritis: radiological-pathological correlation after total knee arthroplasty.," *European journal of radiology* **82,** e192–8 (2013).

[179] N. M. Menezes, M. L. Gray, J. R. Hartke, and D. Burstein, "T2 and T1rho MRI in articular cartilage systems.," *Magnetic resonance in medicine* **51,** 503–9 (2004).

[180] J. Y. Bae, K. S. Park, J. K. Seon, D. S. Kwak, I. Jeon, and E. K. Song, "Biomechanical analysis of the effects of medial meniscectomy on degenerative osteoarthritis.," *Medical & biological engineering & computing* **50,** 53–60 (2012).

[181] T. L. Donahue, M. L. Hull, M. M. Rashid, and C. R. Jacobs, "A finite element model of the human knee joint for the study of tibio-femoral contact," *J Biomech Eng* **124,** 273–280 (2002).

[182] N. Chantarapanich, P. Nanakorn, B. Chernchujit, and K. Sitthiseripratip, "A finite element study of stress distributions in normal and osteoarthritic knee joints," *J Med Assoc Thai* **92 Supplem,** 97–103 (2009).

[183] D. D. D'Lima, P. C. Chen, and C. W. Colwell Jr., "Osteochondral Grafting: Effect of Graft Alignment, Material Properties, and Articular Geometry," *The Open Orthopaedics Journal,* **3,** 61–68 (2009).

[184] T. M. Guess, G. Thiagarajan, M. Kia, and M. Mishra, "A subject specific multibody model of the knee with menisci," *Medical Engineering & Physics* **32,** 505–515 (2010).

[185] N. A. Netravali, S. Koo, N. J. Giori, and T. P. Andriacchi, "The Effect of Kinematic and Kinetic Changes on Meniscal Strains During Gait," *Journal of Biomechanical Engineering* **133,** 11006 (2011).

[186] E. Peña, B. Calvo, M. A. Martínez, D. Palanca, and M. Doblaré, "Finite element analysis of the effect of meniscal tears and meniscectomies on human knee biomechanics," *Clinical Biomechanics* **20,** 498–507 (2005).

[187] E. Peña, B. Calvo, M. A. Martínez, and M. Doblaré, "A three-dimensional finite element analysis of the combined behavior of ligaments and menisci in the healthy human knee joint.," *Journal of biomechanics* **39,** 1686–701 (2006).

[188] E. Pena, B. Calvo, M. A. Martinez, and M. Doblare, "Effect of the size and location of osteochondral defects in degenerative arthritis. A finite element simulation," *Computers in Biology & Medicine* **37,** 376–387 (2007).

[189] W. Wilson, B. van Rietbergen, C. C. van Donkelaar, and R. Huiskes, "Pathways of load-induced cartilage damage causing cartilage degeneration in the knee after meniscectomy," *Journal of Biomechanics* **36,** 845–851 (2003).

[190] N. Yang, H. Nayeb-Hashemi, and P. K. Canavan, "The combined effect of frontal plane tibiofemoral knee angle and meniscectomy on the cartilage contact stresses and strains," *Ann Biomed Eng* **37,** 2360–2372 (2009).

[191] N. H. Yang, H. Nayeb-Hashemi, P. K. Canavan, and A. Vaziri, "Effect of frontal plane tibiofemoral angle on the stress and strain at the knee cartilage during the stance phase of gait," *Journal of Orthopaedic Research* **28,** 1539–1547 (2010).

[192] B. Zielinska and T. L. Donahue, "3D finite element model of meniscectomy: changes in joint contact behavior," *J Biomech Eng* **128,** 115–123 (2006).

[193] M. E. Mononen, P. Julkunen, J. Toyras, J. S. Jurvelin, I. Kiviranta, and R. K. Korhonen, "Alterations in structure and properties of collagen network of osteoarthritic and repaired cartilage modify knee joint stresses," *Biomech Model Mechanobiol* **DOI 10.100** (2011).

[194] K. S. Halonen, M. E. Mononen, J. S. Jurvelin, J. Töyräs, and R. K. Korhonen, "Importance of depth-wise distribution of collagen and proteoglycans in articular cartilage—A 3D finite element study of stresses and strains in human knee joint," *Journal of Biomechanics* **46,** 1184–1192 (2013).

[195] K. S. Halonen, M. E. Mononen, J. S. Jurvelin, J. Töyräs, J. Salo, R. K. Korhonen, and J. To, "Deformation of articular cartilage during static loading of a knee joint – Experimental and finite element analysis," *Journal of Biomechanics* **47,** 2467–74 (2014).

[196] P. Julkunen, R. K. Korhonen, M. J. Nissi, and J. S. Jurvelin, "Mechanical characterization of articular cartilage by combining magnetic resonance imaging and finite-element analysis: a potential functional imaging technique," *Physics in Medicine & Biology* **53,** 2425–2438 (2008).

[197] M. E. Mononen, M. T. Mikkola, P. Julkunen, R. Ojala, M. T. Nieminen, J. S. Jurvelin, and R. K. Korhonen, "Effect of superficial collagen patterns and fibrillation of femoral articular cartilage on knee joint mechanics—A 3D finite element analysis," *Journal of Biomechanics* **45,** 579–587 (2012).

[198] M. E. Mononen, J. S. Jurvelin, and R. K. Korhonen, "Implementation of a gait cycle loading into healthy and meniscectomised knee joint models with fibril-reinforced articular cartilage," *Computer Methods in Biomechanics and Biomedical Engineering* 1–12 (2013), doi:10.1080/10255842.2013.783575.

[199] R. Shirazi and A. Shirazi-Adl, "Computational biomechanics of articular cartilage of human knee joint: Effect of osteochondral defects.," *J Biomech* **42,** 2458–2465 (2009).

[200] R. Shirazi and A. Shirazi-Adl, "Deep vertical collagen fibrils play a significant role in mechanics of articular cartilage," *Journal of Orthopaedic Research* **26,** 608–615 (2008).

[201] M. S. Venäläinen, M. E. Mononen, J. S. Jurvelin, J. Töyräs, T. Virén, and R. K. Korhonen, "Importance of Material Properties and Porosity of Bone on Mechanical Response of Articular Cartilage in Human Knee Joint—A Two-Dimensional Finite Element Study," *Journal of Biomechanical Engineering* **136,** 121005 (2014).

[202] W. Wilson, C. van Donkelaar, B. van Rietbergen, K. Ito, and R. Huiskes, "Erratum to "Stresses in the local collagen network of articular cartilage: a poroviscoelastic fibril-reinforced finite element study" [Journal of Biomechanics 37 (2004) 357–366] and "A fibril-reinforced poroviscoelastic swelling model for articular cartil," *Journal of Biomechanics* **38,** 2138–2140 (2005).

[203] W. Wilson, C. C. van Donkelaar, B. van Rietbergen, K. Ito, and R. Huiskes, "Stresses in the local collagen network of articular cartilage: a poroviscoelastic fibril-reinforced finite element study.," *Journal of biomechanics* **37,** 357–366 (2004).

[204] W. Wilson, C. C. van Donkelaar, B. van Rietbergen, and R. Huiskes, "A fibril-reinforced poroviscoelastic swelling model for articular cartilage," *Journal of biomechanics* **38,** 1195–1204 (2005).

[205] R. Shirazi, A. Shirazi-Adl, M. Hurtig, A. Shiraziadl, and M. Hurtig, "Role of cartilage collagen fibrils networks in knee joint biomechanics under compression," *Journal of Biomechanics* **41,** 3340–3348 (2008).

[206] G. A. Ateshian, W. H. Warden, J. J. Kim, R. P. Grelsamer, and V. C. Mow, "Finite deformation biphasic material properties of bovine articular cartilage from confined compression experiments.," *Journal of biomechanics* **30,** 1157–64 (1997).

[207] M. Holmes and V. Mow, "The nonlinear characteristics of soft gels and hydrated connective tissues in ultrafiltration," *Journal of Biomechanics* **23,** 1145–1156 (1990).

[208] L. P. Li, J. Soulhat, M. D. Buschmann, and A. Shirazi-Adl, "Nonlinear analysis of cartilage in unconfined ramp compression using a fibril reinforced poroelastic model," *Clin Biomech* **14,** 673–682 (1999).

[209] J. M. Huyghe, G. B. Houben, M. R. Drost, and C. C. van Donkelaar, "An ionised/non-ionised dual porosity model of intervertebral disc tissue.," *Biomechanics and modeling in mechanobiology* **2,** 3–19 (2003).

[210] W. M. Lai, J. S. Hou, and V. C. Mow, "A triphasic theory for the swelling and deformation behaviors of articular cartilage.," *Journal of biomechanical engineering* **113,** 245–58 (1991).

[211] A. Hosseini, S. K. Van de Velde, M. Kozanek, T. J. Gill, A. J. Grodzinsky, H. E. Rubash, and G. Li, "In-vivo time-dependent articular cartilage contact behavior of the tibiofemoral joint.," *Osteoarthritis and cartilage / OARS, Osteoarthritis Research Society* **18,** 909–16 (2010).

[212] T. D. MacLeod, K. Subburaj, S. Wu, D. Kumar, C. Wyatt, R. B. Souza, and S. V. Sambasivarao, "Magnetic resonance analysis of loaded meniscus deformation: a novel technique comparing participants with and without radiographic knee osteoarthritis," *Skeletal radiology* **18,** 1199–1216 (2013).

[213] K. D. Butz, D. D. Chan, E. A. Nauman, and C. P. Neu, "Stress distributions and material properties determined in articular cartilage from MRI-based finite strains.," *Journal of biomechanics* **44,** 2667–72 (2011).

[214] A. Kłodowski, M. E. Mononen, J. P. Kulmala, A. Valkeapää, R. K. Korhonen, J. Avela, I. Kiviranta, J. S. Jurvelin, and A. Mikkola, "Merge of motion analysis, multibody dynamics and finite element method for the subject-specific analysis of cartilage loading patterns during gait: differences between rotation and moment-driven models of human knee joint," *Multibody System Dynamics* (2015), doi:10.1007/s11044-015-9470-y.

[215] W. Mesfar and A. Shirazi-Adl, "Biomechanics of the knee joint in flexion under various quadriceps forces.," *The Knee* **12,** 424–34 (2005).

[216] W. Mesfar and A. Shirazi-Adl, "Knee joint mechanics under quadriceps–hamstrings muscle forces are influenced by tibial restraint.," *Clinical biomechanics (Bristol, Avon)* **21,** 841–8 (2006).

[217] W. Mesfar and A. Shirazi-Adl, "Knee joint biomechanics in open-kinetic-chain flexion exercises.," *Clinical biomechanics (Bristol, Avon)* **23,** 477–82 (2008).

[218] A. Shirazi-Adl and W. Mesfar, "Effect of tibial tubercle elevation on biomechanics of the entire knee joint under muscle loads.," *Clinical biomechanics (Bristol, Avon)* **22,** 344–51 (2007).

[219] K. B. Gu and L. P. Li, "A human knee joint model considering fluid pressure and fiber orientation in cartilages and menisci," *Medical Engineering & Physics* **33,** 497–503 (2011).

[220] P. Julkunen, P. Kiviranta, W. Wilson, J. S. Jurvelin, and R. K. Korhonen, "Characterization of articular cartilage by combining microscopic analysis with a fibril-reinforced finite-element model," *Journal of Biomechanics* **40,** 1862–1870 (2007).

[221] P. Tanska, M. E. Mononen, and R. K. Korhonen, "Supplementary material for : A Multi-scale Finite Element Model for Investigation of Chondrocyte Mechanics in Normal and Medial Meniscectomy Human Knee Joint During Walking," **3,** 1–5 (2014).

[222] M. E. Mononen, P. Tanska, H. Isaksson, and R. K. Korhonen, "Prediction of Collagen Degeneration and Osteoarthritis in Knee Joints from Normal and Overweight Subjects – Adaptive Computational 3D Analysis," in *XXV Congress of the International Society of Biomechanics* (2015), pp. AS–0503.

[223] M. Kazemi, L. P. Li, P. Savard, and M. D. Buschmann, "Creep behavior of the intact and meniscectomy knee joints," *Journal of the Mechanical Behavior of Biomedical Materials* **4,** 1351–1358 (2011).

[224] Q. Rong, J. Bai, Y. Huang, and J. Lin, "Biomechanical assessment of a patient-specific knee implant design using finite element method.," *BioMed research international* **2014,** 353690 (2014).

[225] M. Woiczinski, A. Steinbrück, P. Weber, P. E. Müller, V. Jansson, and C. Schröder, "Development and validation of a weight-bearing finite element model for total knee replacement.," *Computer methods in biomechanics and biomedical engineering* 1–13 (2015), doi:10.1080/10255842.2015.1089534.

[226] E. Peña, M. A. Martínez, B. Calvo, D. Palanca, and M. Doblaré, "A finite element simulation of the effect of graft stiffness and graft tensioning in ACL reconstruction.," *Clinical biomechanics (Bristol, Avon)* **20,** 636–44 (2005).

[227] J. Yao, J. Snibbe, M. Maloney, and A. L. Lerner, "Stresses and Strains in the Medial Meniscus of an ACL Deficient Knee under Anterior Loading: A Finite Element Analysis with Image-Based Experimental Validation," *Journal of Biomechanical Engineering* **128,** 135 (2006).

[228] S. Saarakkala, P. Julkunen, P. Kiviranta, J. Mäkitalo, J. S. Jurvelin, and R. K. Korhonen, "Depth-wise progression of osteoarthritis in human articular cartilage: investigation of composition, structure and biomechanics," *Osteoarthritis and cartilage / OARS, Osteoarthritis Research Society* **18,** 73–81 (2010).

[229] E. Schoenbauer, P. Szomolanyi, T. Shiomi, V. Juras, Š. Zbýň, L. Zak, M. Weber, and S. Trattnig, "Cartilage evaluation with biochemical MR imaging using in vivo Knee compression at 3T-comparison of patients after cartilage repair with healthy volunteers.," *Journal of biomechanics* (2015), doi:10.1016/j.jbiomech.2015.06.016.

[230] A. Maroudas, "Physicochemical properties of articular cartilage," in *Adult Articular Cartilage*, Freeman MAR, ed. 1979).

[231] S. Below, S. P. Arnoczky, J. Dodds, C. Kooima, and N. Walter, "The split-line pattern of the distal femur: A consideration in the orientation of autologous cartilage grafts," *Arthroscopy* **18,** 613–617 (2002).

[232] D. F. Villegas, J. A. Maes, S. D. Magee, and T. L. Haut Donahue, "Failure properties and strain distribution analysis of meniscal attachments," *Journal of Biomechanics* **40,** 2655–2662 (2007).

[233] R. D. Komistek, J. B. Stiehl, D. A. Dennis, R. D. Paxson, and R. W. Soutas-Little, "Mathematical model of the lower extremity joint reaction forces using Kane's method of dynamics.," *Journal of biomechanics* **31,** 185–9 (1998).

[234] M. Kozanek, A. Hosseini, F. Liu, S. K. Van de Velde, T. J. Gill, H. E. Rubash, and G. Li, "Tibiofemoral kinematics and condylar motion during the stance phase of gait," *Journal of Biomechanics* **42,** 1877–1884 (2009).

[235] P. Tanska, M. E. Mononen, and R. K. Korhonen, "A multi-scale finite element model for investigation of chondrocyte mechanics in normal and medial meniscectomy Human knee joint during walking," *Journal of Biomechanics* **48,** 1397–1406 (2015).

[236] T. Momersteeg, L. Blankevoort, R. Huiskes, J. Kooloos, J. Kauer, and J. Hendriks, "The effect of variable relative insertion orientation of human knee bone-ligament-bone complexes on the tensile stiffness," *Journal of Biomechanics* **28,** 745–752 (1995).

[237] I. Kutzner, B. Heinlein, F. Graichen, A. Bender, A. Rohlmann, A. Halder, A. Beier, and G. Bergmann, "Loading of the knee joint during activities of daily living measured in vivo in five subjects.," *Journal of biomechanics* **43,** 2164–73 (2010).

[238] Y. Dabiri and L. P. Li, "Altered knee joint mechanics in simple compression associated with early cartilage degeneration.," *Computational and mathematical methods in medicine* **2013,** 862903 (2013).

[239] E. K. Danso, J. T. J. Honkanen, S. Saarakkala, and R. K. Korhonen, "Comparison of nonlinear mechanical properties of bovine articular cartilage and meniscus.," *Journal of biomechanics* **47,** 200–6 (2014).

[240] E. K. Danso, J. T. A. Mäkelä, P. Tanska, M. E. Mononen, J. T. J. Honkanen, J. S. Jurvelin, J. Töyräs, P. Julkunen, and R. K. Korhonen, "Characterization of site-specific biomechanical properties of human meniscus—Importance of collagen and fluid on mechanical nonlinearities," *Journal of Biomechanics* 1–9 (2015), doi:10.1016/j.jbiomech.2015.01.048.

[241] X. Bi, X. Yang, M. P. G. Bostrom, and N. P. Camacho, "Fourier transform infrared imaging spectroscopy investigations in the pathogenesis and repair of cartilage," *Biochimica et Biophysica Acta - Biomembranes* **1758,** 934–941 (2006).

[242] R. K. Korhonen, P. Tanska, S. M. Kaartinen, J. M. Fick, and M. E. Mononen, "New Concept to Restore Normal Cell Responses in Osteoarthritic Knee Joint Cartilage.," *Exercise and sport sciences reviews* **43,** 143–52 (2015).

[243] G. A. Ateshian, "The role of interstitial fluid pressurization in articular cartilage lubrication.," *Journal of Biomechanics* **42,** 1163–1176 (2009).

[244] S. Park, R. Krishnan, S. B. Nicoll, and G. A. Ateshian, "Cartilage interstitial fluid load support in unconfined compression," *Journal of Biomechanics* **36,** 1785–1796 (2003).

[245] H.-S. Gan, T.-S. Tan, L.-X. Wong, W.-K. Tham, K. A. Sayuti, A. H. Abdul Karim, and M. R. bin Abdul Kadir, "Interactive knee cartilage extraction using efficient segmentation software: data from the osteoarthritis initiative.," *Bio-medical materials and engineering* **24,** 3145–57 (2014).

[246] A. Thambyah, J. C. H. Goh, and S. D. De, "Contact stresses in the knee joint in deep flexion.," *Medical engineering & physics* **27,** 329–35 (2005).

[247] A. Bedi, N. H. Kelly, M. Baad, A. J. S. Fox, R. H. Brophy, R. F. Warren, and S. A. Maher, "Dynamic contact mechanics of the medial meniscus as a function of radial tear, repair, and partial meniscectomy.," *The Journal of bone and joint surgery. American volume* **92,** 1398–408 (2010).

[248] J. M. Marzo and J. Gurske-DePerio, "Effects of medial meniscus posterior horn avulsion and repair on tibiofemoral contact area and peak contact pressure with clinical implications.," *The American journal of sports medicine* **37,** 124–9 (2009).

[249] A. Changoor, M. Nelea, S. Méthot, N. Tran-Khanh, A. Chevrier, A. Restrepo, M. S. Shive, C. D. Hoemann, and M. D. Buschmann, "Structural characteristics of the collagen network in human normal, degraded and repair articular cartilages observed in polarized light and scanning electron microscopies," *Osteoarthritis and Cartilage* **19,** 1458–1468 (2011).

[250] Š. Zbýň, V. Mlynárik, V. Juras, P. Szomolanyi, and S. Trattnig, "Evaluation of cartilage repair and osteoarthritis with sodium MRI.," *NMR in biomedicine* (2015), doi:10.1002/nbm.3280.

[251] R. Kijowski, D. G. Blankenbaker, K. W. Davis, K. Shinki, L. D. Kaplan, and A. A. De Smet, "Comparison of 1.5- and 3.0-T MR imaging for evaluating the articular cartilage of the knee joint," *Radiology* **250,** 839–848 (2009).

[252] Y. Xia, J. B. Moody, and H. Alhadlaq, "Orientational dependence of T2 relaxation in articular cartilage: A microscopic MRI ($\mu$MRI) study," *Magnetic Resonance in Medicine* **48,** 460–469 (2002).

[253] M. F. Koff, S. Parratte, K. K. Amrami, and K. R. Kaufman, "Examiner repeatability of patellar cartilage T2 values," *Magn Reson Imaging* **27,** 131–136 (2009).

[254] J. Zuo, R. Bolbos, K. Hammond, X. Li, and S. Majumdar, "Reproducibility of the quantitative assessment of cartilage morphology and trabecular bone structure with magnetic resonance imaging at 7 T," *Magnetic Resonance Imaging* **26,** 560–566 (2008).

**LASSE RÄSÄNEN**

*Current clinical methods cannot evaluate the influence of cartilage structure on knee joint function. Here, spatial variations in collagen fibril orientations and proteoglycans of articular cartilage were shown to modulate joint function in a spatial and time-dependent manner during standing and walking. These methods, i.e. the use of MRI and computational modeling, could be applied as a clinical tool to investigate more realistically failure points in joints leading potentially to osteoarthritis.*

UNIVERSITY OF
EASTERN FINLAND

*uef.fi*

**PUBLICATIONS OF**
**THE UNIVERSITY OF EASTERN FINLAND**
*Dissertations in Forestry and Natural Sciences*

ISBN 978-952-61-2146-8
ISSN 1798-5668